Spring 2012

Densification and thermal properties of zirconium diboride based ceramics

Matthew Joseph Thompson

Department: Materials Science and Engineering

Recommended Citation

Thompson, Matthew Joseph, "Densification and thermal properties of zirconium diboride based ceramics" (2012). *Doctoral Dissertations*. 2150.
https://scholarsmine.mst.edu/doctoral_dissertations/2150

DENSIFICATION AND THERMAL PROPERTIES OF ZIRCONIUM DIBORIDE BASED CERAMICS

By

MATTHEW J THOMPSON

A DISSERTATION

Presented to the Faculty of the Graduate School of the

MISSOURI UNIVERSITY OF SCIENCE AND TECHNOLOGY

In Partial Fulfillment of the Requirements for the Degree

DOCTOR OF PHILOSOPHY

in

MATERIALS SCIENCE AND ENGINEERING

2012

Approved
William G. Fahrenholtz, Advisor
Greg Hilmas, Co-Advisor
F. Scott Miller
Jeffrey D. Smith
Jay Switzer

PUBLICATION DISSERTATION OPTION

This dissertation has been prepared in the style such that the individual sections may be submitted for publication in the *Journal of the American Ceramic Society*. The pages 56 through 89 entitled "Effect of Starting Particle Size and Oxygen Content on Densification of ZrB_2" was published in the *Journal of the American Ceramic Society* in volume 94, issue 2 in 2011. The pages 90 through 128 entitled "Elevated Temperature Thermal Properties of ZrB_2 with Carbon Additions" was accepted for publication in the *Journal of the American Ceramic Society* in November 2011. The pages 129 through 162 entitled "Heating Rate Effects on the Thermal and Mechanical Properties of ZrB_2" have been submitted to the *Journal of the American Ceramic Society*. The pages 163 through 191 entitled "Thermal Properties of ZrB_2-TiB_2 Solid Solutions" and pages 201 through 214 entitled "Elevated Temperature Thermal Properties of ZrB_2-B_4C Ceramics" will be submitted to the *Journal of the American Ceramic Society* following revisions based on the suggestions of the dissertation committee.

ABSTRACT

The research presented in this dissertation focuses on the processing and thermomechanical properties of ZrB_2 based ceramics. The overall goal was to improve the understanding of thermal and mechanical properties based on processing conditions and additives to ZrB_2. To achieve this, the relationships between the thermal and mechanical properties were analyzed for ZrB_2 ceramics that were densified by different methods, varying amounts of carbon, B_4C, or TiB_2 additions.

Four main areas were investigated in this dissertation. The first showed that decreased processing times, regardless of densification method, improved mechanical strength to >500 MPa. This study also revealed that lower oxygen impurity contents led to less grain coarsening. The second study showed that higher heating rates narrowed the grain size distribution, which resulted in strengths above 600 MPa. However, the decreased processing times led to retention of ZrO_2, which decreased the thermal conductivity. The third study revealed that carbon additions interacted with ZrO_2 and WC impurities introduced during powder processing to form (Zr,W)C, which led to higher thermal conductivity than ZrB_2 with no carbon added. The last area examined the effect of solid solution additions on the electron and phonon contributions to thermal conductivity. The formation of solid solutions decreased thermal conductivity to <60 W/m•K compared to 93 W/m•K for nominally pure ZrB_2 at 25°C.

Taken as a whole, this research adds insight into the fundamental aspects of microstructure and composition that control the thermal and mechanical properties of ZrB_2. These changes impact thermal and mechanical properties, which control the performance of ZrB_2 based ceramics.

ACKNOWLEDGEMENTS

My sincerest gratitude goes to my advisor Dr. William Fahrenholtz for all his assistance and guidance through my time in graduate school. He has taught me a great deal about being direct and staying on point through my research. He has encouraged me to travel multiple times to both research experiences at WPAFB and several conferences a year, providing me with many contacts throughout the ceramic community. I would also like to thank Dr. Greg Hilmas, my co-advisor, who offered valuable insight into processing and thermal properties that constantly improved my understanding.

I would also like to thank the rest of my committee: Drs. Jeff Smith, Scott Miller, and Jay Switzer. They provided insight in several areas that constantly improved my knowledge and understanding about materials processing and characterization.

I should also acknowledge the Air Force Office of Scientific Research through contract numbers FA9550-06-1-0125 and FA9550-09-1-0168 under program managers Dr. Joan Fuller and Dr. Ali Sayir. Dr. Michael Cinibulk and Dr. Carmen Carney were also pertinent to access and use of SPS for two of the papers presented here.

I also need to thank all of my friends and colleagues in 307 for their help and support. There are many people to who have helped me and the list is too exhaustive to show here.

My family deserves many thanks as well including my mom, dad, Nicki, and Rachel for their love, guidance, and upbringing that got me to where I am today.

Finally, I thank my fiancé for her love and support over the extended long distance. She gave me hope and helped me through those long and frustrating hours.

TABLE OF CONTENTS

Page

SECTION

PAPER

SECTION

LIST OF FIGURES

PAPER 1

PAPER 2

PAPER 3

PAPER 4

LIST OF TABLES

SECTION

1. INTRODUCTION

Zirconium diboride (ZrB_2) is an ultra high temperature ceramic (UHTC) that has strong covalent bonding, which gives it a melting temperature above 3000°C (3250°C for ZrB_2), high hardness (23 GPa), and high elastic modulus (>500 GPa experimentally, 546 GPa by calculation).[1,2] The bonding also has metallic character, which results in high thermal (60 W/m•K or higher) and electrical (10^7 S/m) conductivities.[1-4] With this unusual combination of properties, ZrB_2 shows promise for diverse applications such as cutting tools, molten metal crucibles, and thermal protection systems for hypersonic aerospace vehicles.[5]

Additives have been shown to improve densification, thermomechanical properties, and oxidation behavior.[1,5] Some additives have been used to remove oxides or prevent further oxidation, while others have been added to improve mechanical properties. The focus of the present research has been to provide insight on how processing conditions and additives affect the thermal properties of ZrB_2. Thermal properties have not been systematically evaluated for different processing techniques or as a function of additive contents. This information is important to the UHTC community because researchers commonly compare mechanical properties and oxidation behavior of materials prepared using different processing conditions without considering their impact on thermal properties. The research conducted in the present study examined the effect of processing parameters on controlling the size and distribution of grains, phases, and grain boundaries, which, in turn, can be used to manipulate thermal conductivity. If thermal conductivity can be increased, then thermal protection systems for hypersonic vehicles would be more efficient at transporting heat, which could, in turn, increase thermal shock resistance and allow for faster vehicle speeds to be achieved.

In hypersonic thermal protection systems, ZrB_2 has been proposed for use as sharp leading and trailing edges. Sharp edge designs have the potential to improve vehicle maneuverability, but temperatures at sharp leading edges increase as leading edge radius decreases and have been predicted to be between 2000K and 2500K depending on the radius and trajectory.[6] Increasing the thermal conductivity of the ceramic leading edge would improve the conduction of heat away from the hot surfaces (Figure 1.1) to cooler areas where it could be dissipated by radiation, where $\dot{q}_i$ is heat flow due to i.

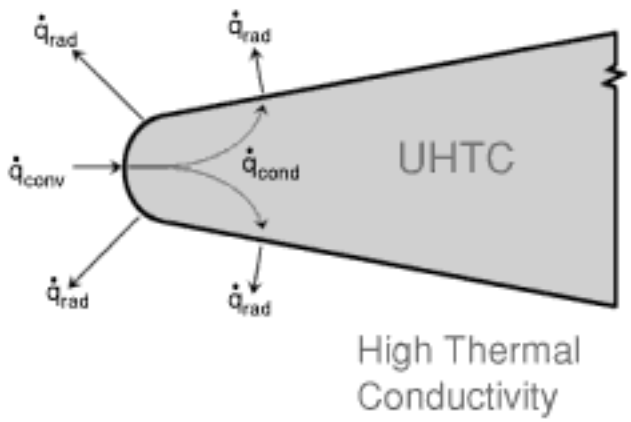

$$\dot{q}_{conv} = \dot{q}_{rad} + \dot{q}_{cond}$$

Figure 1.1: Notional diagram of a leading edge showing a balance for the generation and dissipation of heat.[7]

An increase in thermal conductivity could also enable ZrB_2 to be used in other high heat load and thermal cycling applications like propulsion systems or high temperature electrodes. Conversely, a decrease in thermal conductivity could make ZrB_2 more attractive as high temperature heat shields or thermal insulation. The understanding of how processing conditions and additives affect thermal properties may enable the use of ZrB_2 in aerospace applications that require thermally insulating materials able to operate at very high temperatures to reduce heat transfer to unwanted areas.

The purpose of this research has been to systematically study how densification methods, impurity contents, and additives affect the thermal and mechanical properties of ZrB_2 based ceramics. The main advances described in the dissertation are related to the effects of impurities and additives that are introduced intentionally or unintentionally during processing including WC, TiB_2, oxides, etc., on the thermal conductivity of ZrB_2. In addition, the effects of densification method (sintering, hot pressing, or spark plasma sintering) on the microstructure, mechanical, and thermal properties were also studied. For each of these areas, few fundamental studies have investigated the effects of these processing parameters on the thermal properties of ZrB_2-based ceramics. This research answered a number of technical questions including:

1. How does the densification method affect the microstructure and mechanical properties of ZrB_2 with varying oxygen contents?
2. Does the heating rate used during hot pressing or spark plasma sintering impact the mechanical and/or thermal properties of ZrB_2?
3. How do carbon additions affect the thermal conductivity of ZrB_2 ceramics?

4. Does the formation of solid solutions alter the electron and phonon contributions to thermal conductivity of ZrB_2 ceramics?

This research examined fundamental microstructure-property relationships to determine if the properties of ZrB_2-based ceramics could be improved, which could enable their use in thermal protection systems and other applications involving extreme thermal environments.

The research presented here has the potential to improve the knowledge base of the aerospace community that may utilize these materials for advanced hypersonic aerospace vehicles by examining microstructure-property relationships in materials densified by different methods or containing different additives. By understanding how additives and processing techniques affect thermal and mechanical properties, materials engineers may be able to design ZrB_2-based ceramics that are tailored to the needs of the aerospace community for applications such as thermal protection systems. Improved thermal protection systems could enable higher efficiency and increase the speed of future hypersonic vehicles.

References

1. W.G. Fahrenholtz, G.E. Hilmas, I.G. Talmy, and J.A. Zaykoski, "Refractory Diborides of Zirconium and Hafnium," *J. Am. Ceram. Soc.,* **90** [5] 1347-64 (2007).

2. X. Zhang, X. Luo, J. Han, J. Li, and W. Han, "Electronic structure, elasticity and hardness of diborides of zirconium and hafnium: First principles calculations," *Computational Materials Science,* **44** [2] 411-21 (2008).

3. R.A. Cutler, "Engineering Properties of Borides," pp. 787-803 in Vol. 4, *Ceramics and Glasses: Engineered Materials Handbook.* Edited by S. J. S. Jr. ASM International, Materials Park, OH, 1991.

4. L.S.S. R. Telle, and K. Takagi, "Boride-Based Hard Materials," pp. 802-945 in *Handbook of Ceramic Hard Materials.* Edited by R. Riedel. Wiley-VCH, Weinheim, Germany, 2000.

5. M.M. Opeka, I.G. Talmy, and J.A. Zaykoski, "Oxidation-based materials selection for 2000C + hypersonic aerosurfaces: Theoretical considerations and historical experience: Special Section: Ultra-High Temperature Ceramics (Guest Editors: Joan Fuller and Michael D. Sacks)," *Journal of Materials Science,* **39** 5887-904 (2004).

6. D.M. Van Wie, D.G. Drewry, D.E. King, and C.M. Hudson, "The hypersonic environment: Required operating conditions and design challenges," *Journal of Materials Science,* **39** [19] 5915-24 (2004).

7. N.P. Bansal, *Handbook of ceramic composites*. Kluwer Academic Publishers, 2005.

2. LITERATURE REVIEW

The purpose of this section is to introduce the published research that is related to the work presented in this dissertation. This section will first discuss the structure, bonding, and densfication of ZrB_2. Then, the later portion will discuss mechanical, thermal, and electrical properties of ZrB_2 ceramics.

2.1. PHASE EQUILIBRIA

Reactions between elemental mixtures of zirconium and boron have been studied by a number of researchers. A phase diagram of zirconium and boron is shown in Figure 2.1.[6] ZrB_2 is shown to have a limited solid solution range and a high melting temperature (3245°C) compared to the end members. While other compounds (ex. ZrB_{12}) also form in this system, the majority of research has been focused on the diboride.[7,8] Similarly, other metal diborides have a high melting temperature similar to ZrB_2. Specifically, TiB_2 and HfB_2 have melting temperatures of 3225°C and 3380°C, respectively.[6]

Additions of B_4C or carbon have been used to remove oxides and aid densification of ZrB_2.[9] However, as shown in Figure 2.2, these additions reduce the melting temperature of the composite due to eutectic formation, which is several hundred degrees below that of ZrB_2; 2220°C for ZrB_2-B_4C and 2390°C for ZrB_2-C.[6] In each case, a small amount (up to ~2 mol%) of B_4C or carbon goes into solid solution in ZrB_2 at the eutectic temperature. Larger amounts of additives are present as a second phase with no additional thermodynamically stable phases other than the end members. Adding B_4C as a second phase has been shown to increase hardness and flexure strengths, while carbon has been shown to decrease the flexure strength of ZrB_2.[10-12] However, the effects of these additions on the thermal, electrical, and oxidation behavior has not been fully investigated.

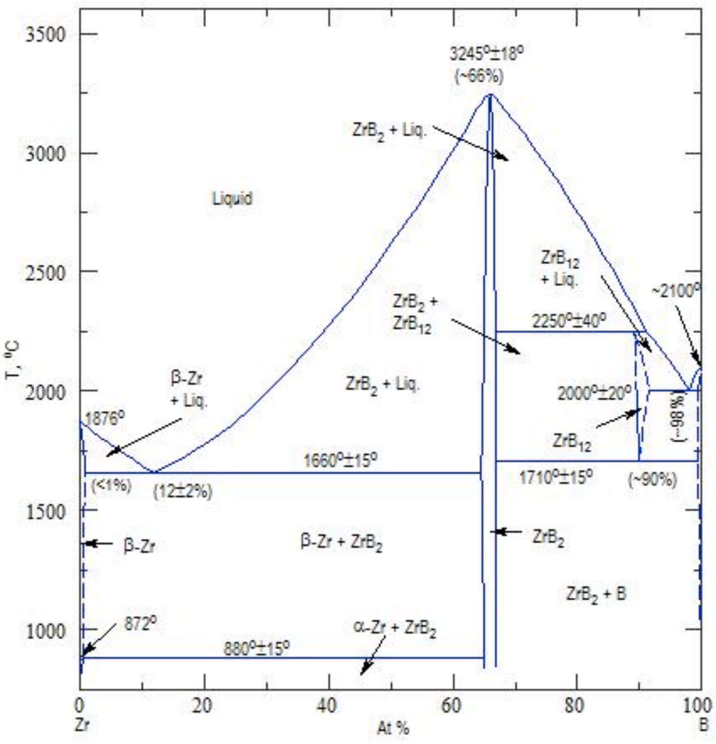

Figure 2.1: Zr and B phase diagram showing melting temperature at 3245°C.[6]

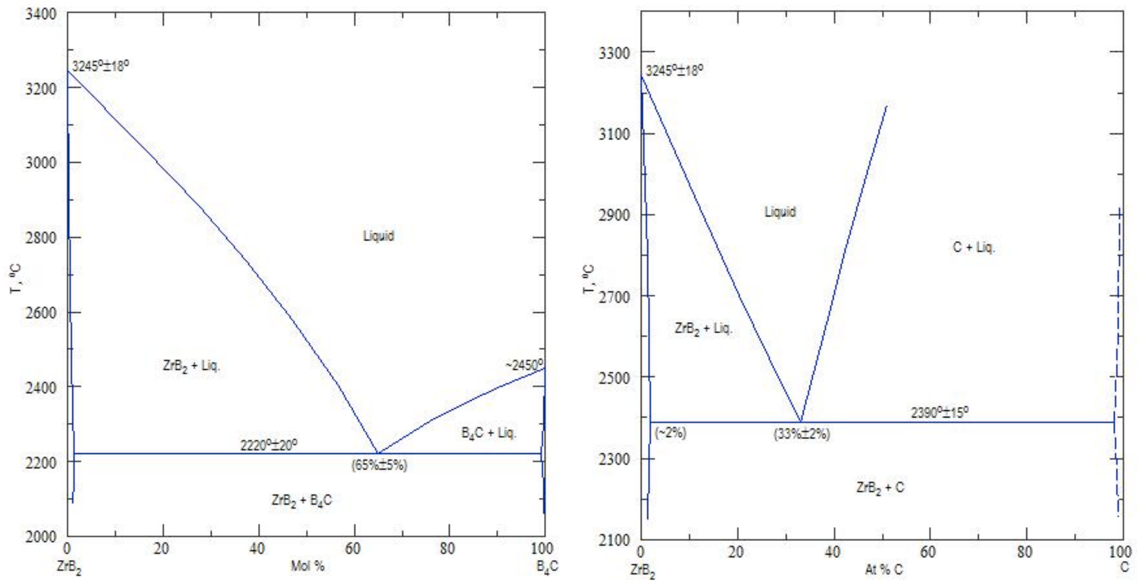

Figure 2.2: Phase diagrams of ZrB_2 with (a) B_4C and (b) carbon additions.[6]

2.2. CRYSTALLOGRAPHY AND BONDING

Metal diboride structures, MB_2, have a primitive hexagonal crystal structure, P6/mmm, shown in Figure 2.3.[7,13,14] The alternating layers of zirconium and boron atoms define the AlB_2 prototype. The base unit has a six member ring of boron atoms (sp^2 hybridized) and the zirconium atom plane has seven atoms in a hexagonal close packed structure. In total, the unit cell contains one formula unit. Each zirconium atom is surrounded by six other in plane zirconium atoms and has 12 nearest boron atom neighbors in adjacent planes. Each boron atom is surrounded by three boron atoms in plane and six zirconium nearest neighbors in adjacent planes.[15,16]

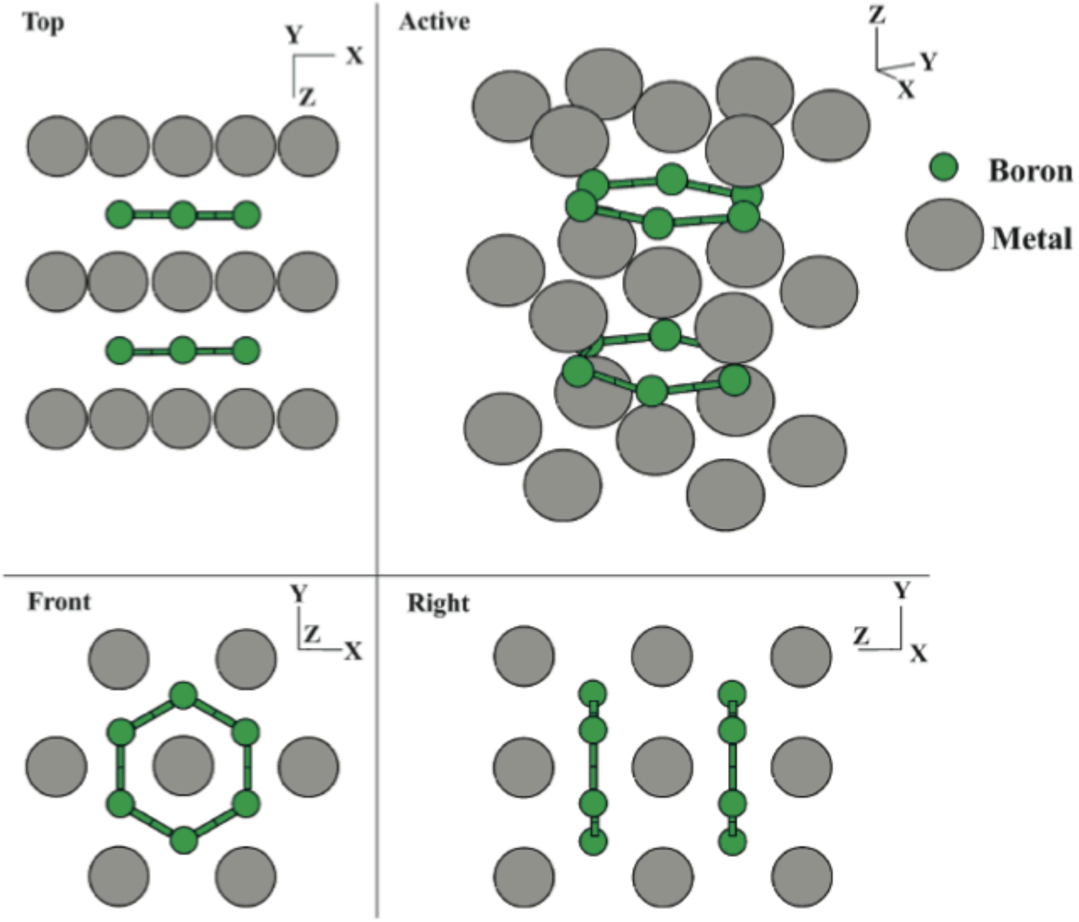

Figure 2.3: AlB_2 crystal structure that shows the symmetry of P6/mmm.[7]

The AlB_2 type crystal structure is unusual in that there are a number of different types of bonding environments within the crystal structure.[17] The first type of bonding occurs in the boron sub-lattice, which typically supports sp^2 bonding (graphite-like structure). This particular bond type has been shown to be covalent in nature.[16,17] The strength of the B-B bonds within the sub-lattice increases the stiffness of the overall structure, which gives rise to the high melting temperature, hardness, strength, and chemical stability of transition metal diborides.[7] The second type of bonding, M-B, is also covalent in nature with a limited amount (~8% for ZrB_2) of ionic character.[16,17] The characteristic properties of the MB_2 complex are controlled by the strength of the M-B bond. That is to say that the hybridization of the bond (typically spd hybridization) and the size of the metal atom controls the length of the a-axis and, therefore, can stretch B-B bonds.[7] The metal atom in MB_2 structures donates two electrons per metal atom to M-B bonding, and an additional partial electron to support the B-B sub-lattice.[16,18] The donation of a partial electron to the B-B sub-lattice changes going across a row of the periodic table (e.g., Zr, Nb, Mo…) because of the filling of bonding and anti-bonding states in the hybrid orbitals.[16] The final type of bond in the MB_2 structure is M-M bonding. Due to the formation of alternating sheets of Zr and B atoms in the crystal structure, each metal atom has six nearest metal atoms. This environment gives rise to metallic bonding, and contributes to the high electrical and thermal conductivities of the diborides.[15-17] The remaining electrons per metal atom (i.e. electrons not donated to M-B or B-B bonding) contribute to free electron movement between metal atoms. Figure 2.4 shows the density of states (DOS) curve, where the Fermi energy level is found in the conduction band.[16] Having the Fermi energy level in the conduction band indicates the presence of free electron motion and, therefore, high electrical conductivity.

The number of electrons per atom donated to M-M bonding can be found by measuring the work function of the material (ϕ)[19]. The work function is the amount of energy required to remove a valence electron from the surface of a material.[20] For electrical conductors this is equivalent to the Fermi-level, because it is also defined as the energy difference between the Fermi-level and the lowest level of the conduction band.[21] Equation 1 may then be used to calculate the number of conducting electrons per unit volume (Z), where E_F is the Fermi energy level, h is Planck's constant, and m is the mass of an electron. In the case of ZrB_2, the work function is 4.6 eV,[19] which means the number of electrons per unit volume is 4.47 x 10^{28} e/m^3.[20]

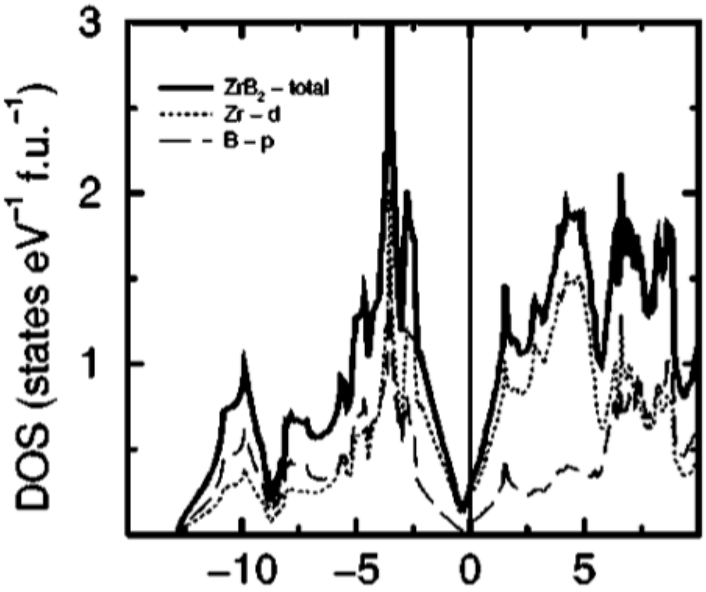

Figure 2.4: Density of states curve for ZrB_2, where electrons can be found in the conduction band.[16]

$$\phi = E_F = \frac{\hbar^2}{8m}\left[\frac{3Z}{\pi}\right]^{2/3} \tag{1}$$

By calculating the number of Zr atoms per unit volume based on crystallographic information (3.255 x 10^{28} Zr atoms/m^3), the number of electrons per Zr atom donated to M-M bonding is calculated to be 1.37. Based on the DOS curve and charge density distribution plots, two electrons are involved with M-B bonding.[16] This results in 0.63 electrons per Zr atom donated to supporting the boron sub-lattice. Vajeeston et al. and Zhang et al. have confirmed this result.[2,16]

2.3. DENSIFICATION

Densification of TiB_2, ZrB_2, and HfB_2 (generically designated as MeB_2) is affected by oxygen impurities that are present on the surfaces of the individual powder particles.[12,22-27] Oxidation of MeB_2 compounds under ambient conditions is nominally stoichiometric, resulting in the formation of equimolar amounts of MeO_2 and B_2O_3. At elevated temperatures, B_2O_3 evaporates, leaving a porous MeO_2 scale that does not act as a barrier to further oxidation.[28] Additives, such as B_4C, $MoSi_2$, and C, have been shown to react with oxygen impurities present on the surfaces of the starting powder particles at elevated temperatures.[29,30] Removing these impurities from the particle surfaces is beneficial to the densification process and leads to increased densification rates, decreased grain coarsening, and improved oxidation resistance.[27,31,32] Specifically, Zhu showed that carbon added to remove oxygen impurities decreased both the temperature and sintering hold time required to achieve near fully dense ZrB_2 by pressureless sintering by decreasing the effects of grain coarsening.[12] Three reactions can be used to describe possible processes that occur when carbon is added (Reactions 2-4). The reaction in equation 2 describes the carbothermal reduction of both oxidation products (ZrO_2 and B_2O_3 for ZrB_2). However, at elevated temperatures, B_2O_3 can evaporate by Reaction 3. When this happens, carbon can react directly with ZrO_2 to form ZrC by Reaction 4. For typical levels of oxygen impurities in starting ZrB_2 powders (i.e., 1 to 2 wt%), the relatively small amounts of ZrC (i.e., <1 wt%) likely to go into solid solution with the ZrB_2, based on the Zr-B-C phase diagram.[6]

$$ZrO_2 + B_2O_3 + 5C \rightarrow ZrB_2 + 5CO_{(g)} \qquad (2)$$

$$B_2O_3 \rightarrow B_2O_{3(g)} \quad (3)$$

$$ZrO_2 + 3C \rightarrow ZrC + 2CO_{(g)} \quad (4)$$

2.3.1. Additive Effects. Additives like carbon and B_4C have been shown to remove surface oxygen impurities present on the surface of the starting powders.[12,33] Removal of oxygen impurities improves densification and reduces effects of grain coarsening as discussed earlier.[22] A list of common additives and primary purpose of each additive is shown in Table 2.1. Other types of additives such as SiC and $MoSi_2$ improve oxidation resistance at elevated use temperatures of >1000°C.[26,29,34-36] These additives are used because when oxidized, a SiO_2 scale forms on the outside of ZrB_2 and impedes further oxidation.[37] One disadvantage to SiO_2 forming additives is that the use time decreases above 1650°C, at which point melting of SiO_2 occurs and even more so when above 2270°C where a eutectic forms between SiC and ZrB_2.[6,38] WC, TaB_2, or heavy metal additives aid in densification and decrease melting temperature, and also form solid solutions with ZrB_2, thus lowering use temperature.[39-41] These additives also improve oxidation resistance because they reduce oxygen diffusion while also reducing grain size and increasing strength.[37]

Table 2.1: Additive Effects on the Sintering and Oxidation Behavior of ZrB_2 with Associated References

Additive	**Purpose of Additive**	**References**
Carbon	Removes oxygen impurities	12,30,42,43
B_4C	Removes oxygen impurities and improves strength	30,33
WC	Removes oxygen impurities and is a sintering aid	44
SiC	Forms passive oxide layer and is a sintering aid	40,42,43,45-47
$MoSi_2$	Forms passive oxide layer and is a sintering aid	29,34,48-50
$TaSi_2$	Forms passive oxide layer and is a sintering aid	40,48
MeB_2	Forms solid solution, decreases oxygen diffusion rates	35,43
Refractory metals	Forms solid solution, decreases oxygen diffusion rates	40

2.3.2. Hot Pressing.

Due to strong covalent bonding present and low diffusion rates that inhibit the material transport required for densification, hot pressing has typically been used to densify ZrB_2.[4] In general, pressure applied during heating allows for faster densification and finer grain sizes.[51] Equation 5 shows the effect pressure has on the densification rate, where H is a numerical constant, D is the diffusion coefficient, ϕ is the stress intensity factor, G is the grain size, k is the Boltzmann constant, T is the absolute temperature, p is the externally applied stress, and m and n are constants dependent on the densification mechanism.[51] Specifically for MeB_2 ceramics, HfB_2 has been shown to reach full density at temperatures as low as 1800°C by hot pressing, which is a few hundred degrees lower than typically required for densification by pressureless sintering.[52]

$$\frac{1}{\rho}\frac{d\rho}{dt} = \frac{HD\phi^n}{G^m kT}p^n \tag{5}$$

Several researchers have explored a number of methods to decrease the hot pressing temperature.[53] The addition of $MoSi_2$ or $TaSi_2$ has been shown by Sciti et al. to reduce the hot pressing temperature to as low as 1750°C because of liquid phase formation.[54,55] Zhu et al. showed that carbon and B_4C remove oxygen impurities that are known to impede densification and coarsen grains.[9,12,22,23,42,44,56] The most common additive to ZrB_2 is SiC, which decreases the densification temperature and reduces grain growth while improving mechanical strength and fracture toughness.[26,57,58] In general, additives that have been used for pressureless sintering also work for hot pressing.[26,30,42]

2.3.3. Spark Plasma Sintering. Spark plasma sintering (also referred to as pulsed electric current sintering or field assisted sintering) provides rapid densification for different types of materials by combining heating, using a pulsed direct current (DC), with an applied uniaxial load.[26,56,59-64] A representation of the setup is shown in Figure 2.5.[61] The pulsed current leads to so-called Joule heating of the sample and die at rates as high as about 600°C/min. Unlike conventional processes in which specimens are heated from the outside, spark plasma sintering produces a unique temperature distribution whereby temperature decreases radially from the center of the sample to the outside.[56,65] Depending on the location of temperature measurement, through a hole in the top of the die or the outside of the graphite sleeve, the measured temperature can be up to 200°C to 300°C lower than the actual powder temperature. Several researchers have modeled this behavior.[59,61,62,65,66]

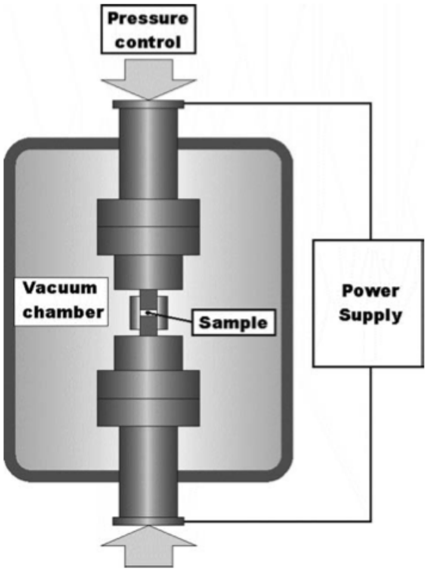

Figure 2.5: A schematic of the SPS setup as shown by Munir et al.[61]

In comparison to hot pressing, grain growth is typically lower during densification by spark plasma sintering due to increased heating rates and the application of the external force (similar to hot pressing), which leads to faster densification than sintering or hot pressing.[63] Using spark plasma sintering, ZrB_2-SiC has been shown to reach near full density as low as 1550°C with a resulting grain size of ~2 μm.[67-69] Likewise, pure ZrB_2 has been shown to achieve full density by spark plasma sintering at much lower temperatures than hot pressing, reaching full density at temperatures as low as 1800°C, compared to temperatures of 2000°C or above that are typical for hot pressing.[54,66,67,70,71] Other research in the densification and kinetics of sintering ZrB_2 with additives has been reported by a number of researchers. This work has been limited to densification behavior and basic property measurement.[54,60,66,67,70,72] To decrease the temperature of densification in ZrB_2 based ceramics, several researchers have added copper, iron, or other metals to improve the path of conduction, which also leads to liquid phase sintering.[39,66]

2.4. MECHANICAL PROPERTIES

The strength of ceramics can be measured in a variety of ways.[73] The most common for UHTCs is the 4-point bend method, which is described in ASTM standard C1161.[75] The testing geometry is shown in Figure 2.6.[74] The geometry is such that the inner span is half that of the outer span. Using this testing geometry, Equation 6 can be used to calculate the flexure strength of the specimen, where P is the load, L is the outer support span length, b is the specimen width, and d is the specimen thickness.[73]

$$\sigma = \frac{3PL}{4bd^2} \tag{6}$$

The flexure strength of ZrB_2 has been reported by a number of researchers to be as high as ~600 MPa.[43,55,75] Specifically, Chamberlain et al. showed that attrition milled (WC media) and HP ZrB_2 achieved strengths up to 584 MPa with an average grain size of 6 μm.[44] A previous summary of flexure strength data presented in Figure 2.7 showed a relationship with the inverse square root of grain size.[25,76-78] This agrees with the Griffith relationship for the strength of brittle materials in which all larger flaws have been eliminated, equation 7. In this relationship, σ is the flexure strength, K_{1C} is the fracture toughness (typically 3-4 MPa $m^{1/2}$, d is the grain size, and Y is a constant that depends on crack geometry (1.98 for a surface flaw typically used).[73,79]

$$\sigma = \frac{K_{1C}}{Y\sqrt{d}} \tag{7}$$

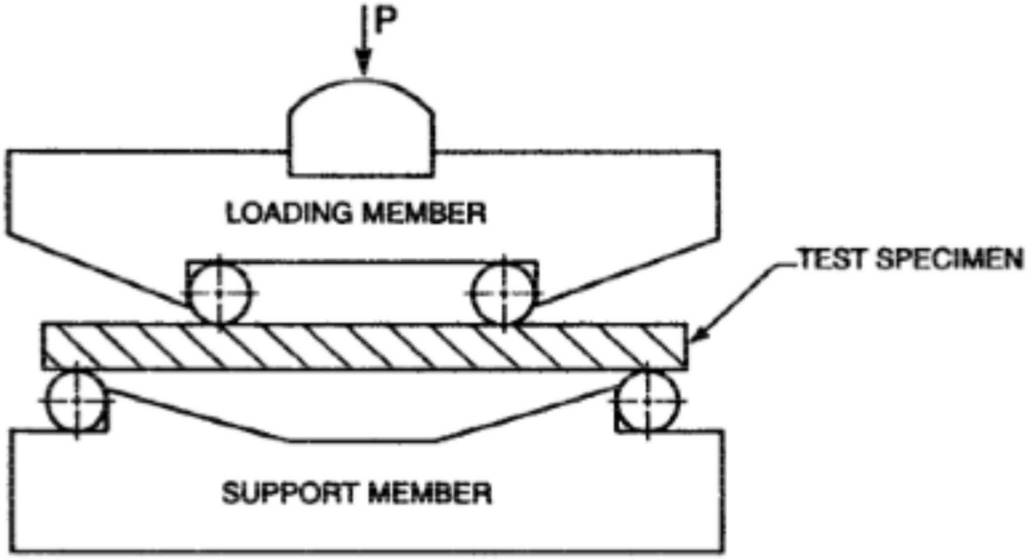

Figure 2.6: The 4-point testing geometry as defined and illustrated by ASTM C1161.[74]

Other densification techniques have produced high strength ZrB_2 as well. SPS was used to densify ZrB_2 at much higher heating rates, which required less time at the densification temperature, and resulted in ceramics with smaller grain sizes.[60,69,80-83] For ZrB_2 with a grain size of 3 μm, an average strength of 760 MPa was measured.[54,55] This is not to say that SPS inherently produces ceramics with superior properties, but rather that shorter processing times and lower densification temperatures can produce microstructures with finer grain sizes than are possible using other methods, which results in higher strengths. It has been confirmed by a number of researchers that the increased heating rates and pulsed direct current led to shorter densification times and decreased grain sizes, which increased the strength of diborides.[58,60,69,72,80,81,84]

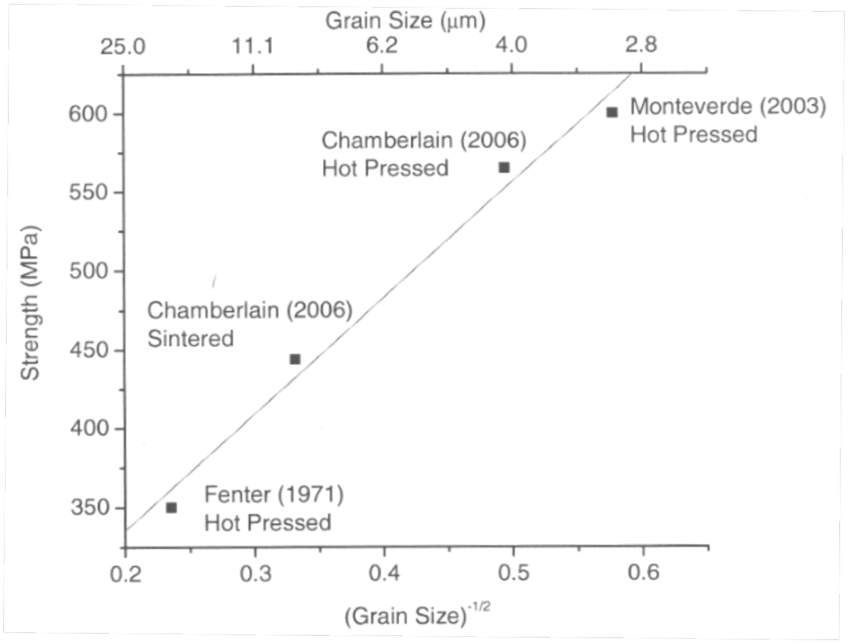

Figure 2.7: A collection of flexure strength versus (grain size)$^{-1/2}$ as summarized by Zimmermann.[78]

Sintering offers the benefit of near net-shape forming, but, to date, densification of diborides has only been accomplished with additives.[7,25] The strength of sintered ZrB_2 has been reported to be as high as 444 MPa by Chamberlain et al.[25] When 20 vol% $MoSi_2$ was added, Sciti et al. found that the flexure strength increased to 531 MPa.[54,85] This was primarily due to $MoSi_2$ pinning ZrB_2 grains, which resulted in a decrease in the average grain size to 2-3 μm compared to a grain size of 9.1 μm reported by Chamberlain for ZrB_2 with minimal additives.[25,54]

Additives such as $MoSi_2$, SiC, or B_4C have been shown to result in diboride particulate composites with increased strength.[10,86-89] The addition of SiC in particular increased the strength of ZrB_2 and HfB_2 to over 1 GPa.[7,44] As an additive, SiC has been reported to lead to increased the Vickers' hardness and improved the strength at room and elevated temperatures due to its ability to pin grain growth and reduce average grain size compared to ZrB_2 without SiC additions.[11,35,67,75,81,84,89] Similar effects have been reported with the addition of $MoSi_2$. The addition of $MoSi_2$ up to 20 vol% has been used in PS, HP, and SPS to improve room and elevated temperature strengths.[29,71,80] The flexure strengths were found to be >700 MPa for ZrB_2-$MoSi_2$.[54,80] Another additive, B_4C, has been a common additive to diborides to remove oxide impurities from particle surfaces and promote densification.[33] B_4C has been shown to increase the hardness and strength of diborides when smaller amounts (<20 vol%) are added.[10,90] Larger additions of B_4C (50 vol%), however, have been shown by Sigl and Kleebe to produce microcracking in TiB_2 because of the thermal expansion mismatch between the additive and the matrix.[91] As a result, the flexure strength and elastic modulus of TiB_2 with larger additions of B_4C decreased.

2.5. THERMAL PROPERTIES

Similar to mechanical properties, the thermal properties are critical to the application of UHTCs into hypersonic vehicles, high temperature electrodes, etc. In particular, the understanding of how heat flows through a material is important to optimize performance for any intended application. As a result of the combination of metallic and covalent bonding in diboride based ceramics, one can see that the electron and phonon transfer mechanisms affect the heat transfer of the ceramics in a different way than just covalent or ionic bonded ceramics. In this section, thermal conductivity, heat capacity, and thermal diffusivity of diboride based ceramics is discussed in detail.

2.5.1. Thermal Conductivity. The thermal conductivity of MB_2 ceramics has been reported by a number of researchers. In general, the thermal conductivities of pure MB_2 ceramics (TiB_2, ZrB_2, HfB_2, etc.) have similar values and behavior as a function of temperature. For example, the room temperature thermal conductivity of TiB_2 was reported to be 96 W/m•K compared to 95 W/m•K for ZrB_2 at room temperature.[92,93] However, the values reported have varied widely, from as low as about 40 W/m•K to above 120 W/m•K for HfB_2-20SiC ceramics (Figure 2.8).[40] The differences in thermal conductivity have been due to a variation in processing technique, impurities, additives, and grain sizes.[46,50] Specifically, the thermal conductivity of ZrB_2 has been reported as low as 38 W/m•K for attrition milled and then hot pressed ZrB_2 and as high as 95 W/m•K for ZrB_2 reacted from elemental forms and then hot pressed.[11,94]

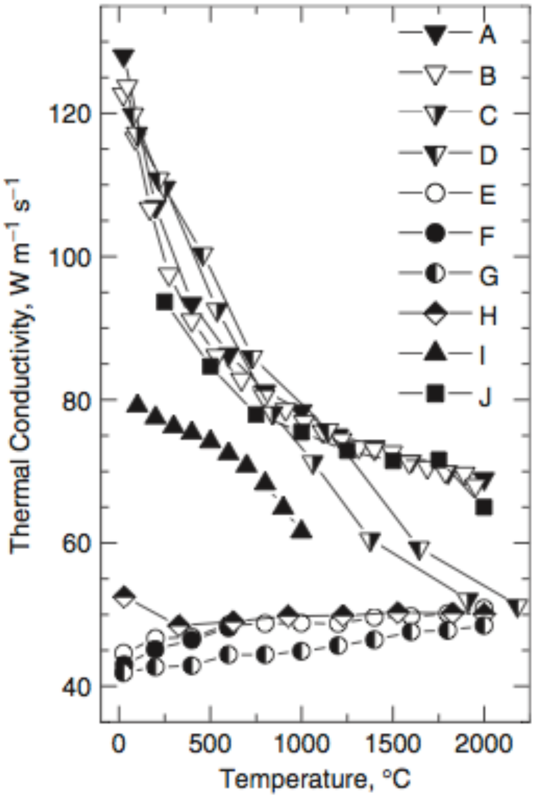

Figure 2.8: Thermal conductivity of HfB$_2$-20vol% SiC ceramics as a function of temperature.[40] The different designations refer to different processing steps and testing facilities.

A number of methods may be used to measure thermal conductivity such as the parallel plate method and the hot-wire method.[95,96] The basic idea for the measurement of thermal conductivity is to create a temperature gradient through the specimen and, assuming steady state heat flow, measure the slope of the temperature profile. Thermal conductivity as a function of temperature can be difficult to measure directly as a result of bulky test setups and steady state conditions. For fine-grained technical ceramics, the common method is to measure thermal diffusivity and heat capacity, which can then be used to calculate thermal conductivity using Equation 8,[97] where α is the thermal diffusivity, C_P is the heat capacity, and ρ is density.[98] More information about heat capacity, thermal diffusivity, and how each is measured can be found in Sections 2.5.2. and 2.5.3, respectively.

$$\lambda = \alpha C_P \rho \qquad (8)$$

The thermal conductivity of diboride-based ceramics is comprised of both electron and phonon contributions.[46] In fact, the electron and phonon contributions are additive.[99] For these ceramics, both modes of thermal transport are significant because of the presence of both metallic and ionic/covalent bond types in the AlB_2 crystal structure. In this case, metallic bonding in the close packed M layers allows for electron transport, while the M-B and B-B covalent bonds have a significant influence on the phonon transport.

2.5.1.1. Phonons. The phonon contribution to the thermal conductivity of AlB_2-type ceramics has a similar mechanism as other covalent and ionic bonded ceramics. That is to say that constructive and destructive phonon vibrations in the crystal lattice dominate the phonon contribution to thermal conductivity. The thermal conductivity for a typical oxide ceramic (Al_2O_3) is shown as a function of temperature in Figure 2.9, where there are four main temperature regimes, three of which are important for the present discussion.[100] The first is the initial rise in thermal conductivity due to the excitation of thermal vibrations, which allows phonons to transport thermal energy through the lattice. As a result, thermal conductivity increases in proportion to T^3. The second region is from ~40 K to the Debye temperature. This region extends from the temperature at which the value of thermal conductivity reaches a maximum and extends through its initial decrease. The decrease is a result of phonon-phonon interactions (also called Umklapp scattering). In this region, thermal conductivity is described by an exp($-\theta_D/2T$) relationship, where θ_D is the Debye temperature. The third region is for temperatures greater than the Debye temperature. In this region, all phonon modes are active and the phonon thermal conductivity changes in proportion to 1/T.[100]

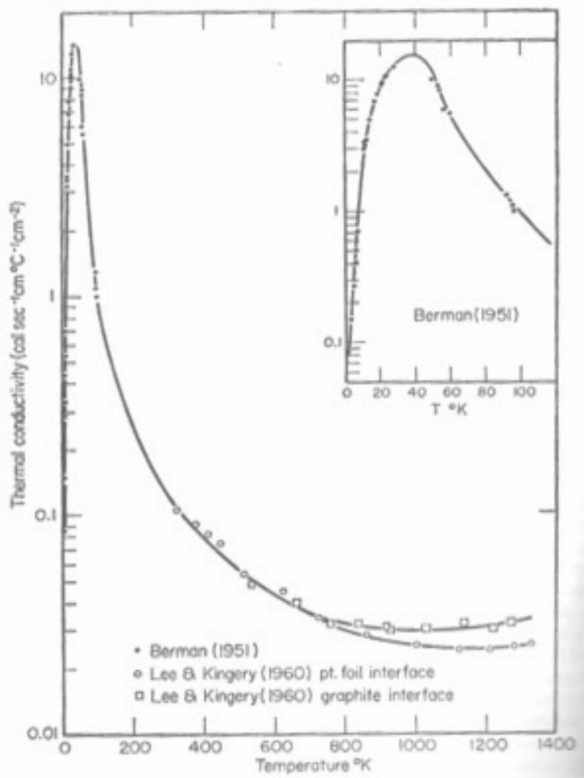

Figure 2.9: Thermal conductivity of single crystal Al_2O_3 over a wide temperature range.[100]

Of interest to the present research is the decrease in thermal conductivity dictated by Umklapp scattering of phonons. Using a classical gas model, the thermal conductivity can be calculated by equation 9, where, C_V is the heat capacity per volume, c is average velocity of a gas particle, and *l* is the mean free path (the distance between collisions).[101] The phonon thermal conductivity of a material from room temperature to the Debye temperature (discussed in detail later) can be expressed by equation 10, where λ_0 is a constant determined by the Bose-Einstein factor.[100] At temperatures much larger than the Debye temperature, the phonon contribution can be determined by equation 11, which shows a 1/T relationship.[100] For diborides, however, the phonon contribution to thermal conductivity is often small compared to the magnitude of the electron contribution. The phonon contribution is typically <1/3 the magnitude of the electron contribution at room temperature and decreases to <1/8 at 1000°C.[46]

$$\lambda_{Ph} = \frac{1}{3} C_V c l \tag{9}$$

$$\lambda_{Ph} = \lambda_0 e^{(-\theta_D/T)} \tag{10}$$

$$\lambda_{Ph} = \frac{B}{(2\pi)^3} \frac{M{\Omega_a}^{1/3} k_B^3 \theta_D^3}{\hbar^3 \gamma^2 T} \tag{11}$$

2.5.1.2. Electrons. The electron contribution to thermal conductivity arises from the metallic bonding in the AlB_2-type crystal structure in diborides. The free electron motion in the close packed layers of zirconium atoms gives rise to electronic conductivity, which is directly related to the electron contribution to thermal conductivity, shown in equation 12.[101] Equation 12 is called the Wiedemann-Franz law (sometimes referred to as the Wiedemann-Franz-Lorenz law), where L is the Lorenz number ($2.44 \times 10^{-8}\ V^2K^{-2}$) and σ is the electrical conductivity.[20,21,101] In the diborides, electron transfer dominates the thermal conductivity, >70% of the total thermal conductivity , which was described by Zhang et al. as shown in Figure 2.10.[92] Other researchers have found the electron contribution to be as low as 66% of the total thermal conductivity.[46,102] Due to the significance of electron transfer in diboride based ceramics, a more detailed description of the electrical properties is provided in Section 2.6.

$$\lambda_{el} = L\sigma T \tag{12}$$

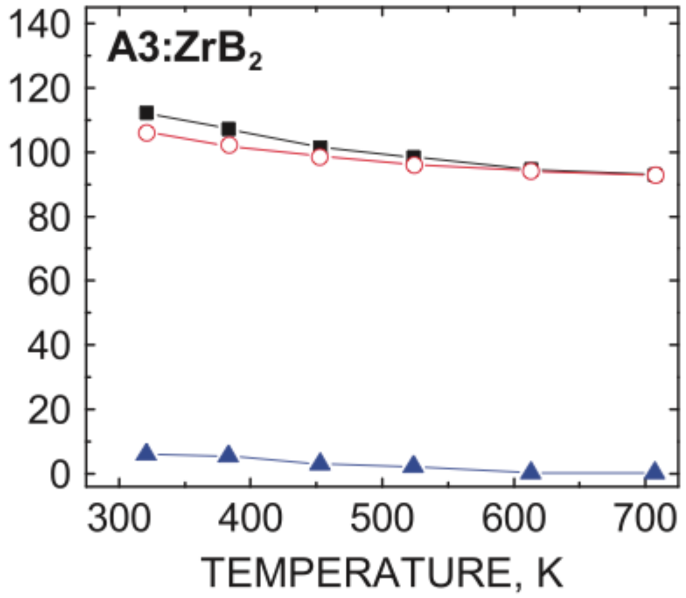

Figure 2.10: The total (squares) thermal conductivity of ZrB$_2$ separated into the electron (open circles) and phonon (triangles) contributions. The vertical axis is thermal conductivity with units of W/m•K.[92]

2.5.2. Heat Capacity. Heat capacity is the physical property that represents the amount of heat required to raise the temperature of a material.[98] Heat capacity can be described by the contribution of phonons and electrons, which have been described by the several models as discussed below. Thermodynamic principles can be used to relate the phonon component of constant volume (C_v) and constant pressure (C_p) heat capacities based on the partial differential of internal energy and enthalpy with respect to temperature, respectively (equations 13 and 14).[103]

$$C_v = \left(\frac{\partial \bar{U}}{\partial T}\right)_V \tag{13}$$

$$C_P = \left(\frac{\partial \bar{H}}{\partial T}\right)_P \tag{14}$$

The constant volume and constant pressure heat capacities can be related to each other by equation 15, where β is the volume expansion coefficient and γ is the Grüneisen parameter. The Grüneisen parameter is described by equation 16, where K is the bulk modulus and $\bar{V}$ is the molar volume.[99,103]

$$C_P = C_V(1 + \beta\gamma T) \tag{15}$$

$$\gamma = \frac{\beta K \bar{V}}{C_V} \tag{16}$$

2.5.2.1. Phonon contribution. Two models have been developed to explain how phonons contribute to the heat capacity of a material. Both of these models describe how phonon transfer in a lattice alters the energy required to raise the temperature of a material as a function of temperature. The first is the Einstein model shown in equation 17, where k_B is Boltzman's constant, ħ is Plank's constant divided by 2π, and ω_E is the Einstein frequency of independent, harmonic oscillating atoms.[103]

$$C_V = 3k_B \left(\frac{\hbar\omega_E}{k_B T}\right)^2 \frac{e^{\left(\hbar\omega_E/k_B T\right)}}{\left(e^{\left(\hbar\omega_E/k_B T\right)}-1\right)^2} \tag{17}$$

The second model, developed by Debye, shows a better correlation with experimental data, especially at lower temperatures (typically <200°C). This is because the Einstein model fails to describe how the heat capacity increases exponentially with increasing temperature, which is a result of independent, harmonic oscillating atoms.[103] The Debye model describes the interactions of oscillating atoms. The phonon contribution to the constant volume heat capacity is in equation 18, where N is the number of atoms per unit cell, R is the gas constant, θ_D is the Debye temperature, and x is the phonon energy ($\hbar\omega$) divided by the thermal energy ($k_B T$).[103] The Debye temperature is the temperature at which the maximum vibrational frequency of the lattice is achieved and can further be explained by equation 19, where h is Planck's constant, r is the number of atoms per formula unit, N_A is Avogadro's number, ρ is bulk density, M is the molar mass, and C_{sound} is Debye sound velocity.[101,103] The Debye temperatures for TiB_2, ZrB_2, and HfB_2 are 867°C, 637°C, and 417°C, respectively.[104]

$$C_V = 9NR\left(\frac{T}{\theta_D}\right)^3 \int_0^{\theta_D/T} \frac{x^4 e^x}{(e^x-1)^2}\,dx \tag{18}$$

$$\theta_D = \frac{\hbar}{2\pi k_B}\left(\frac{6\pi^2 r N_A \rho}{M}\right)^{1/3} C_{sound} \tag{19}$$

The Debye sound velocity can be expressed in terms of the shear modulus, G, bulk density, and Poisson's ratio, ν (equation 20).[103]

$$C_{sound} = \sqrt{G/\rho}\left(\frac{2}{3}+\frac{1}{3}\left[\frac{1-2\upsilon}{2(1-\upsilon)}\right]^{3/2}\right)^{-1/3} \tag{20}$$

2.5.2.2. Electron contribution. In addition to the contribution from phonons, free electrons can contribute to the heat capacity. Sommerfeld's electron theory of metals can describe the free electron contribution to heat capacity, shown in equation 21.[103] Where $N(E_F)$ is the electron density of states at the Fermi level. This expression for heat capacity can be simply represented as γT because all of the terms other than temperature are constant.

$$C_{el} = \frac{2\pi^2}{3} N(E_F) {k_B}^2 T \tag{21}$$

While this equation describes the behavior adequately at high temperatures (> Debye temperatures), the approach by Sommerfeld doesn't agree with experimental values of heat capacity below the Debye temperature. Other researchers noted that this was because of electron-phonon interactions, which were not considered in the model. The electron-phonon interactions change the value of $N(E_F)$ because the mass of an electron near the Fermi level (m_b) is different than that of a free electron (m), shown in equation 22, where $N_{fe}(E_F)$ is the density of states at the Fermi level for a free electron.[103] By including electron-phonon many-body corrections, the electron contribution to heat capacity can be shown simplistically by equation 23. Where γ_{el+ph} is the electron-phonon correction as a function of temperature.

$$N(E_F) = \frac{m_b}{m} N_{fe}(E_F) \tag{22}$$

$$C_{el} = \left(\gamma + \gamma_{el+ph}\right)T \tag{23}$$

2.5.2.3. Experimental measurements. Experimentally, heat capacity has been measured by a variety of methods, including: Differential Scanning Calorimetry (DSC),[105] laser flash,[97] and the liquid drop calorimetry setup.[106] The basic premise of calorimetry in the equilibrium state can be shown by equation 24, where ΔP is the absolute value of heat flow to the specimen, m is the specimen mass, and β is the rate of heating of the specimen.[105] In almost all cases, however, equilibrium is not maintained throughout the measurement (ie., the temperature of the specimen and/or the testing setup is not a constant value) and thus the measurement is made by comparing the heat required to raise the temperature of the specimen to that of a reference material.[105]

$$C_P = \frac{\Delta P}{m\beta} \tag{24}$$

Of particular interest to the research described in this thesis is the laser flash method for determining heat capacity.[97] This technique uses a laser to heat the specimen, and an IR detector measures the temperature rise on the back face of the specimen. Heat capacity by this method is described by equation 25, where L is the thickness, ΔT is the relative temperature rise, and ρ is the density of the material or reference.[107] The advantage of this method is that it may be carried out simultaneously with the laser flash thermal diffusivity measurement (described in the following section).

$$C_{P,m} = \frac{L_R \Delta T_R \rho_R}{L_m \Delta T_m \rho_m} C_{P,R} \quad (25)$$

2.5.3. Thermal Diffusivity. Due to the difficulty in measuring thermal conductivity directly, thermal diffusivity has been used with heat capacity and density to calculate thermal conductivity. Thermal conductivity, λ, can be calculated from the measured thermal diffusivity using equation 26, where α is thermal diffusivity, C_p is heat capacity, and ρ is the bulk density.[97] The advantage of using thermal diffusivity to calculate thermal conductivity is that the setup allows high temperature measurements to be completed using a single temperature measurement and accurately recording time versus forming an equilibrated temperature gradient at different temperatures.

$$\lambda = \alpha \rho C_p \quad (26)$$

Thermal diffusivity has commonly been measured using the laser flash technique originally developed by Parker et al.[108] This method is an ideal case that must meet several criteria to ensure that the values are meaningful[108]:

- The specimen is initially at a constant temperature
- Heat flow is one dimensional heat with no heat loss
- Uniform heat absorption occurs in a very thin layer on the surface of the specimen
- The pulse time of the heat source is infinitesimally small
- The material is fully homogenous
- The specimen properties are invariant as a function of temperature change with pulsed heat source

Parker et al. developed the laser flash technique by measuring and analyzing the rise in temperature on the back face of a specimen once exposed to an initial pulse of energy (sample geometry in Figure 2.11).[97,108] The energy pulse may be generated by a variety of sources including xenon flash lamps or high power lasers (class 1 lasers). Regardless of the initial energy source used, the temperature at any time or position in the specimen may be calculated by[108]:

$$T(x,t) = \frac{1}{L}\int_0^L T(x,t)dx + \frac{2}{L}\sum_{n=1}^{\infty}\left[e^{\left(\frac{-n^2\pi^2\alpha t}{L^2}\right)} \times \cos\left(\frac{n\pi x}{L}\right)\int_0^L T(x,0)\cos\left(\frac{n\pi x}{L}\right)dx\right] \quad (27)$$

where T is the temperature, x is the specimen thickness ($0 \leq x \leq L$), α is the thermal diffusivity, and t is the time.

Assuming that the initial energy pulse is instantaneous and uniformly absorbed, the layer thickness of the heat absorption is small with respect to the specimen thickness, and no radial heat loss, then the temperature on the back face of the sample can be calculated by[108]:

$$T(L,t) = \frac{Q}{\rho CL}\left[1 + 2\sum_{n=1}^{\infty}(-1)^n e^{\left(\frac{-n^2\pi^2\alpha t}{L}\right)}\right] \quad (28)$$

where Q is the pulse energy absorbed, ρ is the specimen density, and C is the specific heat capacity. Assuming a constant specimen thickness, the specimen back face temperature can be plotted as a function of time, Figure 2.12.[97] As can be seen in Figure 2.12, the temperature quickly rises after the pulse of energy to T_{max}, at which point the specimen slowly cools back to the initial temperature (not shown in the figure). Also, the time at half the maximum temperature, $\Delta T_{max}/2$, is recorded for future equations.[97]

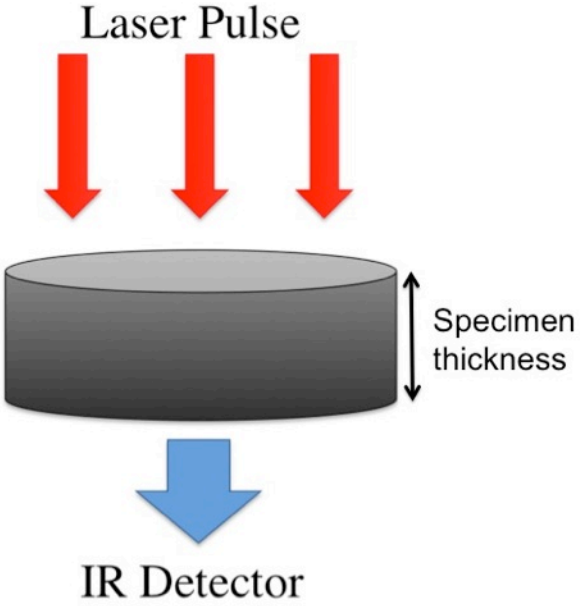

Figure 2.11: An idealized view of the specimen geometry illustrating the energy pulse on the front face and the radiant energy going to an infrared detector on the back face of the specimen.

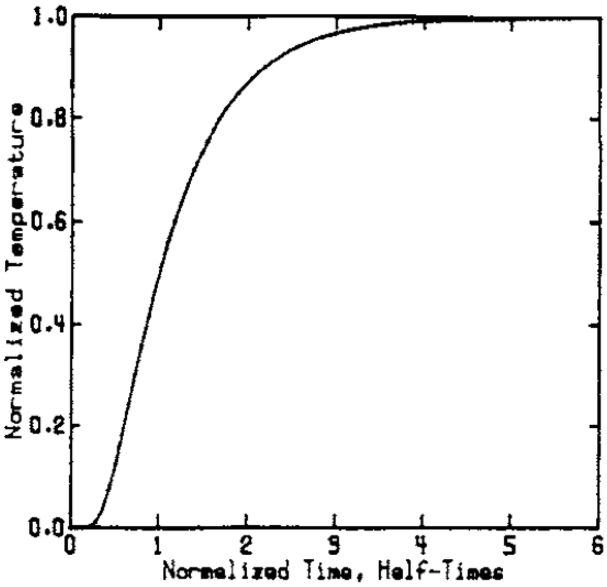

Figure 2.12: General appearance of the back face temperature of a specimen as a function of time.[97]

After measuring the back face temperature as a function of time, two dimensionless parameters can be defined: relative temperature (V(L,t)) and the thermal diffusivity constant (ω).[108] These can be shown as:

$$V(L,t) = \frac{T(L,t)}{T_{max}} \tag{29}$$

$$\omega = \frac{\pi^2 \alpha t}{L^2} \tag{30}$$

If equations (29) and (30) are substituted into equation (28), the relative temperature, V(L,t), is now related to the thermal diffusivity constant, ω.[108] The equation can be shown by:

$$V(L,t) = 1 + 2\sum_{n=1}^{\infty}(-1)^2 e^{(-n^2\omega)} \qquad (31)$$

The typical thermal diffusivity analysis using the Parker method defines the relative temperature as ½ (also referred to as the half-max temperature). Using a relative temperature of ½, ω is 1.38 and the thermal diffusivity can be calculated by Equation (32), such that the time t is now the time at half the maximum temperature ($t_{1/2}$) and L is the specimen thickness.[108]

$$\alpha = \frac{0.13879L^2}{t_{1/2}} \qquad (32)$$

Parker's approach to calculate thermal diffusivity is an idealized one, meaning that in practice, almost all of the initial assumptions are violated to some extent during a typical experiment.[97] As discussed below, several other approaches have been developed to mitigate the problems caused by Parker's assumptions. However, it is to be noted that no single approach corrects all of the deviations from the theoretical condition.

The separate approaches of Heckman, Cowan, and Koski have made significant progress with the issue of a laser pulse not being infinitesimally small.[109-111] In separate studies, Cowan and Koski modeled the laser flash as a block wave that was much shorter than the time to reach half the maximum temperature.[109,111] Along with the block wave assumption, radiative heat loss in the radial direction was also allowed. The resulting back-face temperature rise predicted using the Cowan or Koski models falls below that of Parker's method. In the limiting case of no heat loss, the correction factors for both models agree with that of Parker.[109,111] The work by Heckman assumed that the laser pulse width was similar to the time to reach half the maximum temperature. In this case, the pulse was assumed to be triangular in nature, starting small, increasing to a maximum and then decreasing, which was therefore dependent on finite pulse widths.[110] This resulted in the development of a semi-empirical correction table to adjust the time parameters used for the analysis.[110]

Clark and Taylor developed the most common method used to analyze the temperature rise curve and calculate the thermal diffusivity.[112-114] This method assumed radiative heat losses, which resulted in temperature changes on the back-face of the specimen that were not constant and decreased with time after reaching a maximum.[115] To correct the fit of the measured temperature rise curve, a factor was developed based on different values of time to reach different temperature rise values (ie. $0.2\Delta T$, $0.4\Delta T$, $0.8\Delta T$, etc.).[115] The correction factor resulted in better fits to both the peak in temperature and the resulting cooling portion of the curve compared to the previous methods of Heckman, Cowan, or Koski. The resulting value would then be used to modify the coefficient in equation 32.

2.6. ELECTRICAL PROPERTIES

Metal diboride ceramics with the AlB_2 structure have 1.33 free electrons per metal atom and the metal atoms are arranged in close packed planes within the crystal structure. This gives rise to metallic conduction, which is $>10^5$ S/cm for ZrB_2 and HfB_2.[7] This value is similar to metallic conductors such as Ni or Fe, and is many orders of magnitude higher than typical oxide ceramics (typically $<10^{-10}$ S/cm). Section 2.5.1.2 introduced the Weidman-Franz law that relates electrical conductivity to thermal conductivity. Because of their high electrical conductivity, the electron contribution to thermal conductivity is typically >67% of the total thermal conductivity while the phonon contribution is <33%.[92,94] This section will discuss how temperature and additives affect the electrical conductivity, and, therefore, the electron contribution to thermal conductivity.

Electrical conductivity in metallic conductors depends on the number of charge carriers and their mobility, which has been described by equation 33.[21,116] In this equation, e is the charge of an electron (the charge carrier in metallic conduction), n is the number of charge carriers, and μ is the mobility of the charge carriers. Because the charge on an electron is constant, impurities or additives can only change either the number of carriers or their mobility.[116] The mobility can further be described by equation 34, such that τ is the mean scattering time and m_e is the effective mass of an electron.[116] The mobility term now shows physical meaning, where the mean scattering time is the time between electron collisions and the mass of an electron is an understandable quantity. The following sections will discuss in more detail how the electrical conductivity changes with temperature and the presence of impurities.

$$\sigma = ne\mu \tag{33}$$

$$\mu = \frac{e\tau}{m_e} \tag{34}$$

2.6.1. Temperature Dependence. For a perfect crystal, the mean scattering time for electrons, τ, can be directly related to the inverse of temperature using the simple harmonic vibration of electrons. So, by combining equations 33 and 34, the electrical resistivity (the inverse of electrical conductivity), ρ, can be related to temperature, equation 35, where C is a constant carried over from the mean scattering time.[21] In equation 35, m_e, n, e, and C are all constant as a function of temperature. In this case, the resistivity becomes a linear function with respect to temperature for metallic conduction.[21]

$$\rho = \frac{1}{ne\mu} = \frac{m_e T}{ne^2 C} \tag{35}$$

2.6.2. Matthiessen's Rule. Real materials differ from perfect crystals due to the presence of impurities, lattice imperfections, additives, and other features that scatter electrons. Matthiessen developed an effective mobility term to account for scattering due to imperfections. His relation is shown in equation 36, where μ_L is the mobility due to lattice vibrations and μ_i is the mobility due to component i (ie. vacancies, impurity atoms, etc.).[116]

$$\frac{1}{\mu} = \frac{1}{\mu_L} + \sum_i \frac{1}{\mu_i} \tag{36}$$

From equation 35, the mobility term can be related to the transfer of electrons, which involves the electrical resistivity of a material. Unlike the overall electrical resistivity, not all of the potential differences from the perfect crystal are affected by temperature, such as the quantity and type of lattice defects and grain boundaries.[21,117,118] Matthiessen used this knowledge to develop equation 37, which was tailored to the case of metallic conduction.[116] In this equation, the first term, ρ_L is based on lattice vibrations and changes as function of temperature.[116] The second term relates to other defects such as vacancies, grain boundaries, etc. that are independent of temperature.[116]

$$\rho = \rho_L + \sum_i \rho_i \tag{37}$$

Equation 41 can be used to interpret electrical resistivity such as those measured by Tye and Clougherty and Samsonov as shown in Figure 2.13.[46,102] The data presented in Figure 2.13 show a linear trend of resistivity with temperature, as expected based on metallic conduction. The values of thermal conductivity also increase in the same manner (slope is constant) with temperature, while the absolute values of each different material depends on differences in processing, such as additives, grain size, etc.[116] In each case, the values increase or decrease based on porosity and non-interacting second phases, while the slope doesn't change significantly.

2.6.3. Mixing Rules for Particle Inclusions. For general cases where a second phase is added, a number of mixing models can be used to describe the electrical behavior of the resulting composite. The first is a simple volumetric mixing model shown by equation 38, where x is the volume fraction and ρ is the electrical resistivity of the continuous and discontinuous phases. This mixing model is for materials with similar electrical resistivity, with a second phase that is discontinuous and has no interaction with the continuous matrix phase. One example of this would be SiC-B_4C composites. However, this model does not predict resistivity well for materials with widely different electrical resistivity values, such as accounting for porosity or insulating particles in an electrically conducting matrix.

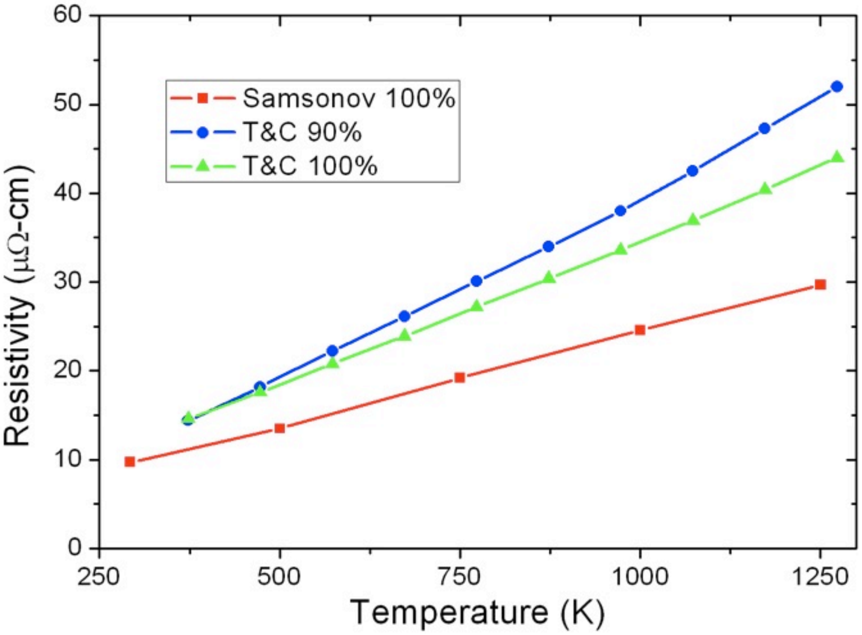

Figure 2.13: The electrical resistivity versus temperature for ZrB_2 with different densities and processing routes. Data provided by Tye and Clougherty, and Samsonov.[46,102] The lines are used to more easily show a linear relationship.

$$\rho_{eff} = x_d\rho_d + x_c\rho_c \tag{38}$$

When the electrical resistivity between the continuous phase and discontinuous phase are significantly different (i.e., a factor of 10 or more), the volumetric mixing model fails to predict resistivities. To more accurately predict electrical resistivity in these situations, two semi-empirical equations have been developed for mixtures with significant differences in electrical resistivity.[116,119,120] Equations 39 and 40 are specific to the cases where the electrical resistivity of the dispersed phase is greater than 10 times or less than 10 times that of the continuous phase, respectively.[116] In either of these cases, however, no single approach with mixing rules can account for a wide range of properties. As a result, a number of specialized models have been developed to account for a wide variety of interactions, properties, etc.[116-121]

$$\rho_{eff} = \rho_c \frac{(1+\frac{1}{2}x_d)}{(1-x_d)} \qquad (\rho_d > 10\rho_c) \qquad (39)$$

$$\rho_{eff} = \rho_c \frac{(1-x_d)}{(1+2x_d)} \qquad (\rho_d < 0.1\rho_c) \qquad (40)$$

2.6.4. Nordheim's Rule for Solid Solutions. If two metals with similar values of electrical resistivity are mixed, the electrical resistivity of the resulting solid solution can be higher than either constituent.[116] This arises from having two elements with different electron contributions and/or number of electron shells. Similarly, this phenomenon has been observed by Juretschke and Steinitz in the case of diborides.[122] Figure 2.14 shows that solid solutions of TiB_2/VB_2 and ZrB_2/NbB_2 have higher electrical resistivities than the pure materials.[122] Further, each of the pure materials has similar values and the overall electrical resistivity is similar to a so called "bell curve," where the maximum occurs near 50 mol%.[122]

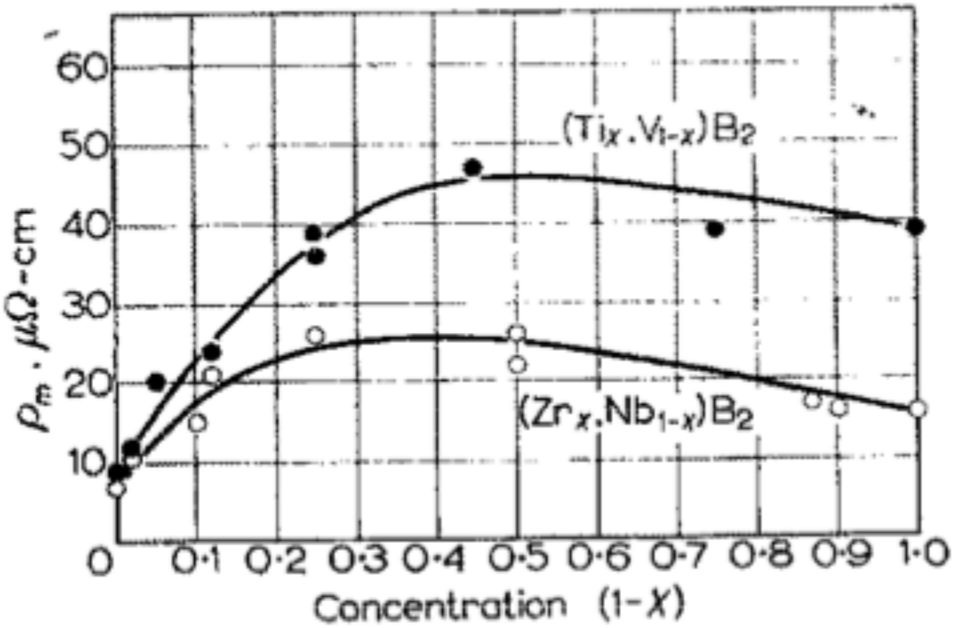

Figure 2.14: Electrical resistivity as a function of the concentration of VB_2 or NbB_2 in mole fraction showing a bell curve type plot.[122]

The behavior shown in Figure 2.14 can be described by Nordheim's rule for solid solutions, which attributes the increase in resistivity to electron scattering with solute atom electrons.[116,122] The case where each end-member has a similar number of electrons can be described by equation 45, where the resistivity is dependent on the resistivity of each constituent (ρ), the volume fraction of solid solution additive (x), and the Nordheim coefficient (c).[116] However, when the two constituents contribute a different number of electrons per atom, as shown in Figure 2.14, the maximum electrical resistivity is shifted from the 50% addition.[16,116] This requires knowledge of both the number of electrons per atom and the mobility of electrons in each of the constituents in order to identify an additional parameter with physical meaning.[122] However, a correction factor can be added to equation 41 to match experimental data.[116] While correction factors have been determined for some metallic systems such as nickel or chromium,[123] these have not been reported for non-metals such as diborides.

$$\rho = x_a\rho_a + (1 - x_a)\rho_b + cx_a(1 - x_a) \tag{41}$$

REFERENCES

1. W. G. Fahrenholtz, G. E. Hilmas, I. G. Talmy, and J. A. Zaykoski, "Refractory Diborides of Zirconium and Hafnium," *J. Am. Ceram. Soc.,* **90** [5] 1347-64 (2007).

2. X. Zhang, X. Luo, J. Han, J. Li, and W. Han, "Electronic structure, elasticity and hardness of diborides of zirconium and hafnium: First principles calculations," *Computational Materials Science,* **44** [2] 411-21 (2008).

3. R.A. Cutler, "Engineering Properties of Borides," pp. 787-803 in Vol. 4, *Ceramics and Glasses: Engineered Materials Handbook.* Edited by S. J. S. Jr. ASM International, Materials Park, OH, 1991.

4. L.S. Sigl, R. Telle, and K. Takagi, "Boride-Based Hard Materials," pp. 802-945 in *Handbook of Ceramic Hard Materials.* Edited by R. Riedel. Wiley-VCH, Weinheim, Germany, 2000.

5. M.M. Opeka, I.G. Talmy, and J.A. Zaykoski, "Oxidation-based materials selection for 2000C + hypersonic aerosurfaces: Theoretical considerations and historical experience: Special Section: Ultra-High Temperature Ceramics (Guest Editors: Joan Fuller and Michael D. Sacks)," *Journal of Materials Science,* **39** 5887-904 (2004).

6. ACerS-NIST, Phase Equilibria Diagrams, [Computer Program] ACerS-NIST Phase Equilibria for Ceramics Program, 2004.

7. W.G. Fahrenholtz, G.E. Hilmas, I.G. Talmy, and J.A. Zaykoski, "Refractory Diborides of Zirconium and Hafnium," *J. Am. Ceram. Soc.,* **90** [5] 1347-64 (2007).

8. S.M. Johnson, S.E. Beckman, E.B. Irby, M.J. Gasch, and M.I. Gusman, in the 9th Bienniel Congress on Refractories, (UNITECR, ed.), Orlando, FL, 2005.

9. S. Zhu, W.G. Fahrenholtz, G.E. Hilmas, and S.C. Zhang, "Pressureless Sintering of Zirconium Diboride Using Boron Carbide and Carbon Additions," *J. Am. Ceram. Soc.,* **90** [11] 3660-3 (2007).

10. V. Skorokhod and V.D. Krstic, "High strength-high toughness B_4C-TiB_2 composites," *J. Mater. Sci. Lett.,* **19** [3] 237-9 (2000).

11. W.-B. Tian, Y.-M. Kan, G.-J. Zhang, and P.-L. Wang, "Effect of carbon nanotubes on the properties of ZrB_2-SiC ceramics," *Materials Science and Engineering: A,* **487** [1-2] 568-73 (2008).

12. S. Zhu, W.G. Fahrenholtz, G.E. Hilmas, and S.C. Zhang, "Pressureless sintering of carbon-coated zirconium diboride powders," *Materials Science and Engineering: A,* **459** [1-2] 167-71 (2007).

13. E.V. Clougherty and R.L. Pober, "Physical and Mechanical Properties of Transition Metal Diborides," *IMD Spec. Rep. Ser.,* **10** [13] 423-44 (1964).

14. T. Lundstrom, "Structure, Defects, and Properties of Some Refractory Borides," *Pure Appl. Chem.,* **57** [10] 1383-90 (1985).

15. J.K. Burdett, E. Canadell, and G.J. Miller, "Electronic structure of transition-metal borides with the AlB_2 structure," *J. Am. Chem. Soc.,* **108** [21] 6561-8 (1986).

16. P. Vajeeston, P. Ravindran, C. Ravi, and R. Asokamani, "Electronic structure, bonding, and ground-state properties of AlB_2-type transition-metal diborides," *Physical Review B,* **63** [4] 045115 (2001).

17. G P Shveikin, "The Chemical Bonding and Electronic Properties of Metal Borides," *Russian Chemical Reviews,* **63** [9] 711-34 (1994).

18. X.-Q. Chen, C.L. Fu, M. Krccaronmar, and G.S. Painter, "Electronic and Structural Origin of Ultraincompressibility of 5d Transition-Metal Diborides MB_2 (M=W, Re, Os)," *Phys. Rev. Lett.,* **100** [19] 196403 (2008).

19. Y. Tomida, S. Nitta, S. Kamiyama, H. Amano, I. Akasaki, S. Otani, H. Kinoshita, R. Liu, A. Bell, and F.A. Ponce, "Growth of GaN on ZrB_2 substrate by metal-organic vapor phase epitaxy," *Appl. Surf. Sci.,* **216** [1-4] 502-7 (2003).

20. L. Solymar and D. Walsh, *Electrical Properties of Materials,* 7 ed. Oxford University Press Inc., New York, 2004.

21. D. Jiles, *Introduction to the Electronic Properties of Materials,* 2 ed. Nelson Thornes Ltd, United Kingdom, 2001.

22. S. Baik and P.F. Becher, "Effect of Oxygen Contamination on Densification of TiB2," *J. Am. Ceram. Soc.,* **70** [8] 527-30 (1987).

23. M.S. Jensen, M.-A. Einarsrud, and T. Grande, "Preferential Grain Orientation in Hot Pressed TiB_2,"*J. Am. Ceram. Soc.,* **90** [4] 1339-41 (2007).

24. M. Brochu, B.D. Gauntt, L. Boyer, and R.E. Loehman, "Pressureless reactive sintering of ZrB2 ceramic," *Journal of the European Ceramic Society,* **29** [8] 1493-9 (2009).

25. A.L. Chamberlain, W.G. Fahrenholtz, and G.E. Hilmas, "Pressureless Sintering of Zirconium Diboride," *J. Am. Ceram. Soc.,* **89** [2] 450-6 (2006).

26. L. Rangaraj, C. Divakar, and V. Jayaram, "Processing of Refractory Metal Borides, Carbides and Nitrides," *Key Eng. Mater.,* **395** 69-88 (2008).

27. S. C. Zhang, G. E. Hilmas, and W. G. Fahrenholtz, "Pressureless Densification of Zirconium Diboride with Boron Carbide Additions," *J. Am. Ceram. Soc.,* **89** [5] 1544-50 (2006).

28. T.A. Parthasarathy, R.A. Rapp, M. Opeka, and R.J. Kerans, "Effects of Phase Change and Oxygen Permeability in Oxide Scales on Oxidation Kinetics of ZrB_2 and HfB_2," *J. Am. Ceram. Soc.,* **92** 1079-86 (2009).

29. L. Silvestroni and D. Sciti, "Effects of $MoSi_2$ additions on the properties of Hf- and ZrB_2 composites produced by pressureless sintering," *Scripta Materialia,* **57** [2] 165-8 (2007).

30. William G. Fahrenholtz, Gregory E. Hilmas, Shi C. Zhang, and Sumin Zhu, "Pressureless Sintering of Zirconium Diboride: Particle Size and Additive Effects," *J. Am. Ceram. Soc.,* **91** [5] 1398-404 (2008).

31. T.A. Parthasarathy, R.A. Rapp, M. Opeka, and R.J. Kerans, "A model for the oxidation of ZrB_2, HfB_2 and TiB_2," *Acta Materialia,* **55** [17] 5999-6010 (2007).

32. D.A. Ray, S. Kaur, R.A. Cutler, and D.K. Shetty, "Effect of Additives on the Activation Energy for Sintering of Silicon Carbide," *J. Am. Ceram. Soc.,* **91** [4] 1135-40 (2008).

33. S.C. Zhang, G.E. Hilmas, and W.G. Fahrenholtz, "Pressureless Densification of Zirconium Diboride with Boron Carbide Additions," *J. Am. Ceram. Soc.,* **89** [5] 1544-50 (2006).

34. D. Sciti, A. Balbo, and A. Bellosi, "Oxidation behaviour of a pressureless sintered HfB_2-$MoSi_2$ composite," *Journal of the European Ceramic Society,* **29** [9] 1809-15 (2009).

35. L. Silvestroni, D. Sciti, and A. Bellosi, "Microstructure and properties of pressureless sintered HfB_2-based composites with additions of ZrB_2 or HfC," *Advanced Engineering Materials,* **9** [10] 915-20 (2007).

36. X.-J. Zhou, G.-J. Zhang, Y.-G. Li, Y.-M. Kan, and P.-L. Wang, "Hot pressed ZrB_2-SiC-C ultra high temperature ceramics with polycarbosilane as a precursor," *Mater. Lett.,* **61** [4-5] 960-3 (2007).

37. F. Peng and R.F. Speyer, "Oxidation Resistance of Fully Dense ZrB_2 with SiC, TaB_2, and $TaSi_2$ Additives," *J. Am. Ceram. Soc.,* **91** [5] 1489-94 (2008).

38. M. Gasch, D. Ellerby, E. Irby, S. Beckman, M. Gusman, and S. Johnson, "Processing, properties and arc jet oxidation of hafnium diboride/silicon carbide ultra high temperature ceramics: Special Section: Ultra-High Temperature Ceramics (Guest Editors: Joan Fuller and Michael D. Sacks)," *Journal of Materials Science,* **39** 5925-37 (2004).

39. S.K. Mishra, A.K. Ray, P. Ramachandrarao, "Effect of Fe and Cr Addition on the Sintering Behavior of ZrB_2 Produced by Self-Propagating High-Temperature Synthesis," *J. Am. Ceram. Soc.,* **85** [11] 2846-8 (2002).

40. M. Gasch, S. Johnson, and J. Marschall, "Thermal Conductivity Characterization of Hafnium Diboride-Based Ultra-High-Temperature Ceramics," *J. Am. Ceram. Soc.,* **91** [5] 1423-32 (2008).

41. J. Zou, S.-K. Sun, G.-J. Zhang, Y.-M. Kan, P.-L. Wang, and T. Ohji, "Chemical Reactions, Anisotropic Grain Growth and Sintering Mechanisms of Self-Reinforced ZrB_2–SiC Doped with WC," *J. Am. Ceram. Soc.,* **94** [5] 1575-83 (2011).

42. E.V. Clougherty, R.J. Hill, W.H. Rhodes, and E.T. Peters, *Research and Development of Refractory Oxidation-Resistant Diborides. Part 2, Volume 2: Processing and Characterization*. 2003.

43. M.M. Opeka, I.G. Talmy, E.J. Wuchina, J.A. Zaykoski, and S.J. Causey, "Mechanical, Thermal, and Oxidation Properties of Refractory Hafnium and Zirconium Compounds," *Journal of the European Ceramic Society,* **19** 2405-14 (1999).

44. A.L. Chamberlain, W.G. Fahrenholtz, G.E. Hilmas, and D.T. Ellerby, "High-Strength Zirconium Diboride-Based Ceramics," *J. Am. Ceram. Soc.,* **87** [6] 1170-2 (2004).

45. W.D. Kingery, "Factors Affecting Thermal Stress Resistance of Ceramic Materials," *J. Am. Ceram. Soc.,* **38** [1] 3-15 (1955).

46. R.P. Tye and E.V. Clougherty, "The Thermal and Electrical Conductivities of some Electrically Conducting Compounds," *Proceedings of the Fifth Symposium on Thermophysical Properties,* 396-401 (1970).

47. E.V. Clougherty, K.E. Wilkes, and R.P. Tye, "Research and Development of Refractory Oxidation-Resistant Diborides. Part 2, Volume 5: Thermal, Physical, Electrical and Optical Properties " *AFML-TR-68-190, Wright-Patterson Air Force Base,* (1969).

48. D. Sciti, L. Silvestroni, S. Guicciardi, D.D. Fabbriche, and A. Bellosi, "Processing, mechanical properties and oxidation behavior of TaC and HfC composites containing 15 vol% $TaSi_2$ or $MoSi_2$," *Journal of Materials Research,* **24** [6] 2056-65 (2009).

49. D. Sciti, M. Brach, and A. Bellosi, "Long-term oxidation behavior and mechanical strength degradation of a pressurelessly sintered ZrB_2-$MoSi_2$ ceramic," *Scripta Materialia,* **53** [11] 1297-302 (2005).

50. S. Guo, Y. Kagawa, T. Nishimura, and H. Tanaka, "Thermal and Electric Properties in Hot-Pressed ZrB_2-$MoSi_2$-SiC Composites," *J. Am. Ceram. Soc.,* **90** [7] 2255-8 (2007).

51. M.N. Rahaman, *Ceramic Processing and Sintering,* 2 ed. CRC Press, Boca Raton, FL, 2003.

52. David Kalish and Edward V. Clougherty, "Densification Mechanisms in High-pressure Hot-Pressing of HfB_2," *J. Am. Ceram. Soc.,* **52** [1] 26-30 (1969).

53. W.G. Fahrenholtz, G.E. Hilmas, S.C. Zhang, and S. Zhu, "Pressureless Sintering of Zirconium Diboride: Particle Size and Additive Effects," *J. Am. Ceram. Soc.,* **91** [5] 1398-404 (2008).

54. D. Sciti, F. Monteverde, S. Guicciardi, G. Pezzotti, and A. Bellosi, "Microstructure and mechanical properties of ZrB_2-$MoSi_2$ ceramic composites produced by different sintering techniques," *Materials Science and Engineering: A,* **434** [1-2] 303-9 (2006).

55. D. Sciti, L. Silvestroni, G. Celotti, C. Melandri, and S. Guicciardi, "Sintering and Mechanical Properties of ZrB_2–$TaSi_2$ and HfB_2–$TaSi_2$ Ceramic Composites," *J. Am. Ceram. Soc.,* **91** [10] 3285-91 (2008).

56. E. A. Olevsky, V. Tikare, and T. Garino, "Multi-Scale Study of Sintering: A Review," *J. Am. Ceram. Soc.,* **89** [6] 1914-22 (2006).

57. S.S. Hwang, A.L. Vasiliev, and N.P. Padture, "Improved processing and oxidation-resistance of ZrB_2 ultra-high temperature ceramics containing SiC nanodispersoids," *Materials Science and Engineering: A,* **464** [1-2] 216-24 (2007).

58. F. Monteverde, "Ultra-high temperature HfB_2-SiC ceramics consolidated by hot-pressing and spark plasma sintering," *J. Alloys Compd.,* **428** [1-2] 197-205 (2007).

59. R.S. Dobedoe, G.D. West, and M.H. Lewis, "Spark plasma sintering of ceramics: understanding temperature distribution enables more realistic comparison with conventional processing," *Advances in Applied Ceramics,* **104** 110-6 (2005).

60. T. Venkateswaran, B. Basu, G.B. Raju, and D.-Y. Kim, "Densification and properties of transition metal borides-based cermets via spark plasma sintering," *Journal of the European Ceramic Society,* **26** [13] 2431-40 (2006).

61. Z. Munir, U. Anselmi-Tamburini, and M. Ohyanagi, "The effect of electric field and pressure on the synthesis and consolidation of materials: A review of the spark plasma sintering method," *Journal of Materials Science,* **41** [3] 763-77 (2006).

62. E. Olevsky and L. Froyen, "Constitutive modeling of spark-plasma sintering of conductive materials," *Scripta Materialia,* **55** [12] 1175-8 (2006).

63. E.A. Olevsky, S. Kandukuri, and L. Froyen, "Consolidation enhancement in spark-plasma sintering: Impact of high heating rates," *Journal of Applied Physics,* **102** [11] 114913-12 (2007).

64. E.A. Olevsky, V. Tikare, and T. Garino, "Multi-Scale Study of Sintering: A Review," *J. Am. Ceram. Soc.,* **89** [6] 1914-22 (2006).

65. D. Tiwari, B. Basu, and K. Biswas, "Simulation of thermal and electric field evolution during spark plasma sintering," *Ceramics International,* **35** [2] 699-708 (2009).

66. W.-W. Wu, G.-J. Zhang, Y.-M. Kan, P.-L. Wang, K. Vanmeensel, J. Vleugels, and O. Van der Biest, "Synthesis and microstructural features of ZrB_2-SiC-based composites by reactive spark plasma sintering and reactive hot pressing," *Scripta Materialia,* **57** [4] 317-20 (2007).

67. I. Akin, M. Hotta, F.C. Sahin, O. Yucel, G. Goller, and T. Goto, "Microstructure and densification of ZrB_2-SiC composites prepared by spark plasma sintering," *Journal of the European Ceramic Society,* **29** [11] 2379-85 (2009).

68. H. Wang, C. Wang, X. Yao, and D. Fang, "Processing and Mechanical Properties of Zirconium Diboride-Based Ceramics Prepared by Spark Plasma Sintering," *J. Am. Ceram. Soc.,* **90** [7] 1992-7 (2007).

69. H. Wang, C.-A. Wang, X. Yao, and D. Fang, "Processing and Mechanical Properties of Zirconium Diboride-Based Ceramics Prepared by Spark Plasma Sintering," *J. Am. Ceram. Soc.,* **90** [7] 1992-7 (2007).

70. S.-Q. Guo, T. Nishimura, Y. Kagawa, and J.-M. Yang, "Spark Plasma Sintering of Zirconium Diborides," *J. Am. Ceram. Soc.,* **91** [9] 2848-55 (2008).

71. A. Bellosi, F. Monteverde, and D. Sciti, "Fast Densification of Ultra-High-Temperature Ceramics by Spark Plasma Sintering," *International Journal of Applied Ceramic Technology,* **3** [1] 32-40 (2006).

72. T. Tsuchida and S. Yamamoto, "MA-SHS and SPS of ZrB_2-ZrC composites," *Solid State Ionics,* **172** [1-4] 215-6 (2004).

73. J.B. Wachtman, *Mechanical Properties of Ceramics*. John Wiley & Sons, Inc., New York, 1996.

74. ASTM C1161, "Standard Test Method for Flexural Strength of Advanced Ceramics at Ambient Temperature," *ASTM International,* (2002).

75. A. Rezaie, W.G. Fahrenholtz, and G.E. Hilmas, "Effect of hot pressing time and temperature on the microstructure and mechanical properties of ZrB_2-SiC," *Journal of Materials Science,* **42** [8] 2735-44 (2007).

76. J.R. Fenter, "Refractory Diborides as Engineering Materials," *SAMPE Quarterly,* [2] 1-15 (1971).

77. F. Monteverde, S. Guicciardi, and A. Bellosi, "Advances in microstructure and mechanical properties of zirconium diboride based ceramics," *Mater. Sci. Eng., A,* **346** [1-2] 310-9 (2003).

78. J.W. Zimmermann, "Improving the Thermal Shock Resistance of Zirconium Diboride Ceramics"; Ceramic Engineering Thesis. University of Missouri-Rolla, Rolla, MO, 2007.

79. J.W. Zimmermann, G.E. Hilmas, and W.G. Fahrenholtz, "Thermal Shock Resistance and Fracture Behavior of ZrB2–Based Fibrous Monolith Ceramics," *J. Am. Ceram. Soc.,* **92** [1] 161-6 (2009).

80. A. Balbo and D. Sciti, "Spark plasma sintering and hot pressing of ZrB_2-$MoSi_2$ ultra-high-temperature ceramics," *Materials Science and Engineering: A,* **475** [1-2] 108-12 (2008).

81. S.-Q. Guo, Y. Kagawa, T. Nishimura, D. Chung, and J.-M. Yang, "Mechanical and physical behavior of spark plasma sintered ZrC-ZrB_2-SiC composites," *Journal of the European Ceramic Society,* **28** [6] 1279-85 (2008).

82. T. Tsuchida and S. Yamamoto, "Spark plasma sintering of ZrB_2-ZrC powder mixtures synthesized by MA-SHS in air," *Journal of Materials Science,* **42** [3] 772-8 (2007).

83. W.-M. Guo, J. Vleugels, G.-J. Zhang, P.-L. Wang, and O. Van der Biest, "Effect of heating rate on densification, microstructure and strength of spark plasma sintered ZrB_2-based ceramics," *Scripta Materialia,* **62** [10] 802-5 (2010).

84. B. Basu, T. Venkateswaran, and D.-Y. Kim, "Microstructure and Properties of Spark Plasma-Sintered ZrO_2–ZrB_2 Nanoceramic Composites," *J. Am. Ceram. Soc.,* **89** [8] 2405-12 (2006).

85. D. Sciti, S. Guicciardi, A. Bellosi, and G. Pezzotti, "Properties of a Pressureless-Sintered ZrB_2–$MoSi_2$ Ceramic Composite," *J. Am. Ceram. Soc.,* **89** [7] 2320-2 (2006).

86. M.K. Ferber, P.F. Becher, and C.B. Finch, "Effect of Microstructure on the Properties of TiB_2 Ceramics," *J. Am. Ceram. Soc.,* **66** [1] C-2-C-3 (1983).

87. J.J. MelÈndez-MartÌnez, A. DomÌnguez-RodrÌguez, F. Monteverde, C. Melandri, and G. de Portu, "Characterisation and high temperature mechanical properties of zirconium boride-based materials," *Journal of the European Ceramic Society,* **22** [14-15] 2543-9 (2002).

88. S. Zhu, W.G. Fahrenholtz, and G.E. Hilmas, "Influence of silicon carbide particle size on the microstructure and mechanical properties of zirconium diboride-silicon carbide ceramics," *Journal of the European Ceramic Society,* **27** [4] 2077-83 (2007).

89. J.W. Zimmermann, G.E. Hilmas, W.G. Fahrenholtz, F. Monteverde, and A. Bellosi, "Fabrication and properties of reactively hot pressed ZrB_2-SiC ceramics," *Journal of the European Ceramic Society,* **27** [7] 2729-36 (2007).

90. L. Weng, X. Zhang, J. Han, W. Han, and C. Hong, "The effect of B_4C on the microstructure and thermo-mechanical properties of HfB_2-based ceramics," *J. Alloys Compd.,* **473** [1-2] 314-8 (2009).

91. L.S. Sigl and H.-J. Kleebe, "Microcracking in B_4C-TiB_2 Composites," *J. Am. Ceram. Soc.,* **78** [9] 2374-80 (1995).

92. L. Zhang, D.A. Pejaković, J. Marschall, and M. Gasch, "Thermal and Electrical Transport Properties of Spark Plasma-Sintered HfB_2 and ZrB_2 Ceramics," *J. Am. Ceram. Soc.,* **94** [8] 2562-70 (2011).

93. R.G. Munro, "Material Properties of Titanium Diboride," *Journal of Research of the National Institute of Standards and Technology,* **105** 709-20 (2000).

94. J.W. Zimmermann, G.E. Hilmas, W.G. Fahrenholtz, R.B. Dinwiddie, W.D. Porter, and H. Wang, "Thermophysical Properties of ZrB_2 and ZrB_2-SiC Ceramics," *J. Am. Ceram. Soc.,* **91** [5] 1405-11 (2008).

95. P. Jeschke, "Thermal Conductivity of Refractories: Working with the Hot-Wire Method," pp. 172-85 in *Thermal Transmission Measurements of Insulation, ASTM STP 660.* Edited by R. P. Tye. American Society for Testing and Materials, 1978.

96. ASTM C177, "Standard Test Method for Steady-State Heat Flux Measurements and Thermal Transmission Properties by Means of the Guarded-Hot-Plate Apparatus," *ASTM International,* (2010).

97. ASTM E1461, "Standard Test Method for Thermal Diffusivity of Solids by the Flash Method," *ASTM International,* (2001).

98. J.P. Holman, *Heat Transfer,* 7 ed. McGraw-Hill Companies, 1990.

99. N. Kaur, R. Mohan, N.K. Gaur, and R.K. Singh, "Cohesive and thermal properties of transition metal diborides," *Physica B: Condensed Matter,* **404** [8-11] 1607-10 (2009).

100. W.D. Kingery, H.K. Bowen, and D.R. Uhlmann, *Introduction to Ceramics*. Wiley-Interscience, 1976.

101. G. Grimvall, *Electric Refractory Materials*. Edited by Y. Kumashiro. Marcel Dekker, Inc., New York, 2000.

102. G.V. Samsonov, B.A. Kovenskaya, and T.I. Serebryakova, "Some physical characteristics of the diborides of transition metals of groups IV and V," *Russian Physics Journal,* **14** [1] 11-4 (1971).

103. G. Grimvall, *Thermophysical properties of materials;* North Holland, 1986.

104. D.E. Wiley, W.R. Manning, and O. Hunter Jr, "Elastic properties of polycrystalline TiB_2, ZrB_2 and HfB_2 from room temperature to 1300 K," *Journal of the Less Common Metals,* **18** [2] 149-57 (1969).

105. ASTM E1269, "Standard Test Method for Determining Specific Heat Capacity by Differential Scanning Calorimetry," *ASTM International,* (2011).

106. ASTM D4611, "Standard Test Method for Specific Heat of Rock and Soil," *ASTM International,* (2008).

107. K. Shinzato and T. Baba, "A Laser Flash Apparatus for Thermal Diffusivity and Specific Heat Capacity Measurements," *J. Therm. Anal. Calorim.,* **64** 413-22 (2001).

108. W.J. Parker, R.J. Jenkins, C.P. Butler, and G.L. Abbott, "Flash Method of Determining Thermal Diffusivity, Heat Capacity, and Thermal Conductivity," *Journal of Applied Physics,* **32** [9] 1679-84 (1961).

109. R.D. Cowan, "Pulse method of measuring thermal diffusivity at high temperatures," *Journal of Applied Physics,* **34** [4] 926-7 (1963).

110. R.C. Heckman, *Error Analysis of the Flash Thermal Diffusivity Technique,* Vol. 14. Edited by P. G. Klemens and T. K. Chu. Eds. Plenum Publishing Corp., NY, 1974.

111. J.A. Koski, in 8th Symposium on Thermophysical Properties, p. 94. The American Society of Mechanical Engineers, New York, 1981.

112. L. Kehoe, P.V. Kelly, and G.M. Crean, "Application of the laser flash diffusivity method to thin high thermal conductivity materials," *Microsystem Technologies,* **5** [1] 18-21 (1998).

113. J.L. Rempe and D.L. Knudson, "High temperature thermal properties for metals used in LWR vessels," *J. Nucl. Mater.,* **372** [2-3] 350-7 (2008).

114. A.J. Whittaker, R. Taylor, and H. Tawil, "Thermal Transport Properties of Carbon-Carbon Fibre Composites I. Thermal Diffusivity Measurements," *Proceedings: Mathematical and Physical Sciences,* **430** [1878] 167-81 (1990).

115. L.M. Clark and R.E. Taylor, "Radiation loss in the flash method for thermal diffusivity," *Journal of Applied Physics,* **46** [2] 714-9 (1975).

116. S.O. Kasap, *Principles of Electrical Engineering Materials and Devices*. McGraw-Hill, Boston, 1997.

117. J.C. Maxwell, *A Treatise of Electricity and Magnetism,* Vol. 1. Oxford University Press, Oxford, 1904.

118. M. Zulfequar and A. Kumar, "Effect of Porosity on Electrical Conductiity of Hot Pressed AlN Ceramic," *Revue De Physique Appliquee,* **21** [9] 525-9 (1986).

119. J.A. Reynolds and J.M. Hough, *Proceedings of the Physical Society,* Vol. 70, no. 769. London, 1957.

120. P.L. Rossiter, *The Electrical Resistivity of Metals and Alloys*. Cambridge University Press, Cambridge, 1987.

121. D.A.G. Bruggeman, "Berechnung verschiedener physikalischer Konstanten von heterogenen Substanzen. I. Dielektrizita tskonstanten und Leitfa ¨ higkeiten der Mischko ¨ rper aus isotropen Substanzen," Ann," *Phys. (Leipzig,* **24** 636-79 (1935).

122. H.J. Juretschke and R. Steinitz, "Hall Effect and Electrical Conductivity of Transition-Metal Diborides," *J. Phys. Chem. Solids,* **4** [1-2] 118-27 (1957).

123. Y. Terada, K. Ohkubo, T. Mohri, and T. Suzuki, *Thermal conductivity in nickel solid solutions,* Vol. 81*;* pp. 2263-8. AIP, 1997.

PAPER

1. EFFECT OF STARTING PARTICLE SIZE AND OXYGEN CONTENT ON DENSIFICATION OF ZrB_2

Matthew Thompson*, William G. Fahrenholtz, Greg Hilmas
Dept. of Materials Science & Engineering
Missouri University of Science and Technology

Abstract

Zirconium diboride (ZrB_2) ceramics were densified by pressureless sintering, hot pressing, or spark plasma sintering of powders with a range of starting particle sizes and oxygen contents. Microstructural analysis of the ZrB_2 ceramics revealed a wide range of final grain sizes. Spark plasma sintering resulted in an average grain size as small as 1.6 μm after densification at 1900°C, while the largest grains, 31 μm, were produced by pressureless sintering at 2100°C. Oxygen impurities in boride ceramics caused grain coarsening in all densification techniques, but inhibited full densification only for pressureless sintering. Carbon was added to react with and remove oxygen impurities, which promoted densification, reduced ZrB_2 grain size, and led to increased room temperature flexure strengths. The highest strength was 527 MPa for spark plasma sintered ZrB_2 while the lowest strength was measured for pressurelessly sintered ZrB_2,

300 MPa. Overall, spark plasma sintering was the superior technique for providing the highest strength and greatest ability to remove oxygen.

Introduction

Zirconium diboride (ZrB_2) is an ultra high temperature ceramic that has strong covalent bonding, which gives it a high melting temperature (3250°C[1]), high hardness (23 GPa)[2], and high elastic modulus (>500 GPa experimentally, 546 GPa theoretically[3]). The compound also has significant metallic character to its bonding, which results in high thermal (60 W/m•K or higher) and electrical (10^7 S/m) conductivities[4]. With this unusual combination of properties, ZrB_2 shows promise for diverse applications such as cutting tools, molten metal crucibles, and thermal protection systems for hypersonic aerospace vehicles.[5]

Densification of TiB_2, ZrB_2, and HfB_2 (generically designated as MeB_2 here) is affected by oxygen impurities that are present on the surfaces of the particles.[6-8] Oxidation of MeB_2 compounds under ambient conditions is nominally stoichiometric, resulting in the formation of equimolar amounts of MeO_2 and B_2O_3. At elevated temperatures, B_2O_3 evaporates, leaving a porous MeO_2 scale that does not act as a barrier to further oxidation.[9] Additives, such as B_4C, $MoSi_2$, and C, have been shown to react with oxygen impurities present on the surfaces of the starting powder particles at elevated temperatures.[10,11] Removing these impurities from the particle surfaces is beneficial to the densification process and leads to increased densification rates, decreased grain coarsening, and improved oxidation resistance.[12-14] Specifically, Zhu showed that carbon added to remove oxygen impurities decreased both the temperature and sintering hold time required to achieve near fully dense ZrB_2 by pressureless sintering, which decreased the effects of grain coarsening.[7] Three reactions can be used to describe possible processes that occur when carbon is added (Reactions 1-3). Reaction 1 describes the carbothermal reduction of both oxidation products (ZrO_2 and B_2O_3 for ZrB_2). However, at elevated temperature, B_2O_3 can evaporate by Reaction 2. When this happens, carbon can react directly with ZrO_2 to form ZrC by Reaction 3. The relatively small amounts of ZrC resulting from Reaction 3 likely goes into solid solution with the ZrB_2.[15]

$$ZrO_2 + B_2O_3 + 5C \rightarrow ZrB_2 + 5CO_{(g)} \tag{1}$$

$$B_2O_3 \rightarrow B_2O_{3(g)} \tag{2}$$

$$ZrO_2 + 3C \rightarrow ZrC + 2CO_{(g)} \tag{3}$$

Due to strong covalent bonding, and low diffusion rates that inhibit the material transport required for densification, hot pressing has typically been used to densify ZrB_2.[2] In general, pressure applied during heating allows for faster densification and finer grain sizes.[16] Specifically for MeB_2 ceramics, HfB_2 has been shown to reach full density at temperatures as low as 1800°C by hot pressing, which is a few hundred degrees lower than required for partial densification by pressureless sintering.[17] However, pressureless sintering is attractive because it offers the potential for near net shape forming of complex shapes.[18] Initially, full densification of ZrB_2 by pressureless sintering was reported to occur at 2150°C.[18] With additives like carbon, boron carbide, or molybdenum disilicide that react with and remove oxygen impurities at lower temperatures, full density has been achieved by pressureless sintering of ZrB_2 at temperatures as low as 1900°C.[7,10,11] However, densification of ZrB_2 by pressureless sintering requires extended times (i.e., 2 hours or more) at the sintering temperature, which can result in grain coarsening that produces lower strengths than hot pressed ceramics for the same composition.

Spark plasma sintering (also known as field assisted sintering or pulsed electric current sintering) provides rapid densification for different types of materials by combining heating, using a pulsed direct current (DC), with an applied uniaxial load.[19-21] The pulsed current leads to so-called Joule heating of the sample and die at rates as high as about 600°C/min with a unique temperature distribution observed, where temperatures decrease radially from the center of the sample.[22,23] In comparison to hot pressing, grain growth is typically lower during densification by spark plasma sintering due to the rapid heating rates and the application of the external force, which leads to rapid densification.[24] Using spark plasma sintering, ZrB_2-SiC has been shown to reach near full density as low as 1550°C with a resulting grain size of ~2 μm.[25,26] Likewise pure ZrB_2 has been shown to achieve full density by spark plasma sintering at much lower temperatures than hot pressing, reaching full density at temperatures as low as 1800°C, compared to temperatures of 2000°C or above that are typical for hot pressing.[27]

The goal of this study was to investigate the effects of initial oxygen content and particle size on densification of ZrB_2. Pressureless sintering, hot pressing and spark plasma sintering techniques were compared to analyze the effect each had on densification of ZrB_2.

Procedure

Commercially available ZrB_2 (Grade B, H. C. Starck, Germany) was used for this study. The powder was used either as received (AR), which had a particle size of ~2 μm, or after attrition milling (AM), which reduced the particle size to ~0.2 μm. Powders were attrition milled in hexane with Co-bonded WC media for two hours at a spindle speed of 600 rpm. The resulting WC content in the attrition milled ZrB_2 was ~5 wt% based on total batch weight. The solvent was removed by rotary evaporation. Particle sizes were measured by laser light scattering (Microtrac S3500, Montgomeryville, PA).

The initial oxygen content for AR ZrB_2 was 1.0 wt%, but it increased to 2.5 wt% for AM ZrB_2. Before sintering, carbon was added to some formulations to react with and remove oxygen that was present as impurity oxides on the particle surfaces. Carbon additions were determined based on the initial oxygen content of the materials assuming removal of oxygen by Reactions 1-3. For AR ZrB_2, 0.75 wt% carbon was added, with the resulting material designated ARC. For AM ZrB_2, 1.75 wt% carbon was added and the resulting material was designated AMC. Carbon was added in the form of phenolic resin (GP 2074, Georgia Pacific, Atlanta, GA). The resin was dissolved in acetone and then the ZrB_2 powder was added to that solution, with stirring, for complete dispersion. After dispersion, the solvent was extracted by rotary evaporation. The resulting mixture consisted of ZrB_2 powder particles that were uniformly coated with phenolic resin. The resin was converted to carbon by charring at 700°C in flowing argon for 2 hours. The heating and cooling rates for the charring process were 10°C/min. To increase oxygen content in some formulations, AM ZrB_2 powder was heated to 450°C for 10 minutes at a rate of 10°C/min in stagnant air. The resulting powder (AMO) had an oxygen content of

8.2 wt%. Before further processing, all powder formulations were crushed and passed through a 50-mesh sieve to ensure uniformity.

ZrB_2 was densified using pressureless sintering (PS), hot pressing (HP), or spark plasma sintering (SPS). For PS, powder was formed into 2 cm diameter disks by uniaxially pressing at 30 MPa followed by cold isostatic pressing at 300 MPa. Pellets were sintered in a resistance-heated graphite element furnace (Model 3060, Thermal Technologies Inc, Santa Rosa, CA) at temperatures ranging from 1600°C to 2100°C. The furnace was heated at 10°C/min under mild vacuum (nominally less than 27 Pa or ~200 mTorr) to reaction holds at 1250°C and 1450°C, where the temperature was held for one hour at each temperature to allow the vacuum to return to the nominal level. Previous studies have indicated that these holds promote oxide removal by evaporation of B_2O_3 and reaction between ZrO_2 and carbon.[6,11,28] Above 1450°C, the ramp rate was increased to 20°C/min to the sintering temperature and the atmosphere was switched to flowing argon gas (nominally $\sim10^5$ Pa or 1 atm). Similarly for HP, the furnace was heated at 10°C/min in mild vacuum (same conditions as in PS) to reaction holds at 1250°C and 1450°C. Above 1450°C, the ramp rate was increased to 35°C/min and the atmosphere was switched to flowing argon gas (nominally $\sim10^5$ Pa or 1 atm). A uniaxial load of 32 MPa was applied at 1600°C as specimens were heated to the final densification temperature of 1900°C. Specimens were held at the densification temperature until ram travel ceased (typically ~ 30 min). Specimens were cooled at 35°C/min and the applied load was released after the temperature fell below 1600°C. For SPS, the powders were reacted prior to loading into the die by heating in the sintering furnace at a rate of 10°C/min to 1250°C for one hour under vacuum (nominally 27 Pa) with an additional hold at 1500°C for one hour. Reacted powders were densified by SPS (HP D25, FCT Systeme GmbH, Germany) in a graphite die under vacuum (20 Pa) for sintering temperatures ranging from 1600°C to 2000°C. During SPS an external load of 32 MPa was applied at 500°C. The heating and cooling rates were 100°C/min with hold times ranging from 3 to 15 minutes at the sintering temperature. Hold times were determined by the time required for densification to reach completion as judged by ram travel. The temperature in SPS was measured by a pyrometer through a hole in the top punch of the die. After densification, materials were designated by a combination of letters to indicate the starting powder type (AR, AM, AMC, or AMO) and densification method (PS, HP, or SPS) such that PS AMC indicates attrition milled powder with carbon added that was densified by pressureless sintering. For each densification technique, the outer portion of the material was removed so that central part of the specimen was analyzed to minimize any effects that were due to contact with the dies or furnace atmosphere.

The oxygen contents of the starting powders and densified materials (ground and passed through a 45-mesh sieve) were measured by the LECO® furnace method (Model TC500, St. Joseph, MI)[1]. The bulk densities of sintered ZrB_2 were measured by the Archimedes' technique (ASTM C373-88) using vacuum infiltration and water as the immersing medium. Relative density values were calculated based on nominal batch composition prior to densification. Specimens for mechanical testing and microstructure analysis were prepared by diamond polishing to a 0.25 μm finish. Mechanical strength was measured in four-point flexure according to ASTM C1161 using a semi-articulated fixture and a screw driven load frame (Model 5881, Instron Corp., Norwood, MA) using

---

[1] Analysis was completed by NSL Analytical Services, Inc, Cleveland, OH

type A-bars (1.5 mm x 2 mm x 25 mm). The reported averages and standard deviations were calculated from a minimum of 10 bars. The elastic modulus for each sample was calculated from bar deflection data collected using a deflectometer during four-point flexure. Microstructures were analyzed using scanning electron microscopy (SEM, S-570, Hitachi, Tokyo, Japan) of both fracture surfaces and polished sections. Polished sections were thermally etched at 1515°C for 20 minutes to reveal grain boundaries. Further analysis of SEM images to determine percent porosity and grain size was completed using computer-based image analysis software (ImageJ, National Institutes of Health, West Bethesda, MD). Reported values for grain size are averages of minimum and maximum diameter dimensions for at least 400 grains.

Results and Discussion

Densification Methods

Zirconium diboride can be densified by a variety of methods including PS, HP, and SPS. For example, Figure 1 shows relative density as a function of temperature for pressurelessly sintered ZrB_2. The onset of densification in ZrB_2 was at ~1700°C under flowing argon, indicated by an increase in relative density for PS ARC and PS AMC. After pressureless sintering at 1800°C for 2 hours, the density of PS AMC was 91.2% and increased to a maximum of 97.6% after sintering for 2 hours at 2000°C. For comparison to other processes that are described below, the grain size of PS AMC was 8.9 μm after sintering at 1900°C for 2 hours. Above 2000°C the relative density of PS AMC ceramics decreased, likely due to an increased driving force for grain growth during heating to the final PS temperature as indicated by the formation of entrapped porosity within grains (not shown). A grain size of 31 μm was observed after sintering PS AMC at 2100°C for 2 hours (relative density ~93%), compared to a grain size of 10.6 um after sintering at 2000°C for 2 hours (relative density ~97.6%). Without the addition of carbon, limited densification occurred. For example, PS AM had a relative density of 67.4% after sintering at 2000°C and a maximum of 75.0% after sintering at 2100°C. From these observations, it is evident that removal of oxygen, which was accomplished by adding carbon in this study, is required to achieve high relative density by PS.

The application of external pressure during HP enhanced densification, which decreased the time required for densification and increased the density achieved at any temperature compared to PS. Figure 2 shows the relative density as a function of time during HP of ZrB_2. For HP, a uniaxial load of 32 MPa was applied when the specimen temperature reached 1600°C. At that temperature, data collection started by recording the ram travel. The onset of densification during HP was observed at ~1700°C, similar to that of PS. Based on ram travel, HP resulted in a densification rate of 0.975 min^{-1} at ~1900°C for AMC, which was presumably faster than the densification rate during PS due to the applied pressure, which should aid densification. Specifically, a relative density of >99% was achieved for HP AMC after 50 minutes at 1900°C, compared to a relative density of 97% for PS AMC after 120 minutes at 1900°C. Further microstructural analysis revealed an average grain size of 3.3 μm for HP AMC after HP for 50 min at 1900°C, compared to a grain size of 8.9 μm for PS AMC after PS for 2 hours at 1900°C. Not only did HP enhance densification, but it also decreased grain growth compared to PS due to an increased densification rate that resulted from the application of the external pressure.

The third densification technique that was examined in this study was SPS. The densification behavior by SPS is shown in Figure 3. During SPS, the onset of densification occurred at ~1500°C. Unlike HP, in which the pressure was applied only after the specimen reached 1600°C, pressure was applied at temperatures above 500°C during the SPS cycle. In addition to the reduction in the onset temperature for densification, the densification rate during SPS was higher than HP, reaching 1.744 min^{-1} at ~1900°C for AMC compared to 0.975 min^{-1} during HP at 1900°C. The relative density of SPS AMC reached 89% after 5 min at 1900°C. Lower density of SPS AMC was a result of a defined hold time of 5 minutes at 1900°C. Because density was still increasing at the end of the hold time, an extended hold time would have increased density. However, a maximum density of >99% was achieved for SPS AMC at 2000°C for 5 min. Because densification was interrupted after five minutes at 1900°C, even less grain growth occurred during SPS than had during HP. For SPS AMC densified at 1900°C, the average grain size was 1.6 μm, about half the size of the same powder densified by HP at 1900°C. The enhanced densification rate for SPS compared to HP and PS has been attributed to a combination of the increased heating rate (100°C/min) and the surface chemical effects induced by the pulsed electric current applied to heat the specimen for SPS.[21,27] Because the densification rate was much higher in SPS than in HP and PS, near full density could be achieved using lower temperatures and shorter times at sintering temperature than other methods, which led to smaller final grain sizes.

For the three sintering techniques, the sintering time required to achieve near full density indicated that the driving force for densification increased going from PS to HP to SPS. The increase in driving force was evident by comparing the densification rates for

HP (0.975 min^{-1}) and SPS (1.744 min^{-1}) at 1900°C. As a result of the increasing densification rate, the time required to reach full density at the sintering temperature decreased, which had the beneficial effect of decreasing grain size from 8.9 μm for PS to 3.3 μm for HP and to 1.6 μm for SPS, which is shown in Figure 4. Based on the initial observations of densification described in this section, six different combinations of sintering technique, starting particle size, and oxygen content were selected for a more comprehensive examination of the effects of the processing parameters. Each combination was selected to produce nearly full theoretical density for a specific sintering technique and/or type of starting powder. The sintering temperatures for these materials were: 2050°C for PS, 1900°C for HP, and 2000°C for SPS. The combinations were designed to separate the effects of sintering technique, oxygen content of the starting powders, and particle size on densification.

Oxygen Content

Previous studies have shown that oxygen impurities enhance particle coarsening during heating, which impedes densification.[6] Therefore, the oxygen content of the starting ZrB_2 powder also impacts the microstructure and mechanical properties of the densified ceramics. From the preliminary densification study described above, specific combinations of starting particle size and carbon additions were selected for densification by PS, HP, or SPS to analyze the effect of oxygen content on mechanical properties and microstructure.

The densification behavior for PS of ZrB_2 powders with a range of oxygen contents is shown in Figure 5. All of the starting powders were attrition milled and had the same starting particle size of ~0.2 μm. After attrition milling, the nominal oxygen content for the powder, designated AM, was 2.1 wt% prior to densification. The powder with the highest nominal oxygen content, AMO, had an initial oxygen content of 8.2 wt%. Both AM and AMO showed the same densification trends in PS. However, the relative density of AMO was ~20% lower than that of AM for any sintering temperature because of grain coarsening, which led to the formation of closed pores entrapped within grains in addition to open porosity. At lower temperatures, PS AMO was less dense than other materials, probably due to the presence of an oxide scale on the outside of the particles and agglomeration due to the oxidation procedure that was employed.

Previous research has shown that carbon reacts with and removes surface oxide impurities from ZrB_2, leading to higher relative densities and smaller grain sizes than ceramics prepared without carbon additions.[7] The addition of carbon also reduces the onset temperature for densification to 1700°C (PS AMC) compared to 2000°C or higher for PS AM and PS AMO. From this observation, oxygen impurities had an adverse effect on densification of ZrB_2. For TiB_2, Baik and Becher concluded that a total oxygen content of less than 0.5 wt% was necessary to achieve high relative density.[6] In the present study, carbon was added to some batches to react with and remove oxygen to promote densification.

Similar to PS, the initial oxygen content of the powders affected the relative density for ZrB_2 densified by HP; however, smaller grain sizes were observed for HP materials compared to those densified by PS, shown in Table I. For HP, the initial oxygen contents of the powders varied from 2.1 wt% for AM and AMC to 8.2 wt% for AMO. The mechanical force applied during HP enhanced densification and reduced the time required to reach full density, which limited the amount of time over which grain growth was possible. After HP at 1900°C for 30 minutes, the grain size of HP AM was 3.1 μm and the relative density was ~99%. The grain size was 3.4 μm for HP AMO and the relative density was 97% for similar conditions (not shown). For comparison, the grain size of PS AMC was 8.9 μm after 120 min at 1900°C and PS AMO did not densify significantly. The application of pressure as a driving force increased the density of ZrB_2 when oxygen impurities were present. In addition, HP decreased the time required at the sintering temperature, which decreased grain coarsening.

Similar to HP, the initial oxygen content of the powders did inhibit densification by SPS. However, grain size and densification behavior were affected by the initial oxygen content. After SPS at 2000°C, the grain size of SPS AMC was 4 μm compared to 7.3 μm for SPS AMO (Table I). Also, the standard deviation of grain size for SPS AMC was 1.6 μm compared to a standard deviation of 2.1 μm for SPS AMO, which shows that removing oxygen reduced the range of grain sizes in the final ceramics. Figure 6 shows that the standard deviation in the grain size was likely caused by a few larger grains that grew at the expense of a majority of smaller grains. These grains were larger than grains in other SPS ZrB_2 samples, presumably due to the higher initial oxygen content of the powders. Based on these results, oxygen content had a considerable effect on the grain size of SPS ZrB_2. Also of note is that SPS ZrB_2 samples had the smallest grain size among the different densification methods for each composition-sintering temperature combination. For example, at 1900°C SPS AMC had a grain size of 1.6 μm compare to 3.3 μm for HP AMC and 8.9 μm for PS AMC. One significant difference between SPS and the other densification techniques is that SPS had a faster heating rate, 100°C/min or higher, compared to programmed heating rates of 35°C/min for HP and 10°C/min for PS. In addition, SPS employed direct heating of the ZrB_2 with the pulsed electric current, which may have also reduced grain coarsening by promoting removal of oxide impurities at lower temperatures. This combination of direct heating and higher heating rates allowed for high density ZrB_2 with a range of oxygen content to be achieved. However, the presence of oxygen decreased the grain size uniformity.

The final oxygen content of densified ceramics was also affected by the densification technique. The initial and final oxygen contents of ZrB_2 specimens are shown in Table I. AMC ZrB_2 had an initial oxygen content of 2.1 wt%, which decreased to 0.03 wt% after PS, HP, or SPS (Table I). For comparison, the final oxygen content of AM ZrB_2 was 0.4 wt% after HP, which is an order of magnitude higher than AMC ZrB_2. HP AM ZrB_2, however, achieved near full density showing that applied pressure improves densification compared to PS, despite the presence of oxygen impurities.

In contrast to PS and HP, SPS utilizes direct heating of the sample using a pulsed current, which improved oxygen removal during processing. SPS AMO, which had an initial oxygen content of 8.2 wt% or about four times higher than AM ZrB_2, had a final oxygen content of 0.14 wt%, roughly one-third that of HP AM, which had a final oxygen content of 0.4 wt%. Based on these results, SPS shows a greater ability to remove oxygen content than PS or HP. The enhanced ability to remove oxygen is attributed to the effects of the pulsed electric current to achieve high heating rates. Some researchers have proposed to lead to dielectric breakdown of surface oxide impurities.[21] Regardless of the mechanism, the enhanced removal of oxygen would be expected to benefit densification by reducing the effects of grain coarsening during the heating cycle.

Particle Size

Starting particle size also affects densification behavior. To minimize the impact of oxygen content on densification, the effect of starting particle size on densification was examined in materials with carbon additions. It should be noted here that particle size reduction was accomplished by attrition milling with WC media to reduce starting particle size, which introduced ~5 wt% WC impurities to ZrB_2. At elevated temperatures, WC goes into solid solution with ZrB_2 and has been shown to act as a sintering aid at temperatures above 2100°C.[18] The compositions in the present study contained carbon, which acts as a sintering aid at temperatures below 2000°C. Therefore, the effects discussed below should be due to particle size and not the presence of WC impurities in AM compositions.

Figure 7 shows relative density as a function of sintering temperature for ZrB_2 with different starting particle sizes. PS ARC had a starting particle size of 2 μm while PS AMC had a starting particle size of 0.2 μm. For both materials, the onset of densification was around 1700°C. However, PS AMC achieved at relative density ~97% at 1900°C, while PS ARC only reached a relative density of 86% at the same temperature. In general, higher sintering temperatures were required to densify ZrB_2 with the larger particle size. A maximum relative density of 94% was achieved for PS ARC after pressureless sintering at 2100°C for three hours. Consequently, the grain size of dense PS ARC (26 μm after sintering at 2100°C for 120 min) was larger than PS AMC (8.9 μm after sintering at 1900°C for 120 min) because of the longer times and higher temperatures required to achieve similar densities. An average grain size was not calculated for PS ARC because it could not be measured accurately due to its lower densities, so the reported value is representative of the feature sizes observed in SEM. Based on these results, reducing the starting particle size appeared to increase the driving force for densification, which enabled nearly full densification by PS at 1900°C when the oxygen impurity content was controlled using carbon additions.

Similarly, in ZrB_2 densified by HP at 1900°C, relative densities of ARC and AMC were 89% and 99%, respectively. Based on these observations, finer starting particle sizes resulted in higher densities, presumably due to more rapid densification rates that resulted from the higher driving force for densification associated with the finer starting particle size. Figure 2 showed that 20 additional minutes were required at 1900°C for HP ARC to reach full density compared to the 50 minutes needed to densify HP AMC. With longer time at 1900°C, the grain size of HP ARC was 6.6 μm compared to the grain size of HP AMC that was 3.3 μm. Overall, smaller starting particle size led to higher density because of an increased surface area that increased the driving force for densification. As a result of decreased time at the sintering temperature, smaller grain sizes were achieved.

Particle size also affected densification and microstructure of ZrB_2 densified by SPS. As with the other densification techniques, higher temperatures were required for densification of powders with larger starting particles sizes. For SPS ARC with a starting particle size of ~2 μm, a maximum relative density of 85% was achieved by SPS at 2000°C. In contrast, SPS AMC had a starting particle size of ~0.2 μm and a final relative density of >99% at the same temperature. The lower density of SPS ARC was attributed to its larger starting particle size. The final grain size of SPS ARC densified at 2000°C was 7.1 μm compared to 4.1 μm for SPS AMC. Fracture surfaces (Figure 8) show the finer grain and pore sizes in SPS AMC as compared to SPS ARC. While SPS ARC is 85% dense, the fracture surface was transgranular, which was not expected. From Figure 8, SPS ARC shows particles inside pores that are ZrB_2. The hypothesis for this occurrence was that as received powder had a non-uniform particle size that lead to isolated particles, uniformly distributed in the material, that did not participate during densification.

Property – Microstructure Relationships

In general, the strength of ZrB_2 ceramics with high relative density (>95%) had a linear relationship with the inverse square root of grain size (Figure 9). The gray line on the plot is a trend line based on the Griffith relationship assuming that the grain size was the critical flaw in these ceramics. Compared to the other materials prepared as part of the present study, the failure strength of SPS AMC (527 MPa) was higher than predicted by its average grain size (4.1 μm). For comparison, the strength of SPS AMC was higher than that of HP AMC (460 MPa) even though HP AMC had a finer grain size (3.3 μm). The trend line in Figure 9 suggests that strengths approaching 700 MPa would be expected, if the average grain size could be reduced to ~1 μm.

For HP and SPS AMC ZrB_2 specimens, the failure mechanism was a mix of transgranular and intergranular modes (not shown). Compositions with carbon contents lower than the solid solubility limit in ZrB_2 lead to a higher probability for transgranular fracture. However, larger amounts of carbon accumulated as a second phases at grain boundaries lead to a higher propensity for intergranular fracture, shown in Figure 10. Carbon added in amounts above 2 wt%, based on ZrB_2 content, led to observed carbon at grain boundaries, indicated by arrows in Figure 10, which was confirmed by Raman spectroscopy. Other features of SPS AMC ZrB_2 were also finer than the other AMC ceramics. For example, SPS AMC had a smaller volume fraction and size of pores compared to that of SPS ARC, which had an average strength of 445 MPa. SPS ARC also had a higher than predicted strength based on a relative density of 86%. In particular, SPS ARC exhibited a high degree of transgranular fracture and large open pores between grains, which was not expected based on the porosity level being above the percolation threshold. SPS specimens had higher strengths as a result of smaller grains and cleaner grain boundaries that resulted in a higher probability of transgranular fracture.

In contrast to SPS AMC, PS AMC had an average strength of 300 MPa, which was lower than expected based on grain size. The lower failure strength was due to the presence of carbon inclusions in the grain boundaries that caused the failure mode to become intergranular. The fracture mode switches as a result of accumulated carbon at the grain boundaries, which can be observed as a second phase when more than ~2 wt% carbon was added to ZrB_2.

Summary and Conclusions

ZrB_2 ceramics were densified by PS, HP, and SPS at temperatures as low as 1900°C. For each processing condition, starting particle size and initial oxygen content of ZrB_2 were varied to evaluate the effects on density, grain size, and strength. The increased surface area as a result of decreasing starting particle size from ~2 μm (AR) to 0.2 μm (AM) increased the driving force for densification. AR ZrB_2 could not be densified under any of the conditions used in this study. However, PS AMC reached a maximum relative density of 97.6% after PS at 2000°C. The application of uniaxial pressure during HP or SPS enhanced the driving force for densification and led to ~100% relative density for AM ZrB_2. Grain size increased with increasing oxygen content of the starting powders, which showed that the degree of grain coarsening increased with increased oxygen content. For PS, the addition of carbon was required to remove oxygen impurities and facilitate densification. The increased heating rates in HP and SPS also enabled higher densification rates, which resulted in smaller grain sizes due to decreased sintering times and reduced the driving force for grain coarsening. SPS further enhanced the removal of oxygen impurities compared to HP and PS as a result of increased heating rates and, possibly, the effect of the pulsed current on the stability of the surface oxide impurities. Strengths showed a roughly linear trend with inverse square root of grain size as predicted by the Griffith relationship. The highest strength was achieved by SPS, followed by HP, and then PS. The strength of SPS ZrB_2 was higher than expected based on grain size and porosity considerations. Fracture surfaces of HP and SPS ZrB_2 samples showed a predominantly transgranular fracture mode while PS ZrB_2 showed predominantly intergranular fracture, indicating weaker grain boundaries in PS that were due to an observed carbon phase.

The combined results suggest reducing impurity content (including oxygen and carbon content) and starting particle size could produce ZrB_2 ceramics with smaller grain sizes and higher densities. The addition of a small amount of carbon, 1-2 wt% depending on initial oxygen content, removes oxygen impurities without resulting in the presence of excess carbon in the grain boundaries of the final ceramics. Based on this analysis, additives such as B_4C that react with ZrO_2 to produce ZrB_2 rather than ZrC may result in higher strengths for the final ceramics by reducing the content of residual carbon. SPS is also beneficial, as additives are not necessary to reduce oxygen content, which may further enhance the purity of the grain boundaries in the final ceramic. Also, increasing the heating rate to 200-300°C/min while sintering at 2000°C limits grain growth by decreasing the effects of grain coarsening and maintain >99% density. If these processing variables are controlled simultaneously, the grain size of ZrB_2 could be minimized without introducing unwanted impurities in the final ceramic (i.e., carbon inclusions) and changing the fracture behavior. Based on predictions using the Griffith criterion, if grain size can be reduced to ~1 μm, then strengths as high as 700 MPa may be possible.

Acknowledgements

The authors would like to acknowledge Dr. Michael Cinibulk and Dr. Carmen Carney at the Air Force Research Laboratory, WPAFB in Dayton, OH for their aid in the use of the FCT SPS unit, which was crucial for the completion of this work. The AMCL at Missouri S&T should also be acknowledged for use of SEMs.

References

1. R.A. Cutler, "Engineering Properties of Borides," pp. 787-803 in Vol. 4, *Ceramics and Glasses: Engineered Materials Handbook.* Edited by S. J. S. Jr. ASM International, Materials Park, OH, 1991.

2. L.S.S. R. Telle, and K. Takagi, "Boride-Based Hard Materials," pp. 802-945 in *Handbook of Ceramic Hard Materials.* Edited by R. Riedel. Wiley-VCH, Weinheim, Germany, 2000.

3. William G. Fahrenholtz, Gregory E. Hilmas, Inna G. Talmy, and James A. Zaykoski, "Refractory Diborides of Zirconium and Hafnium," *Journal of the American Ceramic Society,* **90** [5] 1347-64 (2007).

4. X. Zhang, X. Luo, J. Han, J. Li, and W. Han, "Electronic structure, elasticity and hardness of diborides of zirconium and hafnium: First principles calculations," *Computational Materials Science,* **44** [2] 411-21 (2008).

5. M.M. Opeka, I.G. Talmy, and J.A. Zaykoski, "Oxidation-based materials selection for 2000C + hypersonic aerosurfaces: Theoretical considerations and historical experience: Special Section: Ultra-High Temperature Ceramics (Guest Editors: Joan Fuller and Michael D. Sacks)," *Journal of Materials Science,* **39** 5887-904 (2004).

6. S. Baik and P.F. Becher, "Effect of Oxygen Contamination on Densification of TiB2," *Journal of the American Ceramic Society,* **70** [8] 527-30 (1987).

7. S. Zhu, W.G. Fahrenholtz, G.E. Hilmas, and S.C. Zhang, "Pressureless sintering of carbon-coated zirconium diboride powders," *Materials Science and Engineering: A,* **459** [1-2] 167-71 (2007).

8. M.S. Jensen, M.-A. Einarsrud, and T. Grande, "Preferential Grain Orientation in Hot Pressed TiB2," *Journal of the American Ceramic Society,* **90** [4] 1339-41 (2007).

9. T.A. Parthasarathy, R.A. Rapp, M. Opeka, and R.J. Kerans, "Effects of Phase Change and Oxygen Permeability in Oxide Scales on Oxidation Kinetics of ZrB2 and HfB2," *Journal of the American Ceramic Society,* **92** 1079-86 (2009).

10. L. Silvestroni and D. Sciti, "Effects of MoSi2 additions on the properties of Hf- and Zr-B2 composites produced by pressureless sintering," *Scripta Materialia,* **57** [2] 165-8 (2007).

11. W. G. Fahrenholtz, G. E. Hilmas, S. C. Zhang, and S. Zhu, "Pressureless Sintering of Zirconium Diboride: Particle Size and Additive Effects," *Journal of the American Ceramic Society,* **91** [5] 1398-404 (2008).

12. T.A. Parthasarathy, R.A. Rapp, M. Opeka, and R.J. Kerans, "A model for the oxidation of ZrB2, HfB2 and TiB2," *Acta Materialia,* **55** [17] 5999-6010 (2007).

13. S. C. Zhang, G. E. Hilmas, and W. G. Fahrenholtz, "Pressureless Densification of Zirconium Diboride with Boron Carbide Additions," *Journal of the American Ceramic Society,* **89** [5] 1544-50 (2006).

14. D.A. Ray, S. Kaur, R.A. Cutler, and D.K. Shetty, "Effect of Additives on the Activation Energy for Sintering of Silicon Carbide," *Journal of the American Ceramic Society,* **91** [4] 1135-40 (2008).

15. ACerS-NIST, Phase Equilibria Diagrams, [Computer Program] ACerS-NIST Phase Equilibria for Ceramics Program, 2004.

16. M.N. Rahaman, *Ceramic Processing and Sintering,* 2 ed. CRC Press, Boca Raton, FL, 2003.

17. D. Kalish and E. V. Clougherty, "Densification Mechanisms in High-pressure Hot-Pressing of HfB2," *Journal of the American Ceramic Society,* **52** [1] 26-30 (1969).

18. A.L. Chamberlain, W.G. Fahrenholtz, and G.E. Hilmas, "Pressureless Sintering of Zirconium Diboride," *Journal of the American Ceramic Society,* **89** [2] 450-6 (2006).

19. R.S. Dobedoe, G.D. West, and M.H. Lewis, "Spark plasma sintering of ceramics: understanding temperature distribution enables more realistic comparison with conventional processing," *Advances in Applied Ceramics,* **104** 110-6 (2005).

20. T. Venkateswaran, B. Basu, G.B. Raju, and D.-Y. Kim, "Densification and properties of transition metal borides-based cermets via spark plasma sintering," *Journal of the European Ceramic Society,* **26** [13] 2431-40 (2006).

21. Z. Munir, U. Anselmi-Tamburini, and M. Ohyanagi, "The effect of electric field and pressure on the synthesis and consolidation of materials: A review of the spark plasma sintering method," *Journal of Materials Science,* **41** [3] 763-77 (2006).

22. Eugene A. Olevsky, Veena Tikare, and Terry Garino, "Multi-Scale Study of Sintering: A Review," *Journal of the American Ceramic Society,* **89** [6] 1914-22 (2006).

23. D. Tiwari, B. Basu, and K. Biswas, "Simulation of thermal and electric field evolution during spark plasma sintering," *Ceramics International,* **35** [2] 699-708 (2009).

24. E.A. Olevsky, S. Kandukuri, and L. Froyen, "Consolidation enhancement in spark-plasma sintering: Impact of high heating rates," *Journal of Applied Physics,* **102** [11] 114913-12 (2007).

25. I. Akin, M. Hotta, F.C. Sahin, O. Yucel, G. Goller, and T. Goto, "Microstructure and densification of ZrB2-SiC composites prepared by spark plasma sintering," *Journal of the European Ceramic Society,* **29** [11] 2379-85 (2009).

26. H. Wang, C. Wang, X. Yao, and D. Fang, "Processing and Mechanical Properties of Zirconium Diboride-Based Ceramics Prepared by Spark Plasma Sintering," *Journal of the American Ceramic Society,* **90** [7] 1992-7 (2007).

27. S.-Q. Guo, T. Nishimura, Y. Kagawa, and J.-M. Yang, "Spark Plasma Sintering of Zirconium Diborides," *Journal of the American Ceramic Society,* **91** [9] 2848-55 (2008).

28. S.C. Zhang, G.E. Hilmas, and W.G. Fahrenholtz, "Pressureless Densification of Zirconium Diboride with Boron Carbide Additions," *Journal of the American Ceramic Society,* **89** [5] 1544-50 (2006).

Table I Density, Grain Size, Hardness, Strength, and Elastic Modulus of ZrB_2 Ceramics

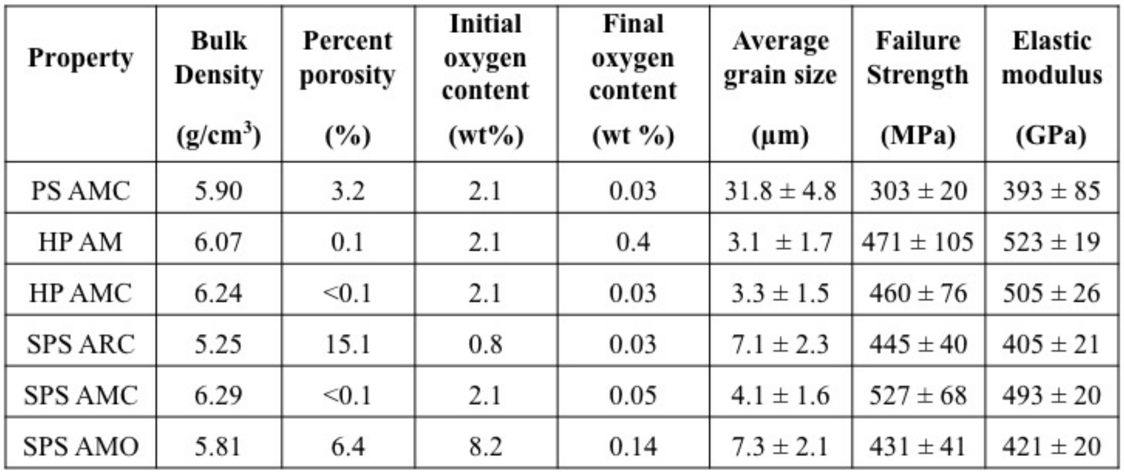

Property	Bulk Density (g/cm^3)	Percent porosity (%)	Initial oxygen content (wt%)	Final oxygen content (wt %)	Average grain size (μm)	Failure Strength (MPa)	Elastic modulus (GPa)
PS AMC	5.90	3.2	2.1	0.03	31.8 ± 4.8	303 ± 20	393 ± 85
HP AM	6.07	0.1	2.1	0.4	3.1 ± 1.7	471 ± 105	523 ± 19
HP AMC	6.24	<0.1	2.1	0.03	3.3 ± 1.5	460 ± 76	505 ± 26
SPS ARC	5.25	15.1	0.8	0.03	7.1 ± 2.3	445 ± 40	405 ± 21
SPS AMC	6.29	<0.1	2.1	0.05	4.1 ± 1.6	527 ± 68	493 ± 20
SPS AMO	5.81	6.4	8.2	0.14	7.3 ± 2.1	431 ± 41	421 ± 20

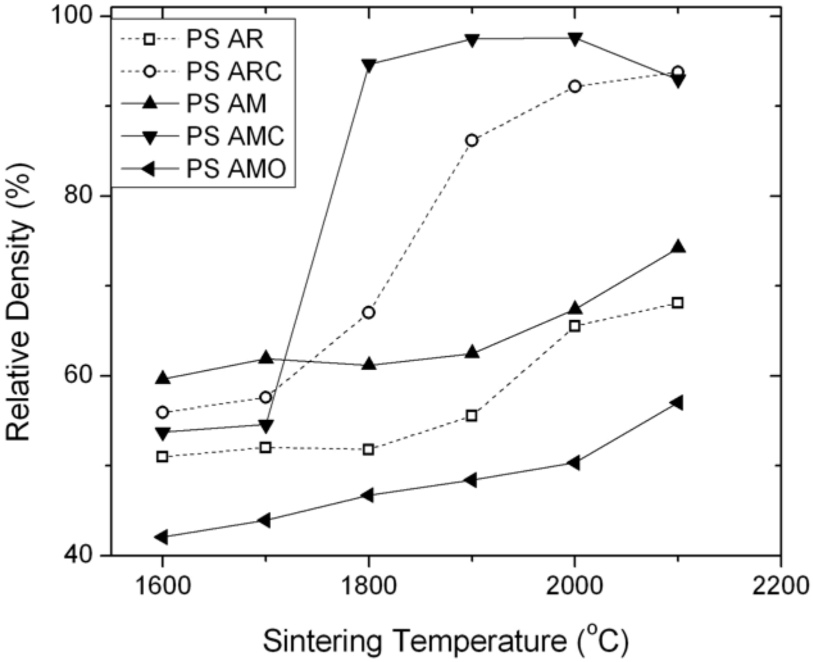

Figure 1: Relative density of various ZrB_2 materials after pressureless sintering for 2 hours at temperatures from 1600°C to 2100°C. The lines are present to guide the eye for each composition.

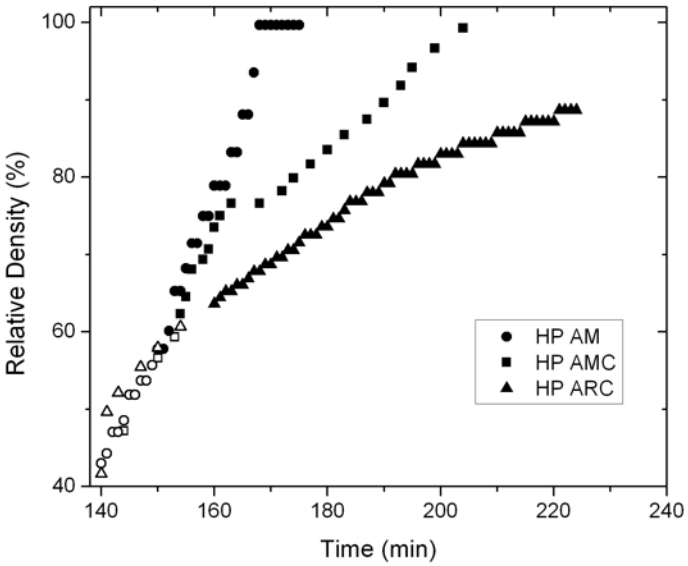

Figure 2: Relative density as a function of time for hot pressing of several ZrB_2 powders. The open symbols indicate times at which the temperature was increasing and the closed symbols indicate times after the final densification temperature of 1900°C was reached.

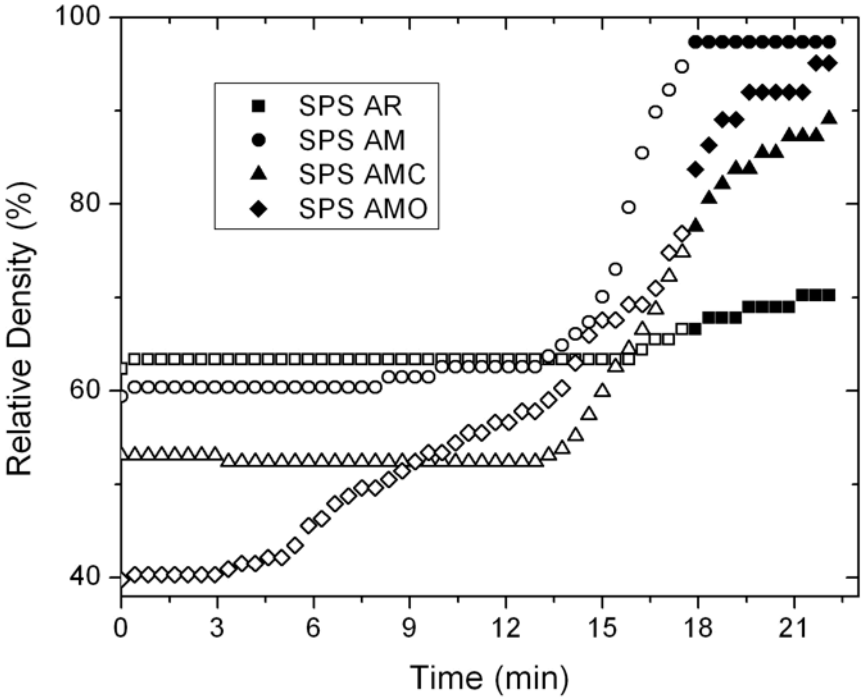

Figure 3 Relative density as a function of time of attrition milled ZrB_2 during spark plasma sintering to a final temperature of 1900°C. The open symbols indicate times at which the temperature was increasing and the closed symbols indicate times after the final densification temperature of 1900°C was reached.

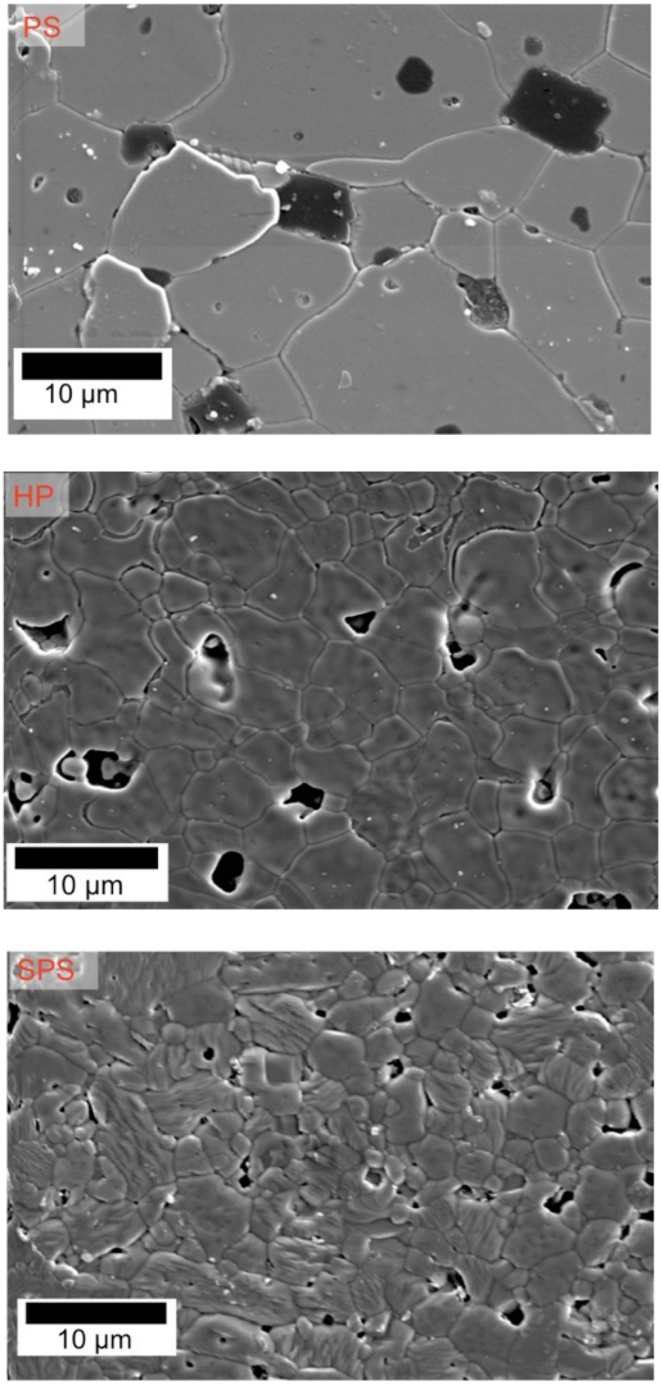

Figure 4: SEM images of AMC ZrB_2 ceramics densified by PS, HP, and SPS at 1900°C.

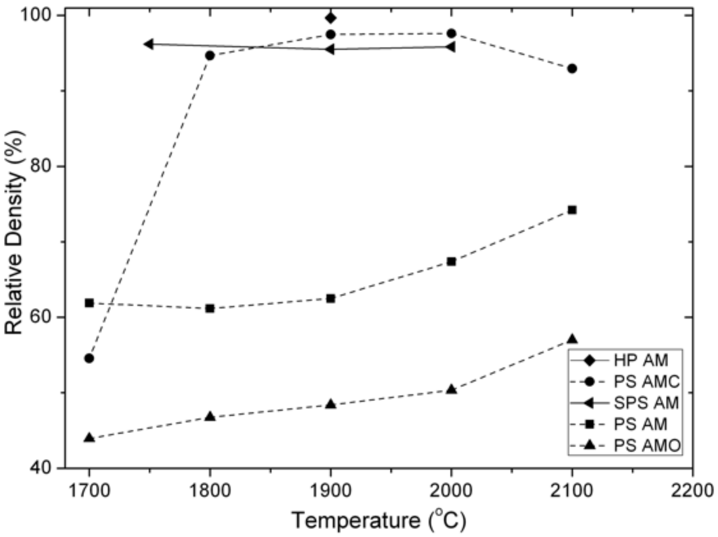

Figure 5: Relative density of ZrB_2 based on nominal composition as a function of sintering temperature for a range of initial oxygen contents and densification techniques.

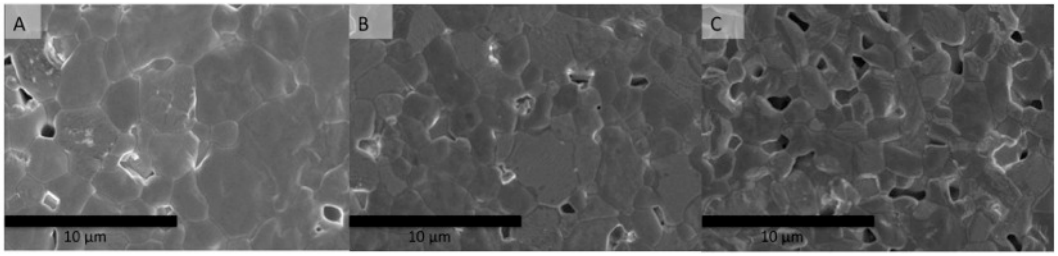

Figure 6: SEM images of ZrB_2 ceramics densified by SPS at of 1900°C, where the starting powders (A) AMO, (B) AM, and (C) AMC had a range of initial oxygen contents.

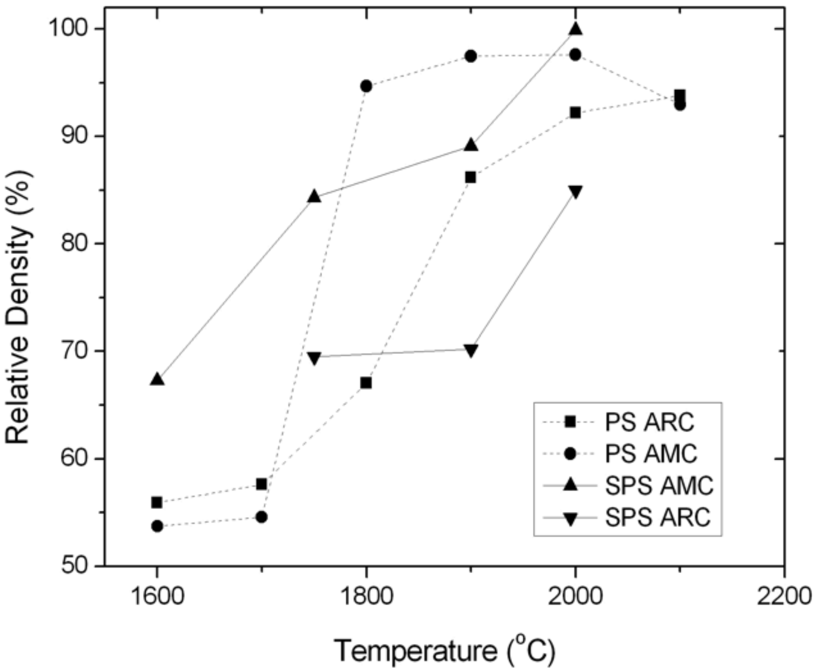

Figure 7: Relative density as a function of densification temperature for ZrB_2 with different starting particle sizes.

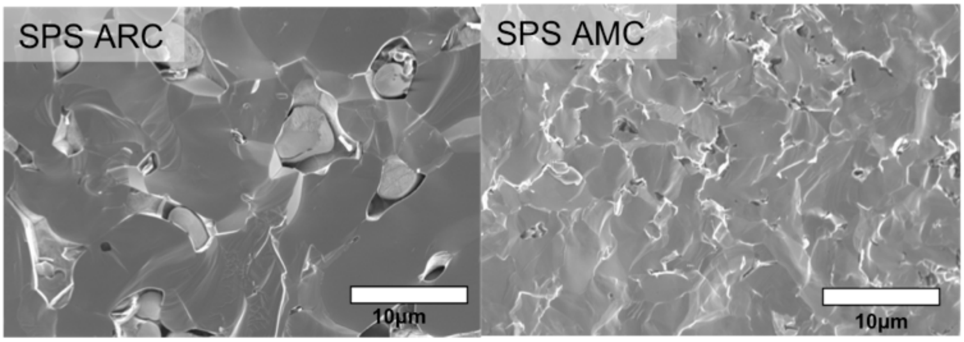

Figure 8: SEM images of fracture surfaces of SPS ARC (left) and SPS AMC (right) that were densified at 2000°C.

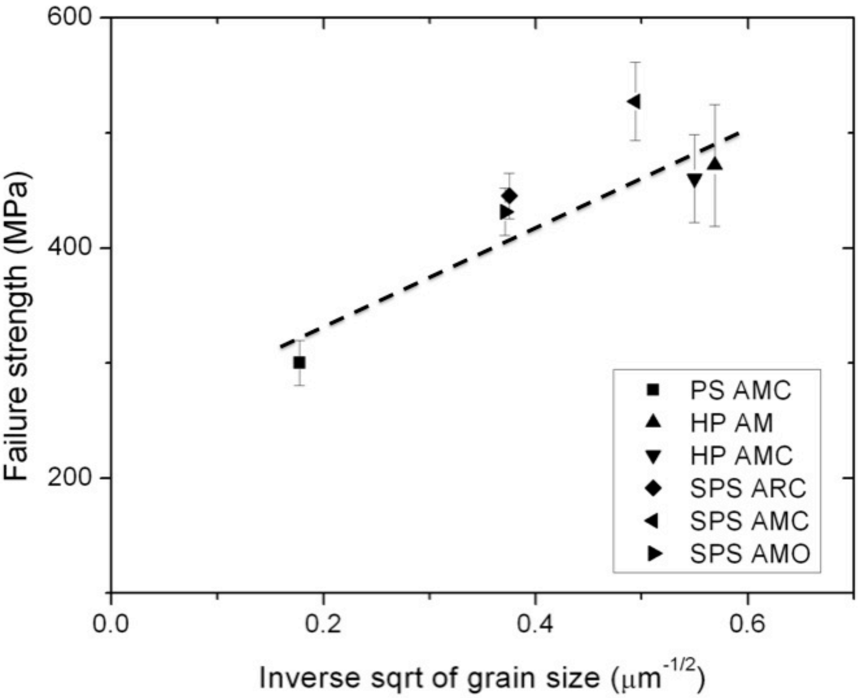

Figure 9: Failure strength as a function of inverse square root of grain size for ZrB_2 ceramics densified by PS, HP, and SPS.

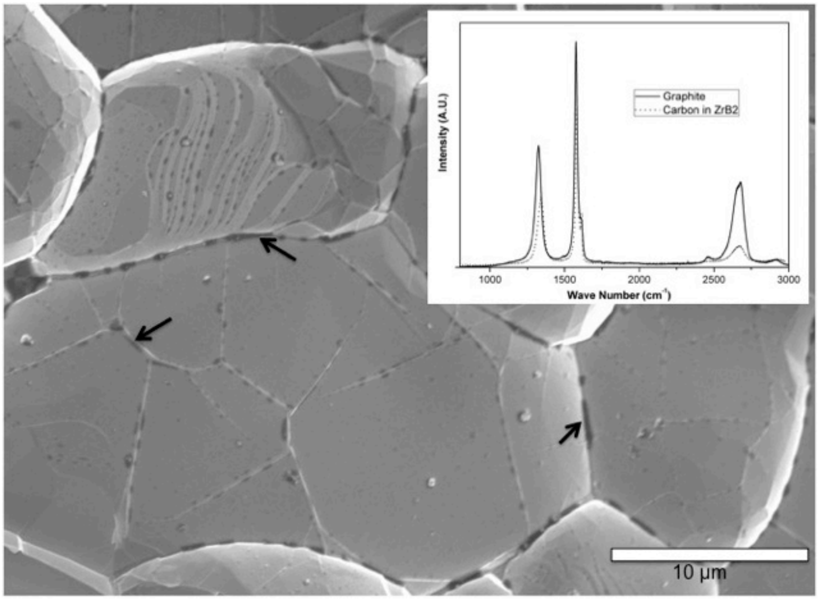

Figure 10: SEM image of a PS AMC ZrB_2 fracture surface. Black areas, indicated by arrows, are confirmed by Raman spectroscopy (shown as an inset) to be graphitic carbon.

2. ELEVATED TEMPERATURE THERMAL PROPERTIES OF ZRB_2 WITH CARBON ADDITIONS

Matthew J. Thompson*; William G. Fahrenholtz; Greg E. Hilmas;
Dept. of Materials Science and Engineering
Missouri University of Science and Technology, Rolla, MO 65409

Abstract

The thermal properties of zirconium diboride (ZrB_2) ceramics with carbon additions of up to 3 wt% were characterized up to 2000°C. Carbon contents were selected to produce ZrB_2 that was nominally pure, contained dissolved carbon, or contained carbon inclusions. The microstructure and density changes that resulted from the carbon additions affected the thermal behavior of ZrB_2 at room and elevated temperatures. Thermal diffusivity at 200°C increased from 0.150 cm^2/sec for nominally pure ZrB_2 to 0.175 cm^2/sec for ZrB_2 with 3 wt% carbon. The thermal diffusivity decreased with increasing temperature, reaching a value of 0.143 cm^2/sec at 2000°C for ZrB_2 with 3 wt% carbon. In addition, thermal diffusivity changed irreversibly during the first thermal cycle after densification due to changes in the microstructure that started between 1550°C and 1650°C. Heating resulted in the formation of a new phase, growth of ZrB_2 grains, changes in the morphology of carbon inclusions, and migration of W impurities from the ZrB_2 matrix into the new phase. Heat capacity, unlike thermal diffusivity, did not change during thermal cycling. Thermal conductivity, which was calculated from thermal diffusivity, heat capacity, and density, was as high as 64.2

W/m•K at 2000°C for ZrB_2 with 3 wt% carbon. The phonon contribution to thermal conductivity decreased to nearly zero with the addition of 3 wt% carbon due to the presence of elongated carbon inclusions around ZrB_2 grains.

Introduction

Zirconium diboride (ZrB_2) based ceramics boast an unusual combination of properties including high hardness (20 GPa)[1], high elastic modulus (546 GPa)[2], high melting temperature (3250°C), and chemical stability.[3,4] In particular, the high melting temperature and chemical stability in extreme temperatures and environments put ZrB_2 into a class of materials known as ultrahigh temperature ceramics (UHTCs). ZrB_2 and the other UHTCs have been proposed for a variety of applications such as cutting tools, refractory linings, or molten metal crucibles.[5] Additionally, diboride based ceramics have high thermal and electrical conductivities (typically >50 W/mK and ~10^7 S/m respectively).[4] High conductivities, in combination with superior mechanical properties, make ZrB_2 an excellent candidate for applications such as high temperature electrodes and thermal protection systems for hypersonic aerospace vehicles.[6]

Due to strong covalent bonding and low self-diffusion coefficients, densification of ZrB_2 requires high temperatures (>1800°C) and external pressures (>20 MPa).[7] Previous research has also shown that the presence of oxides on particle surfaces hinders densification.[8,9] Additives such as carbon, B_4C, and $MoSi_2$ have been used to react with and remove oxides, which promotes densification.[10-12] Specifically, Baik et al. have shown that oxygen content must be below 0.5 wt% to densify TiB_2 by pressureless sintering.[9] Some additives that promote densification have also been shown to reduce grain coarsening at elevated temperatures.[13] Oxidation of ZrB_2 leads to the formation of ZrO_2 and B_2O_3.[8,9,14] Additives such as SiC or $TaSi_2$ have been used to improve the oxidation resistance of ZrB_2, and can also improve densification behavior.[15-17] Si containing compounds promote the formation of a glassy SiO_2 layer on exposed surfaces, which reduces oxidation and maintains mechanical stability above 1000°C.[18] Finally, additions of SiC have also been found to increase the flexure strength of diborides to >1 GPa.[15]

Despite numerous investigations, only minute changes in heat capacity have been reported as a result of additions of less than 5 mol%, of SiC, $TaSi_2$, B_4C, or other common additives.[19] Above the reported Debye temperature of 962°C, heat capacity values >700 J/kg•K have been reported for ZrB_2 with various additives. Measured heat capacities of ZrB_2 ceramics with additives follow values predicted using volumetric rules of mixture calculations with tabulated data such as those found in the NIST-JANAF tables.[20]

Diborides have been proposed for use as sharp leading edges based, in part, on their ability to conduct heat away from the hottest areas of the ceramics.[6] Diborides are desirable because they have higher thermal conductivities than their corresponding carbides or oxides. As an example, ZrB_2 has a reported thermal conductivity >60 W/m•K, whereas reported thermal conductivities for the corresponding carbide, ZrC, are in the range of 30-40 W/m•K.[21-23]

The thermal conductivity of solids consists of contributions due to electron and phonon conduction. The phonon contribution is affected by the phonon mean free path, which is sensitive to the microstructure and, therefore, the processing conditions. The phonon contribution to thermal conductivity of ZrB_2, regardless of processing conditions, reaches a constant value above the Debye temperature because the phonon velocity and mean free path become constant.[23-25] Additives can affect both components of the thermal conductivity. Additions of SiC, for instance, have been shown to increase the thermal conductivity of ZrB_2 to 100 W/m•K due to an increase in the phonon contribution.[23] The thermal conductivity of ceramics with second phase additions has been studied using models such as effective medium theories of Bruggeman[26] and Maxwell[27], or unit cell models used by Smith et al.[28] However, these models have not been able to explain differences in reported experimental values for diborides, mostly because the overall conductivity of these ceramics is made up of a combination of electron and phonon contributions while the models have typically been developed to explain a single transport mechanism.[19]

The purpose of this study was to investigate the effect of carbon addition on the thermal properties of hot pressed ZrB_2.

Procedure

Commercially available ZrB_2 (Grade B, H. C. Starck, Germany) was used for this study. The powder was attrition milled in hexane for two hours using Co-bonded WC milling media in a fluoropolymer lined bucket. The resulting slurry was rotary evaporated to remove hexane. Milling reduced the average particle size of the ZrB_2 from ~2 μm (supplier data) to ~0.2 μm, which was measured by laser light scattering (Microtrac S3500, Montgomeryville, PA). The mass of the WC milling media was measured before and after milling, which indicated that ~2 wt% WC was incorporated into the ZrB_2 powder. The oxygen content after attrition milling was 2.06 wt% as determined using the LECO® furnace method (Model TC500, St. Joseph, MI).[2] Carbon was added as phenolic resin (GP 2074, Georgia Pacific, Atlanta, GA) that was dissolved in acetone. The phenolic resin solution was added to a slurry of ZrB_2 particles in acetone. The resulting mixture was then rotary evaporated to remove the acetone, which left the ZrB_2 particles coated with phenolic resin. The resulting powder was heated at 10°C/min to 700°C and held for 2 hours in flowing Ar to convert the phenolic resin to amorphous carbon. The carbon yield of the phenolic resin was 41 wt%. After charring, the powders were passed through a 50-mesh sieve.

Densification was accomplished by hot pressing using a 1-inch diameter circular graphite die in a resistively heated graphite element hot press (Thermal Technology Inc., Model HP20-3060-20, Santa Rosa, CA). The graphite die was lined with graphite paper and coated with boron nitride (Cerac, SP-108, Milwaukee, WI) to minimize reaction between the die and the ZrB_2. Specimens were heated at 40°C/min throughout the run. Below 1500°C, specimens were heated in a mild vacuum (~20 Pa). Isothermal holds of 1 hour were used at 1300°C and 1500°C during heating to allow for reactions between the surface oxides (B_2O_3 and ZrO_2) and the carbon and/or WC. After the hold at 1500°C, the atmosphere was changed to flowing Ar gas at a pressure of $\sim 10^5$ Pa and a uniaxial pressure of 32 MPa was applied to the specimen. When the specimens reached 1900°C, the furnace was held at that temperature until ram travel had stopped for 10 minutes. The furnace was then allowed to cool at 40°C/min. The external pressure was released below 1650°C.

---

[2] Analysis completed by NSL Analytical Services, Inc, Cleveland, OH

Hot pressed specimens were surface ground and cut (Chevalier, FSG-3A818, Santa Fe Springs, CA) into squares approximately 12.5 mm by 12.5 mm by 3 mm thick. The outer portions of the billets were ground or cut away to remove the portion of the pellet that may have been affected by reaction with the hot press die. The bulk density of each specimen was measured by the Archimedes' technique (ASTM standard C373) using vacuum infiltration with distilled water as the immersing medium. Specimens were polished using successively finer diamond abrasives with a final abrasive size of 0.25 μm. Carbon inclusions that were visible on the polished surfaces were analyzed using Raman spectroscopy (Horiba LabRAM ARAMIS spectrometer, Edison, NJ) with a 633 nm HeNe laser and a 1 μm spot size.

Thermal diffusivity was measured by the laser flash technique (Flashline 5000, Anter Corp, Pittsburgh, PA) following the procedure defined in ASTM standard E1461.[29] Specimens were coated with graphite (Dry Graphite Lube, Diversified Brands, Cleveland, OH) and then analyzed up to 2000°C in flowing Ar that was maintained at a gauge pressure of ~41 kPa. Specimens were heated at 15°C/min. Each data point was an average of 3 tests taken every 2 minutes after the specimen had been held at a constant temperature for 7 minutes, with uncertainty of <2%. Thermal diffusivity was calculated using the Clark and Taylor method according to Equation (1).[30] In this calculation, thermal diffusivity (α) was dependent on specimen thickness (L) and time for the specimen to rise to a quarter, half, and three quarters of the maximum temperature ($t_{0.25}$, $t_{0.5}$, $t_{0.75}$) after the laser pulse. Heat capacity was measured at the same time as thermal diffusivity by comparing the relative temperature rise of each specimen against a graphite standard using Equation (2), where ρ is bulk density, C_p is heat capacity, L is thickness of specimen, and ΔT is temperature rise.[31] The uncertainty of the heat capacity measurement was <3%. Thermal conductivity (λ) was then calculated at each temperature from the measured thermal diffusivity (α), heat capacity (C_p), and bulk density (ρ), according to Equation (3).

$$\alpha = \frac{L^2}{t_{0.5}}\left[-0.346 + 0.362(t_{0.75}/t_{0.25}) - 0.065(t_{0.75}/t_{0.25})^2\right] \tag{1}$$

$$\left(\rho C_p\right)_M = \frac{L_R \Delta T_R}{L_M \Delta T_M}\left(\rho C_p\right)_R \tag{2}$$

$$\lambda = \alpha \rho C_p \tag{3}$$

Electrical resistivity was measured as a function of temperature up to 1200°C in flowing Ar. Measurements were made by the 4-point van der Pauw method (ASTM standard F76) on 12.5 mm round disks that had a thickness of 0.5 mm.[32] Data were collected during cooling after equilibrating for 10 minutes at each test temperature. Nickel electrodes were used for the measurements and they were joined to the specimens with platinum paint. Equation (4) was then used to calculate electrical resistivity based on specimen thickness t, maximum current I, voltages in given directions $V_{ij,kl}$, and a geometric factor *f* that was dependent on the voltages. The reciprocal of electrical resistivity, electrical conductivity, was then used for discussion.

$$\rho = \frac{1.1331 f\, t}{I}\left[V_{21,31} - V_{12,34} + V_{32,41} - V_{23,41}\right] \tag{4}$$

Scanning electron microscopy (SEM; Hitachi S570, Japan) was used to characterize microstructures. Grain sizes were measured from SEM micrographs using image analysis software (ImageJ, National Institutes of Health, Bethesda, MD) by analyzing ~500 grains. Scanning transmission electron microscopy (STEM) sections were produced using focused ion beam milling (Helios Nano Lab 600, FEI, Hillsboro, OR) to a final thickness of 100 nm. STEM (same as FIB) was used to further analyze microstructure for enhanced contrast and higher magnification. X-ray diffraction (Philips X-Pert Pro diffractometer, Westborough, MA, USA) analysis was used to identify phases. Rietveld refinement (RIQAS, Materials Data Inc., Livermore, CA) of XRD patterns was used to quantify the amounts of phases and determine lattice parameters. Diffraction was accomplished using $Cu_{k\alpha}$ radiation (1.5409 Angstroms) and scanning from 5° to 90° 2θ using a step size of 0.0263 degrees.

Results and Discussion

Densification and Microstructure

Zirconium diboride (ZrB_2) was densified with carbon additions up to 3 wt%. As summarized in Table I, adding carbon decreased the time required for densification at 1900°C. The specimen with no intentionally added carbon (designated AM0C to indicate attrition milled powder with 0 wt% carbon addition) required ~35 min at 1900°C to reach nearly full density. In contrast, only ~10 min at 1900°C was required to densify the specimens with 1 wt% (AM1C) and 3 wt% (AM3C) carbon added. Carbon additions also led to a decrease in the final oxygen content of the hot pressed ZrB_2. Oxygen was likely removed by a combination of processes: 1) the evaporation of B_2O_3 by Reaction 5 or similar processes that occurred during heating under mild vacuum (~20 Pa), with evaporation expected to be independent of carbon additions; and 2) the carbothermal reduction of ZrO_2 and B_2O_3 by Reactions 6 and/or 7, which depend on the amount of carbon addition.[13] The final oxygen content in the ceramic with no carbon addition (AM0C) was 0.40 wt% compared to an oxygen content of ~2.06 wt% for the powder prior to hot pressing. Presumably, the reduction in oxygen content from 2.06 wt% to 0.40 wt% was mainly due to Reaction 5. In contrast, the final oxygen contents for the ceramics with carbon additions (AM1C and AM3C) were ≤0.05 wt% due to removal of oxygen by Reactions 6 and 7 in addition to Reaction 5. This behavior showed that carbon additions not only reduced the final oxygen content of the ceramics but also decreased the bulk density because of excess carbon present in the microstructure.

$$B_2O_{3(l)} \rightarrow B_2O_{3(g)} \tag{5}$$

$$ZrO_2 + B_2O_3 + C \rightarrow ZrB_2 + CO_{(g)} \tag{6}$$

$$ZrO_2 + C \rightarrow ZrC + CO_{(g)} \tag{7}$$

Table I: Summary of processing conditions and properties of hot pressed ZrB_2 ceramics.

Designation	**Carbon added (wt%)**	**Final oxygen content (wt%)**	**Time at 1900°C (min)**	**Bulk Density (g/cm^3)**	**Grain size (µm)**	**Observed carbon (vol%)**
AM0C	0	0.40	35.0	6.22	3.3 ± 2.2	0
AM1C	1	0.05	10.0	6.19	2.4 ± 1.3	1.4
AM3C	3	0.03	12.5	6.01	1.8 ± 0.9	10.8

Carbon additions led to a noticeable decrease in grain size in the dense ceramics. Figure 1 shows the microstructure of ZrB_2 ceramics with different carbon additions. For AM0C, no second phases were visible in polished, thermally etched cross sections. The grain size was 3.3 µm for AM0C after densification, but it decreased to 2.4 µm for AM1C, presumably due to the decreased time required for densification. In contrast to ceramics with 0 or 1 wt% carbon, the addition of 3 wt% carbon produced a distinct second phase. The densification time for AM3C was about the same as AM1C, but the presence of carbon inclusions pinned grains, which further reduced the average grain size of the resulting ZrB_2 to 1.8 µm. The addition of 3 wt% carbon resulted in the presence of ~10 vol% carbon in the final ceramic, which was particularly visible in polished sections (not shown). Based on SEM observation, the ceramic with 1 wt% carbon added appeared to be below the solid solubility limit for carbon in ZrB_2, which resulted in some reaction with oxides and the rest of the carbon dissolving into the ZrB_2 matrix during densification. In contrast, the addition of 3 wt% carbon was above the solid solubility limit, which resulted in the presence of visible carbon inclusions.[33] Overall, carbon additions reduced the grain size of ZrB_2 by two different mechanisms: 1) reduction of grain coarsening due to shorter times required for densification for both levels of carbon addition; and 2) grain pinning with carbon additions that produce a second phase, as in the 3 wt% addition case.

Raman spectroscopy was used to characterize the carbon inclusions observed in the AM3C ceramic (Figure 2). From the spectra, both the D peak (1333 cm^{-1}) and G peak (1585 cm^{-1}) were observed for the carbon inclusions. These peaks were due to sp^3 and sp^2 bonding, respectively. The presence of both sp^3 and sp^2 hybridization is common for micron sized grains of graphite.[34] Previous studies have concluded that the relative intensities of the D and G bands of the Raman patterns are related to the amount of disorder in the carbon.[34,35] The ratio of the area of the D peak to the G peak should be 0.75 for polycrystalline graphite,[35] as it was for the graphite standard. The ratio of the area of the D peak to G peak for typical carbon present around the grains in AM3C was 1.28. This ratio showed that the carbon around the ZrB_2 grains was graphitic, but that it had some disorder as indicated by the increased relative amount of sp^3 bonding. Carbon was also present as smaller inclusions having a rounded morphology and located at triple grain junctions. These spherical carbon inclusions were observed for both AM1C and AM3C. The ratio of the D to G peak areas was approximately 0.81 for the spherical inclusions, suggesting that the carbon had a lower degree of disorder, which nearly matched the graphite standard.

Measured Thermal Properties

Heat capacity was measured as a function of temperature up to 2000°C. Figure 3 shows heat capacity for AM0C, AM1C, and AM3C as well as NIST-JANAF data for ZrB_2. The results showed no distinguishable change in heat capacity for ZrB_2 with up to 3 wt% carbon additions. A minimum heat capacity of 44.80 J/mol•K was measured at 25°C, while above 600°C heat capacity increased linearly with temperature to a maximum measured value of 80.40 J/mol•K for AM1C at 2000°C. The heat capacity values measured in this study agreed with NIST-JANAF data (solid line in Figure 3) as well as the results published as part of other studies.[18,19,25,36] Below 1400°C, all of these values fell within a range of about 5% of the average. The heat capacity values can be described as a function of temperature by Equation (8), which was fit to data from the NIST-JANAF tables, and shown in Figure 3 by the solid line. Overall, the presence of a small volume fraction of carbon did not affect the measured heat capacity values.

$$Cp = 66.96 + 5.67 \times 10^{-3} T + 1.43 \times 10^{-6} T^{2} - 0.15 \times 10^{-9} T^{3} - 1.84 \times 10^{6} T^{-2} \qquad (8)$$

Steady state thermal diffusivity was measured as a function of carbon content from 200°C to 2000°C. For each material, the thermal diffusivity had a maximum value at 200°C and decreased to a minimum value at 2000°C (Figure 4). For example, the maximum thermal diffusivity for AM3C was 0.176 cm^2/sec at 200°C and it decreased to a minimum value of 0.143 cm^2/sec at 2000°C. Without added carbon, the thermal diffusivity decreased from a maximum of 0.149 cm^2/sec at 200°C to a minimum value of 0.129 cm^2/sec at 2000°C. Regardless of the carbon addition, the thermal diffusivity decreased up to 2000°C because of increased phonon scattering with increased temperature.

The thermal diffusivity values measured for ZrB_2 in the present study were consistent with values for other ZrB_2-based ceramics reported by Zimmermann et al.[25] and Guo et al.[36] Among the three materials measured in the present study, AM3C had the highest thermal diffusivity at 200°C with a value of 0.176 cm^2/sec compared to 0.149 cm^2/sec for AM0C. In contrast, AM1C had the lowest value of 0.129 cm^2/sec at 200°C. The dissolved carbon present in AM1C reduced its thermal diffusivity compared to AM0C because of a reduction in phonon transfer processes by forming a solid solution. In contrast, the presence of carbon as a second phase in AM3C increased its thermal diffusivity at 200°C to 0.176 cm^2/sec. The additional carbon phase in AM3C may have increased the thermal diffusivity of the ceramic due to the higher thermal diffusivity of graphite (0.53 cm^2/sec at 25°C) compared to ZrB_2.[37]

For ZrB_2 with carbon additions, the thermal diffusivity of the as processed specimens did not follow the same path upon heating and cooling during the first thermal cycle. The largest differences were noted in AM3C (Figure 5). The first diffusivity run started with a value of 0.118 cm^2/sec measured at 1000°C and increased up to 0.140 cm^2/sec at 2000°C. Upon cooling, the diffusivity increased further to 0.160 cm^2/sec at 1000°C. However, this initial measurement (i.e., heating the as-processed specimen to 2000°C) stabilized the value of thermal diffusivity so that the values measured in all subsequent runs followed the cooling path of the first run during both heating and cooling. Therefore, the second run (and all subsequent runs) for composition AM3C started at 0.160 cm^2/sec at 1000°C and decreased to 0.143 cm^2/sec at 2000°C. On cooling, the diffusivity followed the same path as heating, resulting in a diffusivity of 0.165 cm^2/sec at 800°C. This irreversible change in thermal diffusivity during the first run could have resulted from experimental factors such as debonding of the graphite coating, or changes in the specimen such as grain growth or new phase formation.

To determine the cause of the change in thermal diffusivity during the first heating cycle, SEM was used to analyze the microstructure of AM3C for both an as-processed specimen (i.e., before the initial thermal diffusivity measurement) and for a specimen that had been heated to 2000°C to measure thermal diffusivity (Figure 6). The specimens were not etched to avoid any potential microstructural changes and to highlight the morphology of the carbon inclusions. For AM3C, the as-processed material had an average grain size of 1.8 μm. The carbon was present as a second phase that was observed along grain boundaries. After heating to 2000°C, the average grain size of AM3C increased to 3.7 μm and a new phase with a lighter contrast was observed at some ZrB_2-carbon boundaries (see arrows in Figure 6(B)). Subsequently, x-ray diffraction was used to determine that the new phase was ZrC (discussed in more detail below). In addition to the formation of a new phase, the morphology of the carbon inclusions changed from mainly needle-like in the as-processed material to larger particles with a more equiaxed morphology after heating to 2000°C. The increase in thermal diffusivity observed during the initial heating cycle, therefore, was due to changes in the microstructure that did not noticeably affect the measured heat capacity values, which were the formation of ZrC and grain growth.

Quantitative x-ray diffraction confirmed that after cycling to 2000°C AM3C contained approximately 97.1 wt% ZrB_2 and 2.9 wt% ZrC (Figure 7). In addition, the observed ZrC peaks were shifted to higher 2θ values than those from the powder diffraction file card for pure ZrC (PDF card number 35-0784). The shift to higher 2θ values corresponds to a decrease in the ZrC lattice parameter from 4.691 Å reported for pure ZrC to 4.653 Å. The decrease suggests that some of the W that was introduced into the material as an impurity from the WC media used in the attrition milling process migrated into the ZrC that formed during thermal cycling. The total WC impurity content of the ceramics was ~2.2 wt% based on mass loss from the media. After hot pressing, WC appeared to be dissolved in the ZrB_2 matrix since no WC inclusions were observed in SEM and no WC peaks were detected by XRD. After heating to 2000°C, analysis of the lattice parameter of the ZrC showed that the ZrC grains contained ~15 wt.% W, which was equivalent to 0.45 wt% W based on a total system composition of 2.2 wt% WC.[38,39] Thus, even though ZrC made up only 2.67 vol% (2.9 wt%) of the specimen, it contained about 20% of the total W. Unlike ZrC, the XRD peaks for ZrB_2 in AM3C did not shift noticeably relative to those of pure ZrB_2 as the amount of W in the ZrB_2 (~1.7 wt% of the total specimen after heat treatment) resulted in shifts that were below the detection limit. The noticeable shift in ZrC lattice parameter after heat treatment indicated that W migrated preferentially to the (Zr,W)C phase. Reducing the impurity content of the ZrB_2 (i.e., migration of some of the W from that was originally in $(Zr,W)B_2$ to (Zr,W)C) would be expected to increase the thermal diffusivity of AM3C by decreasing phonon and electron scattering in the matrix phase.[40] Therefore, some of the increase in thermal diffusivity measured for AM3C after the first thermal cycle (and compared to AM0C) is due to a reduction in the W impurity content of the matrix phase.

To determine the temperature at which the irreversible changes in microstructure and thermal diffusivity occurred, thermal diffusivity was measured for as-processed AM3C specimens up to temperatures of 1450°C, 1550°C, and 1650°C (Figure 8). For specimens heated to 1450°C or 1550°C, no significant difference was observed between the heating and cooling paths indicating that no changes in microstructure occurred at these temperatures. In contrast, when measured up to 1650°C, the thermal diffusivity changed noticeably. Whereas the value at 200°C had been ~0.17 cm^2/sec in the as-processed state, or for the measurements after heating to the temperatures of 1550°C or lower, the thermal diffusivity at 200°C decreased to a value of ~0.14 cm^2/sec after heating to 1650°C. The thermal diffusivity decreased after heating to 1650°C as compared to an increase after heating to 2000°C, which indicated that the changes were not complete after heating to 1650°C. Full stabilization required heating to 2000°C, which resulted in a permanent increase in thermal diffusivity due to grain growth, the formation of ZrC, and migration of W impurities from ZrB_2 into the newly-formed ZrC.

Calculated Thermal Properties

Equation 3 was used to calculate thermal conductivity as a function of temperature and carbon additions from measured thermal diffusivity and NIST-JANAF heat capacity values after stabilization at 2000°C. The bulk density was calculated based on nominal composition as a function of temperature using thermal expansion data from Touloukian et al.[41] Heat capacity was calculated as a function of temperature using Equation (8). Thermal conductivity, shown in Figure 9, increased with increasing temperature for each composition, reaching a maximum value at 2000°C. Thermal conductivity was highest for AM3C and lowest for AM1C while values for AM0C were between the other two materials. For example, the highest thermal conductivity at 2000°C was 64.2 W/m•K for AM3C compared to 58.7 W/m•K for AM0C. The addition of 1 wt% carbon led to a decrease in grain size and, presumably, the dissolution of carbon into the ZrB_2, which decreased the thermal conductivity to 53.9 W/m•K at 2000°C. The addition of 3 wt% carbon led to the formation of carbon as a second phase, but also produced ZrC during the first thermal cycle after processing. The increase in thermal conductivity of AM3C after heating to 2000°C relative to the other two materials was due to the presence of carbon, the formation of ZrC, and the migration of W from the ZrB_2 into the ZrC.

Small additions of carbon (i.e., levels that could be expected to form a solid solution based on known phase equilibria)[33] were initially expected to increase the thermal conductivity of ZrB_2. Previous densification studies concluded that small additions of carbon (i.e., up to 2 wt%) reacted with and removed oxides present on the surfaces of ZrB_2 particles. In hot pressed ceramics, these oxides would be expected to form a grain boundary phase that would decrease thermal and electrical conductivities since the oxides are thermal and electrical insulators. Larger additions of carbon, which formed a second phase that was shown to be graphitic by Raman spectroscopy (Figure 2), were expected to increase thermal conductivity based on a simple dispersed phase models for thermal conductivity.[27,36] The dispersed phase model used, which can be described by Equation (9), estimated the thermal conductivity of a composite by summing the products of the volume fraction and thermal conductivity of each phase. For example, composition AM3C contained approximately 10 vol% graphite after the first thermal diffusivity measurement. If polycrystalline graphite with a thermal conductivity value of 150.0 W/m•K[42] at 400°C were added to ZrB_2 with a measured thermal conductivity of 44.5 W/m•K at 400°C, a value of approximately 57 W/m•K would be expected for AM3C. The measured value was 48.0 W/m•K, which was less than the value predicted by a simple dispersed phase composite model. The measured value, however, may have been lower than the prediction due to the phase and orientation of the carbon, as well as any preferred orientation of the graphite since the measurements were conducted on specimens perpendicular to the hot pressing direction.

$$\lambda = \sum_{i} v_i \lambda_i \tag{9}$$

To better understand the distribution of carbon in the three ZrB_2-based ceramics, STEM imaging was used (Figure 10). For AM0C, traces of carbon were observed along the grain boundaries while image analysis revealed ~1.4 vol% (0.42 wt%) in AM1C. Carbon was considered to be an isolated, trace phase in both of these materials, although AM1C was expected to have a significant amount of carbon dissolved into the ZrB_2 matrix since 1 wt% carbon was added. In contrast, the addition of 3 wt% carbon led to the presence of 10.8 vol% carbon in AM3C, which was present both as carbon dissolved into the ZrB_2 matrix and as carbon inclusions. The carbon inclusions in AM3C also had a pronounced aspect ratio, estimated to be ~12 using image analysis software. Previous work done by Garboczi et al. with percolation theory showed that with an aspect ratio of 12, the percolation threshold is 7.8 vol% in a polycrystalline matrix, indicating that the carbon observed in AM3C could be above the percolation threshold.[43] Therefore, the carbon inclusions were likely to form a network having random, 3D connectivity. Further, the connected carbon network could be responsible for part, if not all, of the increase in thermal conductivity of AM3C relative to AM0C because graphite has a higher thermal conductivity than the ZrB_2 matrix.

Electrical conductivity was measured as a function of temperature for all of the specimens to separate the electron and phonon contributions to thermal conductivity. Figure 11 shows that electrical conductivity for AM0C decreased with increasing temperature with a maximum value of $2.96 \times 10^4\ \Omega^{-1}cm^{-1}$ at 300°C. The electrical conductivity decreased with 1 wt% carbon addition to $2.54 \times 10^4\ \Omega^{-1}cm^{-1}$ and increased to $3.5 \times 10^4\ \Omega^{-1}cm^{-1}$ with 3 wt% carbon addition at 300°C. For comparison, the magnitude of conductivity for the ZrB_2 ceramics in this study were comparable to that of nickel based alloys, which have a reported conductivity of 3.6 x 10^4 Ω^{-1}cm^{-1} at 300°C.[44] Based on measured electrical conductivity, it appears that dissolution of carbon into the ZrB_2 matrix decreased its electrical conductivity and, therefore, the electron contribution to thermal conductivity in AM1C. In AM3C, the excess carbon formed ZrC and pulled W out of solid solution with ZrB_2, forming (Zr,W)C which increased the electrical conductivity of AM3C compared to AM0C.

The electrical conductivity for all of the ZrB_2 ceramics increased as the inverse temperature increased, which indicated that electron transfer was the dominant electrical conduction mechanism. After the materials were cycled to 2000°C, the electrical conductivity was measured up to 1300°C, where a minimum electrical conductivity of 1.35 x 10^4 Ω^{-1}cm^{-1} was measured for AM0C. For higher temperatures, electrical conductivity values were estimated by extrapolating the linear portion of the conductivity curve up to 2000°C. The relationship between electrical conductivity and temperature suggests that metallic bonding in ZrB_2 is responsible for the high thermal and electrical conductivities.

The electron contribution to thermal conductivity was calculated from the electrical conductivity using the Wiedemann-Franz law (Equation (10)), where L is the Lorentz number (2.45 x 10^{-8} W•Ω•K^{-2}), σ_e is the electrical conductivity, and T is the absolute temperature.[45] The phonon contribution was then estimated by subtracting the electron contribution from the total thermal conductivity. Figure 12 illustrates electron and phonon contributions to thermal conductivity as a function of temperature and carbon addition. Figure 12a shows that the electron contribution dominated thermal conductivity for AM0C, comprising about 90% of the total thermal conductivity at 2000°C.

$$k_e = L\sigma_e T \tag{10}$$

Figures 12b and 12c show the electron and phonon contributions to thermal conductivity for AM0C, AM1C and AM3C. The electron contribution displayed a similar trend with carbon addition as the overall thermal conductivity (Figure 9), wherein the addition of 1 wt% carbon led to a decrease in the electron contribution for all temperatures tested, but the addition of 3 wt% carbon led to an increase in the electron contribution. The presence of dissolved carbon in the ZrB_2 matrix in AM1C decreased the electronic portion of the conductivity due to solid solution formation, which decreased electrical conductivity of the ZrB_2 matrix. Interestingly, the addition of 1 wt% carbon did not appear to affect the overall phonon contribution to thermal conductivity as both AM0C and AM1C had phonon contributions of ~6 W/m•K at temperatures above 800°C. Thus, the dissolution of carbon into the ZrB_2 matrix did not appear to influence phonon transport, but decreased overall thermal conductivity of AM1C by decreasing the electron contribution to thermal conductivity.

In contrast to the lower carbon additions, AM3C had the highest value for the electron contribution to thermal conductivity with a value of 67 W/m•K at 2000°C compared to 47 W/m•K for AM1C and 54 W/m•K for AM0C. The increase in electron contribution, the dominant conduction mechanism for all of the specimens, was due to an increased in electrical conductivity. The increase was at least partially due to an increase in conductivity of the ZrB_2 matrix due to the reduced amount of W in solid solution in ZrB_2 after the formation of (Zr,W)C (2.67 vol%) in AM3C. The phonon contribution to thermal conductivity at 200°C decreased to near zero when 3 wt% carbon was added, compared to ~ 6 W/m•K for the AM0C and AM1C (Figure 12c). The decrease in the phonon contribution to thermal conductivity may have been due to the formation of graphite precipitates, which formed a percolating network of elongated and highly oriented graphite particles. Apparently, the formation of the second phase decreased phonon conduction. The overall increase in thermal conductivity of AM3C was, therefore, due to the increase in the electrical contribution that overcame a decrease in the phonon contribution. The increase in the electron contribution was due to the preferential migration of W from the ZrB_2 matrix to the newly formed ZrC phase when AM3C was heated to 2000°C.

Conclusion

ZrB_2 with carbon additions of 0 to 3 wt% was densified by hot pressing at 1900°C. The size of the ZrB_2 grains decreased from 3.3 μm in AM0C to 2.4 μm in AM1C because the added carbon reacted with and removed oxygen impurities, which reduced the time necessary for densification at 1900°C and reduced the effects of grain coarsening. The addition of 3 wt% carbon led to further reductions in the grain size to 1.8 μm after hot pressing due to the pinning effect of carbon inclusions in AM3C. Raman spectroscopy showed that the residual carbon found at grain boundaries in AM3C was graphitic. Regardless of the amount of carbon addition, the measured heat capacity of ZrB_2 did not change compared to nominally pure ZrB_2. Thermal diffusivity increased to over 0.17 cm^2/sec at 200°C with for AM3C compared to 0.15 cm^2/sec for AM0C. During the first heating cycle, the thermal diffusivity changed irreversibly above 1500°C.

This was attributed to ZrC formation, growth of ZrB_2 grains, and the migration of W from the ZrB_2 matrix into the newly formed ZrC phase.

Thermal conductivity was calculated up to 2000°C from the measured thermal diffusivity and heat capacity. Similar to thermal diffusivity, thermal conductivity was highest for AM3C at 64.2 W/m•K compared to 58.7 W/m•K for AM0C. For AM3C, the addition of 3 wt% carbon led to the presence of 10.8 vol% carbon in the hot pressed ceramic, which was above the calculated percolation threshold in the ZrB_2 matrix. The distinct second phase of oriented graphite and ZrC decreased the phonon contribution to thermal conductivity to nearly zero. The decrease in W impurity content in the ZrB_2 matrix increased the electron contribution to thermal conductivity and gave AM3C the highest thermal conductivity.

Acknowledgements

The authors would like to acknowledge the AMCL at Missouri S&T for use of SEM, STEM, FIB, and XRD.

References

1. L.S. Sigl, R. Telle, and K. Takagi, "Boride-Based Hard Materials," pp. 802-945 in *Handbook of Ceramic Hard Materials.* Edited by R. Riedel. Wiley-VCH, Weinheim, Germany, 2000.

2. D.E. Wiley, W.R. Manning, and O. Hunter Jr, "Elastic properties of polycrystalline TiB_2, ZrB_2 and HfB_2 from room temperature to 1300K," *Journal of the Less Common Metals,* **18** [2] 149-57 (1969).

3. R.A. Cutler, "Engineering Properties of Borides," pp. 787-803 in Vol. 4, *Ceramics and Glasses: Engineered Materials Handbook.* Edited by S. J. S. Jr. ASM International, Materials Park, OH, 1991.

4. X. Zhang, X. Luo, J. Han, J. Li, and W. Han, "Electronic structure, elasticity and hardness of diborides of zirconium and hafnium: First principles calculations," *Computational Materials Science,* **44** [2] 411-21 (2008).

5. O. Kida, "Monolithic Refractory Material and Waste Melting Furnace Using the Same," Japanese Patent JP2000335969, May 12, 2000.

6. M.M. Opeka, I.G. Talmy, and J.A. Zaykoski, "Oxidation-based materials selection for 2000C + hypersonic aerosurfaces: Theoretical considerations and historical experience: Special Section: Ultra-High Temperature Ceramics (Guest Editors: Joan Fuller and Michael D. Sacks)," *Journal of Materials Science,* **39** 5887-904 (2004).

7. W. G. Fahrenholtz, G. E. Hilmas, I G. Talmy, and J. A. Zaykoski, "Refractory Diborides of Zirconium and Hafnium," *Journal of the American Ceramic Society,* **90** [5] 1347-64 (2007).

8. S. Zhu, W.G. Fahrenholtz, G.E. Hilmas, and S.C. Zhang, "Pressureless sintering of carbon-coated zirconium diboride powders," *Materials Science and Engineering: A,* **459** [1-2] 167-71 (2007).

9. S. Baik and P.F. Becher, "Effect of Oxygen Contamination on Densification of TiB_2," *Journal of the American Ceramic Society,* **70** [8] 527-30 (1987).

10. S. C. Zhang, G. E. Hilmas, and W. G. Fahrenholtz, "Pressureless Densification of Zirconium Diboride with Boron Carbide Additions," *Journal of the American Ceramic Society,* **89** [5] 1544-50 (2006).

11. D. Sciti, A. Balbo, and A. Bellosi, "Oxidation behaviour of a pressureless sintered HfB_2-$MoSi_2$ composite," *Journal of the European Ceramic Society,* **29** [9] 1809-15 (2009).

12. William G. Fahrenholtz, Gregory E. Hilmas, Shi C. Zhang, and Sumin Zhu, "Pressureless Sintering of Zirconium Diboride: Particle Size and Additive Effects," *Journal of the American Ceramic Society,* **91** [5] 1398-404 (2008).

13. M.J. Thompson, W.G. Fahrenholtz, and G.E. Hilmas, "Effect of Starting Particle Size and Oxygen Content on Densification of ZrB_2," *Journal of the American Ceramic Society,* **Accepted for Publication 8/2/2010**.

14. M. Gasch, D. Ellerby, E. Irby, S. Beckman, M. Gusman, and S. Johnson, "Processing, properties and arc jet oxidation of hafnium diboride/silicon carbide ultra high temperature ceramics: Special Section: Ultra-High Temperature Ceramics (Guest Editors: Joan Fuller and Michael D. Sacks)," *Journal of Materials Science,* **39** 5925-37 (2004).

15. A.L. Chamberlain, W.G. Fahrenholtz, G.E. Hilmas, and D.T. Ellerby, "High-Strength Zirconium Diboride-Based Ceramics," *Journal of the American Ceramic Society,* **87** [6] 1170-2 (2004).

16. S.-Q. Guo, Y. Kagawa, T. Nishimura, D. Chung, and J.-M. Yang, "Mechanical and physical behavior of spark plasma sintered ZrC-ZrB_2-SiC composites," *Journal of the European Ceramic Society,* **28** [6] 1279-85 (2008).

17. D. Sciti, L. Silvestroni, G. Celotti, C. Melandri, and S. Guicciardi, "Sintering and Mechanical Properties of ZrB_2–$TaSi_2$ and HfB_2–$TaSi_2$ Ceramic Composites," *Journal of the American Ceramic Society,* **91** [10] 3285-91 (2008).

18. M.M. Opeka, I.G. Talmy, E.J. Wuchina, J.A. Zaykoski, and S.J. Causey, "Mechanical, Thermal, and Oxidation Properties of Refractory Hafnium and zirconium Compounds," *Journal of the European Ceramic Society,* **19** 2405-14 (1999).

19. M. Gasch, S. Johnson, and J. Marschall, "Thermal Conductivity Characterization of Hafnium Diboride-Based Ultra-High-Temperature Ceramics," *Journal of the American Ceramic Society,* **91** [5] 1423-32 (2008).

20. M.W. Chase, *NIST-JANAF Thermochemical Tables*. American Chemical Society and the American Institute of Physics, Woodbury, NY, 1998.

21. L.N. Grossman, "High-Temperature Thermophysical Properties of Zirconium Carbide," *Journal of the American Ceramic Society,* **48** [5] 236-42 (1965).

22. S.E. Landwehr, G.E. Hilmas, W.G. Fahrenholtz, I.G. Talmy, and H. Wang, "Thermal properties and thermal shock resistance of liquid phase sintered ZrC-Mo cermets," *Materials Chemistry and Physics,* **115** [2-3] 690-5 (2009).

23. R.P. Tye and E.V. Clougherty, "The Thermal and Electrical Conductivities of some Electrically Conducting Compounds," *Proceedings of the Fifth Symposium on Thermophysical Properties,* 396-401 (1970).

24. G. Grimvall, "Thermal Conductivity," *pp. 255-285 in Thermophysical Properties of Materials,* North-Holland Physics Publishing, Amsterdam, Netherlands (1986).

25. J.W. Zimmermann, G.E. Hilmas, W.G. Fahrenholtz, R.B. Dinwiddie, W.D. Porter, and H. Wang, "Thermophysical Properties of ZrB2 and ZrB2-30SiC Ceramics," *Journal of the American Ceramic Society,* **91** [5] 1405-11 (2008).

26. D.A.G. Bruggeman, "Berechnung verschiedener physikalischer Konstanten von heterogenen Substanzen. I. Dielektrizita ¨ tskonstanten und Leitfa ¨ higkeiten der Mischko ¨ rper aus isotropen Substanzen,’’ Ann," *Phys. (Leipzig,* **24** 636-79 (1935).

27. D. Stroud, "Generalized effective-medium approach to the conductivity of an inhomogeneous material," *Physical Review B,* **12** [8] 3368 (1975).

28. D.S. Smith, S. Fayette, S. Grandjean, C. Martin, R. Telle, and T. Tonnessen, "Thermal Resistance of Grain Boundaries in Alumina Ceramics and Refractories," *Journal of the American Ceramic Society,* **86** [1] 105-11 (2003).

29. ASTME1461, "Standard Test Method for Thermal Diffusivity of Solids by the Flash Method," *ASTM International,* (2001).

30. L.M. Clark and R.E. Taylor, "Radiation loss in the flash method for thermal diffusivity," *Journal of Applied Physics,* **46** [2] 714-9 (1975).

31. K. Shinzato and T. Baba, "A Laser Flash Apparatus for Thermal Diffusivity and Specific Heat Capacity Measurements," *Journal of Thermal Analysis and Calorimetry,* **64** [1] 413-22 (2001).

32. ASTMF76, "Standard Test Methods for Measuring Resistivity and Hall Coefficient and Determining Hall Mobility in Single-Crystal Semiconductors," *ASTM International,* (2008).

33. ACerS-NIST, Phase Equilibria Diagrams, [Computer Program] ACerS-NIST Phase Equilibria for Ceramics Program, 2004.

34. A.C. Ferrari and J. Robertson, "Interpretation of Raman spectra of disordered and amorphous carbon," *Physical Review B,* **61** [20] 14095 (2000).

35. E.F. Antunes, A.O. Lobo, E.J. Corat, V.J. Trava-Airoldi, A.A. Martin, and C. VerÌssimo, "Comparative study of first- and second-order Raman spectra of MWCNT at visible and infrared laser excitation," *Carbon,* **44** [11] 2202-11 (2006).

36. S. Guo, Y. Kagawa, T. Nishimura, and H. Tanaka, "Thermal and Electric Properties in Hot-Pressed ZrB2-MoSi2-SiC Composites," *Journal of the American Ceramic Society,* **90** [7] 2255-8 (2007).

37. P.G. Klemens, " The Specific Heat and Thermal Conductivity of Graphite," *Australian Journal of Physics,* **6** 405-9 (1953).

38. V.N. Eremenko and T.Y. Velikanova, "Use of the phase diagrams of ternary transition metal systems containing carbides in the development of heat-resisting hard alloys," *Powder Metallurgy and Metal Ceramics,* **22** [12] 1010-21 (1983).

39. M. Craft, "Sintering and Microstructural Effects on the Mechanical Properties of Zirconium Carbide-Tungsten Cermets"; Ceramic Engineering Thesis. Missouri University of Science and Technology, Rolla, 2010.

40. H.J. Juretschke and R. Steinitz, "Hall effect and electrical conductivity of transition-metal diborides," *Journal of Physics and Chemistry of Solids,* **4** [1-2] 118-27 (1958).

41. Y. Touloukian, C. Ho, and D. Dewitt, *Thermal Expansion: Nonmetallic Solids,* Vol. 13. Edited by Touloukian. IFI/Plenum, New York, 1970.

42. D.F. Pedraza and P.G. Klemens, "Effective Conductivity of Polycrystalline Graphite," *Carbon,* **31** [6] 951-6 (1993).

43. E.J. Garboczi, K.A. Snyder, J.F. Douglas, and M.F. Thorpe, "Geometrical percolation threshold of overlapping ellipsoids," *Physical Review E,* **52** [1] 819-28 (1995).

44. B. Sundqvist, "Electrical resistance of nickel in the range 300-725 K and 0-2 GPa," *Physical Review B,* **38** [17] 12283 (1988).

45. R. Franz and G. Wiedemann, "Ueber die Wärme-Leitungsfähigkeit der Metalle," *Annalen der Physik,* **165** [8] 497-531 (1853).

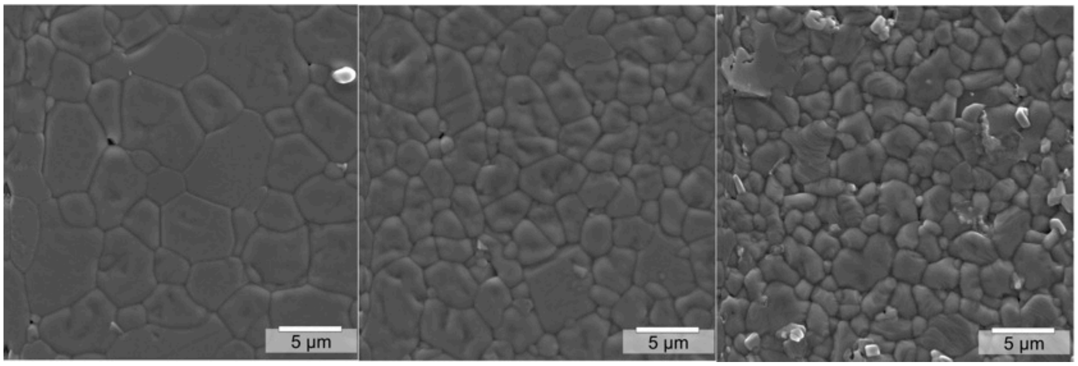

Figure 1: SEM images of AM0C (left), AM1C (center), and AM3C (right). These specimens were sectioned perpendicular to the hot pressing direction, polished, and then thermally etched to highlight the grain boundaries.

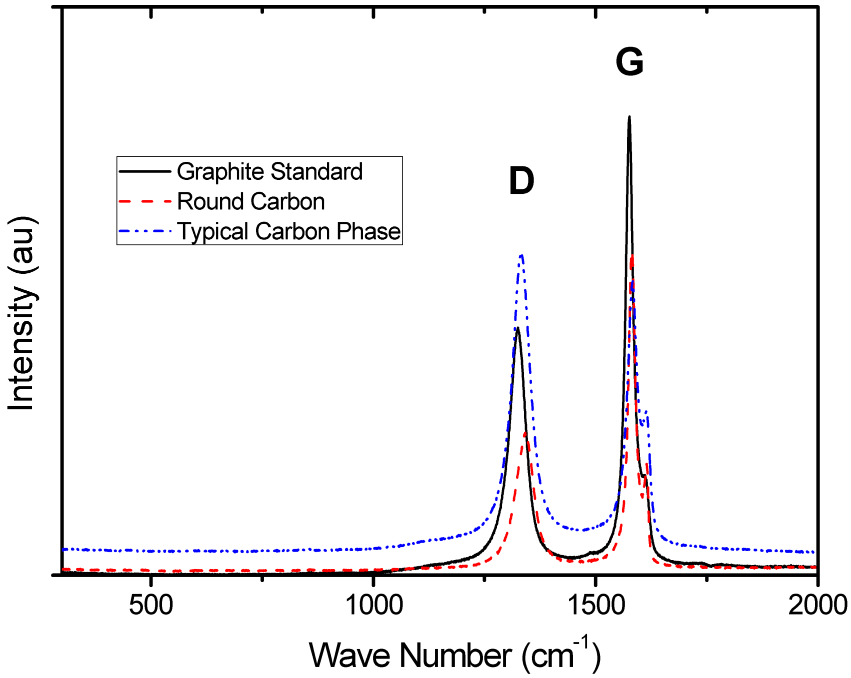

Figure 2: Raman patterns for AM3C and a polycrystalline graphite standard showing that two forms of carbon were present. The ratio of the area of the D peak to the area of the G peak was 0.75 for polycrystalline graphite, 1.28 for typical carbon inclusions observed in AM3C, and 0.81 for round carbon inclusions from AM3C.

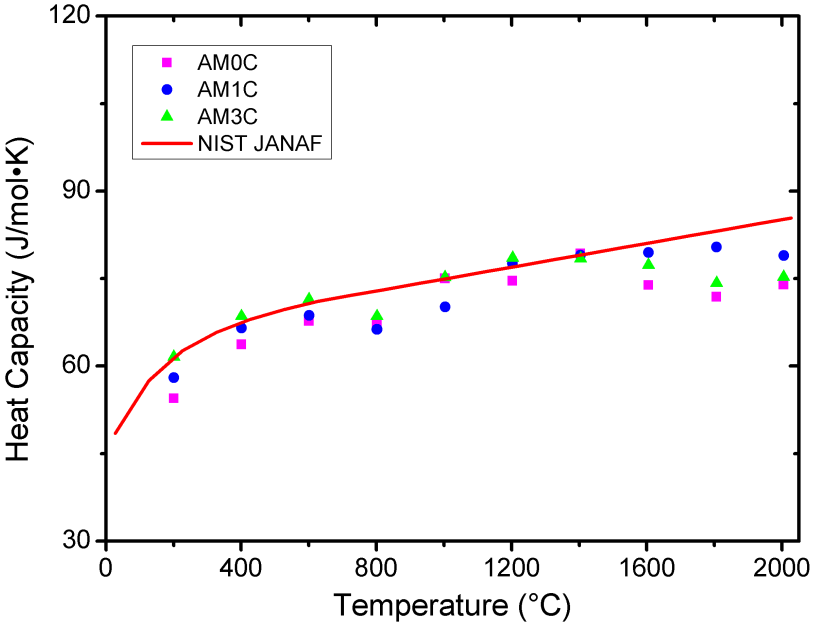

Figure 3: Heat capacity as a function of temperature for AM0C, AM1C, and AM3C. Data from NIST JANAF tables are also shown for comparison.

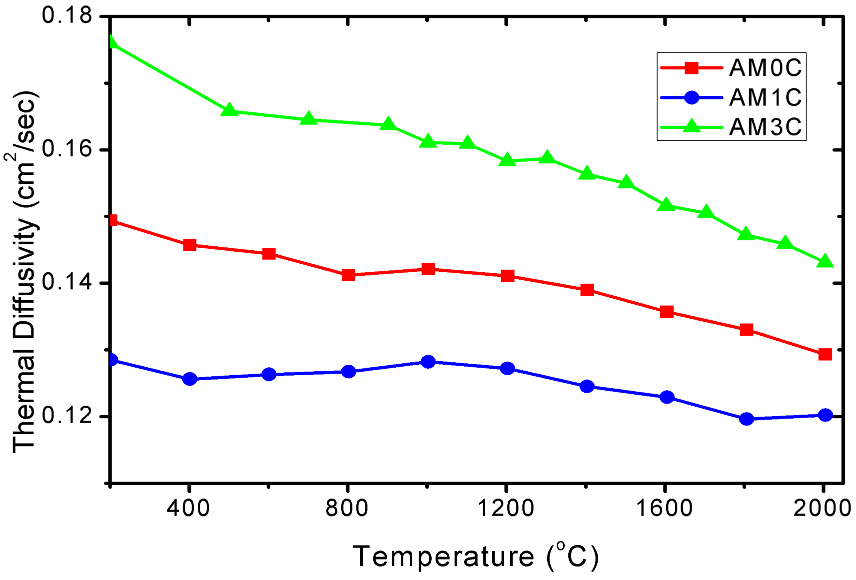

Figure 4: Thermal diffusivity as a function of temperature measured during cooling from 2000°C for ZrB_2 ceramics with three different carbon contents.

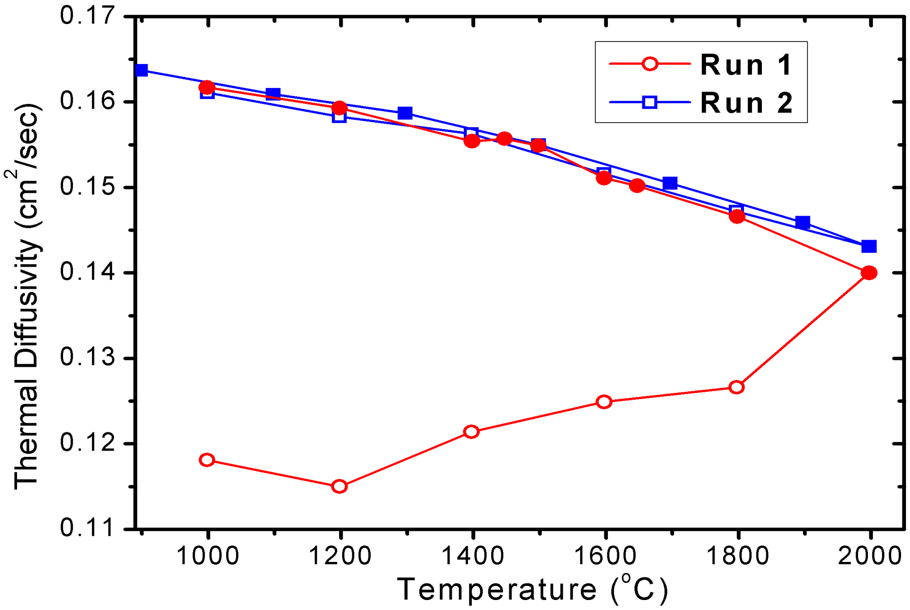

Figure 5: Thermal diffusivity as a function of temperature during heating (open symbols) and cooling (filled symbols) of AM3C for its first diffusivity run (circles) and a second run (squares).

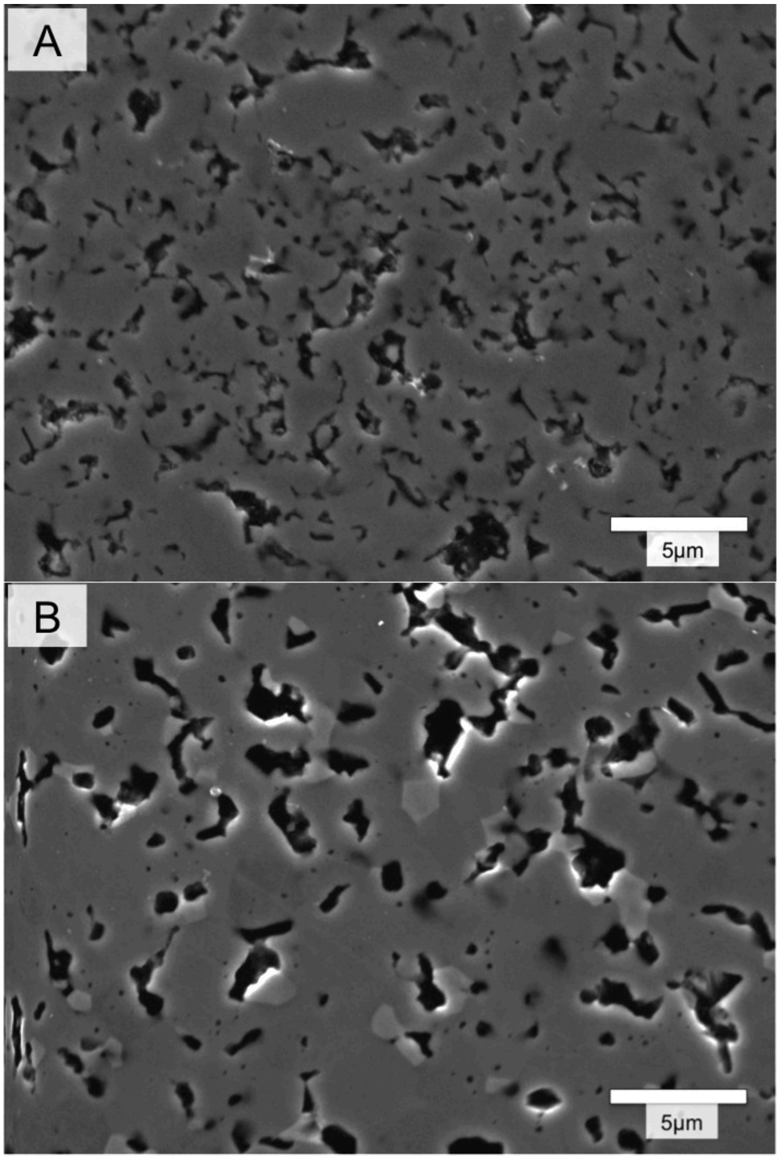

Figure 6: SEM images of polished AM3C as processed (A) and after thermal diffusivity measurement up to 2000°C (B). Noticeable differences include: ZrB_2 grain growth, graphitic carbon growth, decrease in aspect ratio, and ZrC formation.

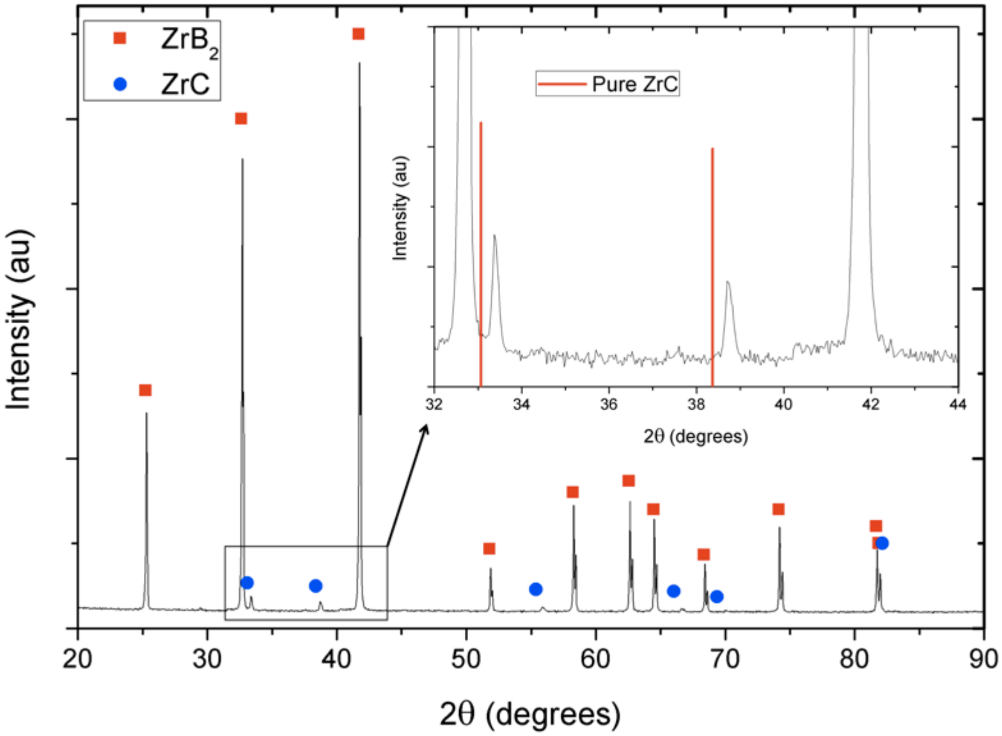

Figure 7: X-ray diffraction pattern for AM3C after heating to 2000°C shows the presence of ZrB_2 and ZrC. The ZrC peaks were shifted to higher angles than the ZrC standard (indicated by vertical lines on inset).

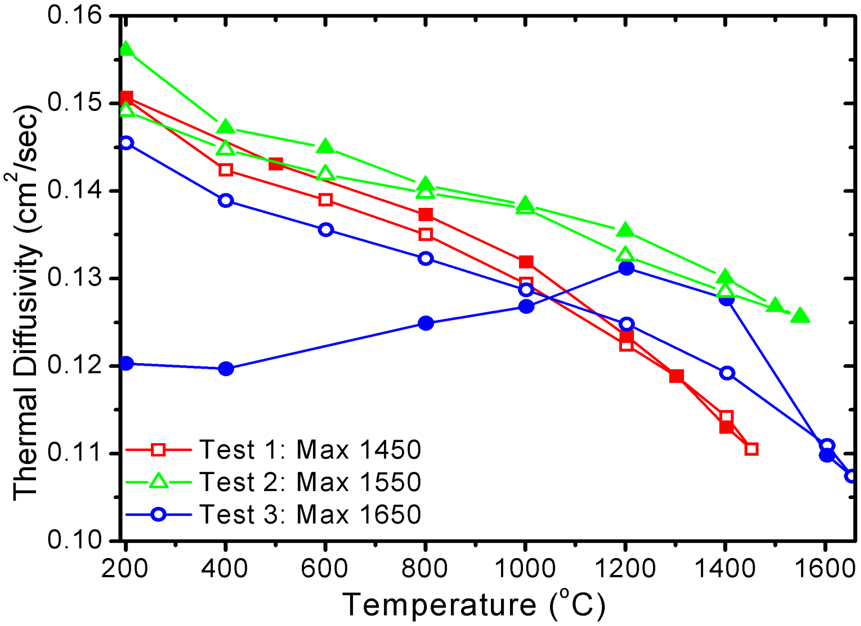

Figure 8: Thermal diffusivity as a function of temperature for AM3C specimens run to maximum temperatures of 1450°C (squares), 1550°C (triangles), and 1650°C (circles) showing the measured diffusivity during heating (open symbols) and cooling (filled symbols).

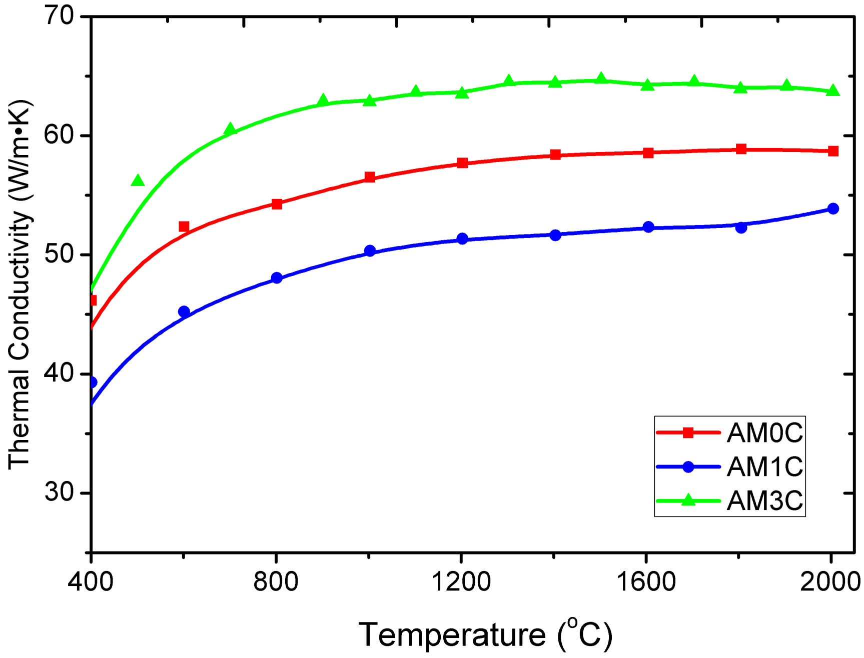

Figure 9: Thermal conductivity as a function of temperature for AM0C, AM1C, and AM3C calculated from measured heat capacity and thermal diffusivity.

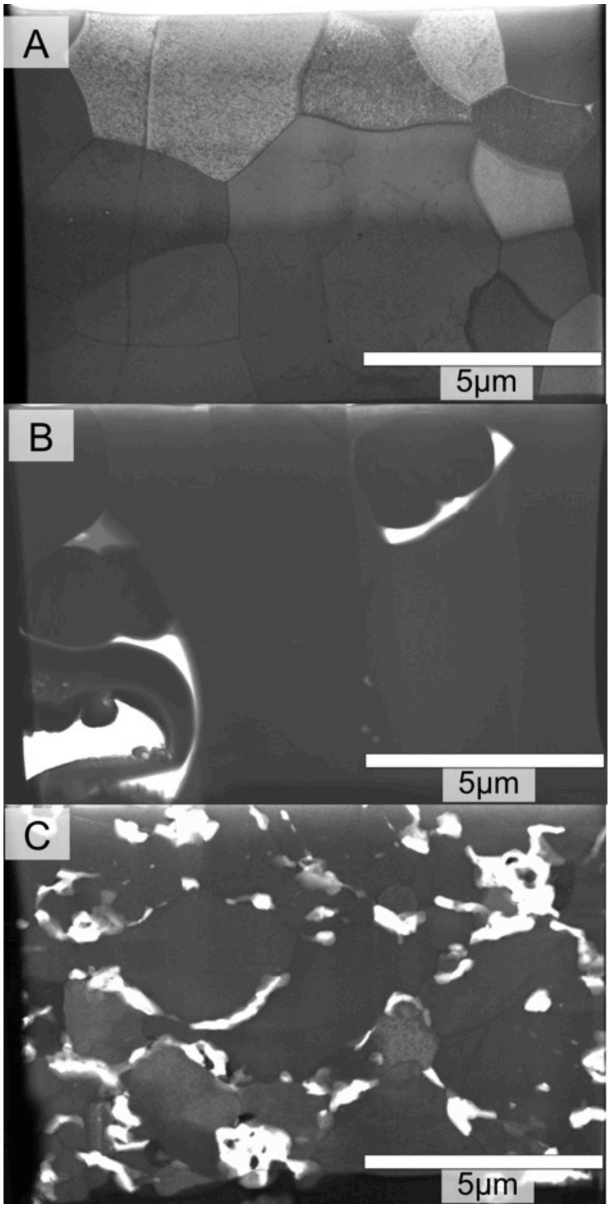

Figure 10: STEM images of AM0C (A), AM1C (B), and AM3C (C), all of which show evidence of carbon at the grain boundaries in AM1C and AM3C.

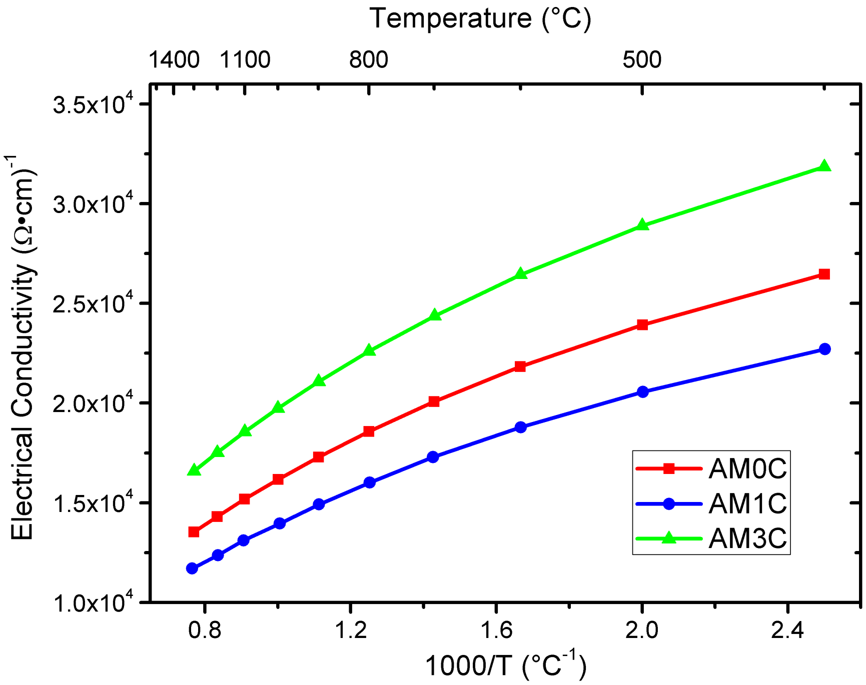

Figure 11: Electrical conductivity of AM0C, AM1C, and AM3C as a function of temperature.

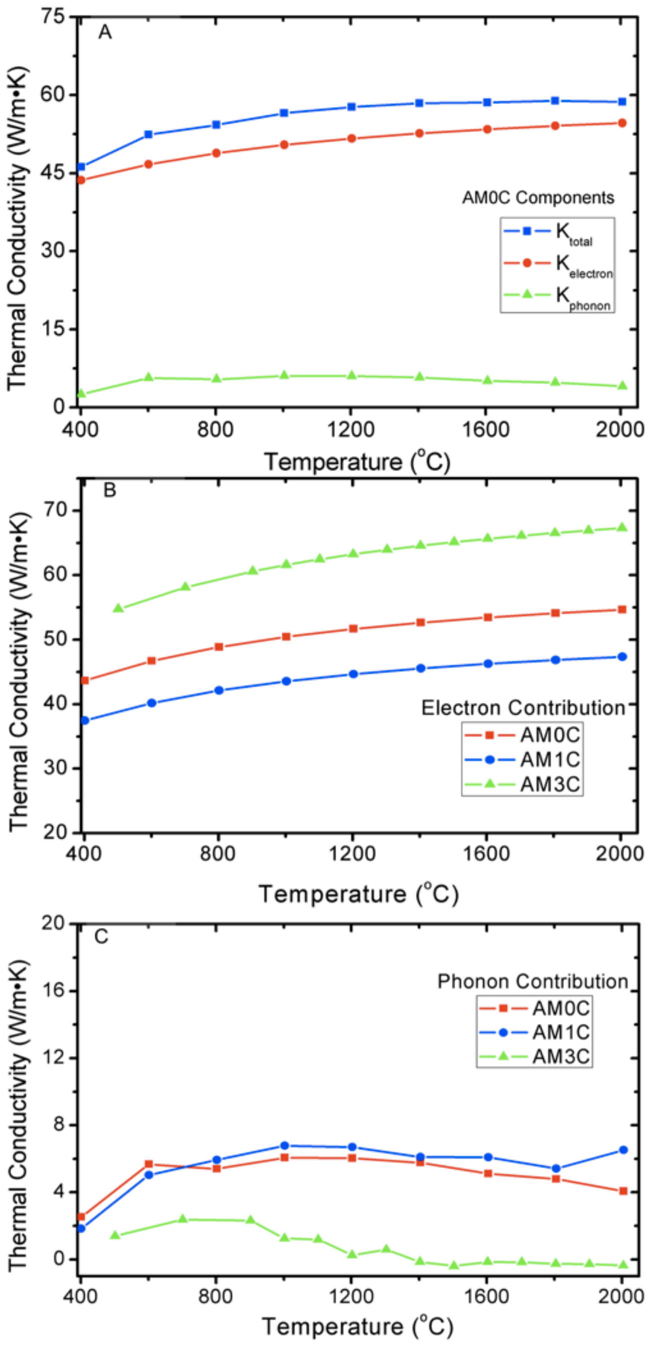

Figure 12: Electron and phonon contribution to thermal conductivity of AM0C, AM1C, and AM3C measured to 1200°C and extrapolated to 2000°C. AM0C total thermal conductivity with electron and phonon contributions is shown in (a), electron contributions of compositions in (b), and phonon contributions of compositions in (c).

3. HEATING RATE EFFECTS ON THE THERMAL AND MECHANICAL PROPERTIES OF ZRB$_2$

Matthew Thompson*; William G. Fahrenholtz; Greg E. Hilmas;
Dept. of Materials Science and Engineering
Missouri University of Science and Technology, Rolla, MO 65401

Abstract

Zirconium diboride ceramics were densified by hot pressing and spark plasma sintering with heating rates varying from as low as 5°C/min up to 300°C/min. Slower heating rates produced larger grains due to the longer times at temperatures between 1500°C and 1900°C, which is the temperature range in which ZrB$_2$ grains coarsen. Heating rates above 50°C/min resulted in rapid densification, but this led to the retention of up to 3.3 vol% of ZrO$_2$ in the microstructure. After densification, changes to the microstructure were evaluated to interpret the effects of heating rate on thermal and mechanical properties. The flexure strength of ceramics processed by hot pressing with a heating rate of up to 80°C/min was proportional to the inverse square root of the maximum grain size based on the Griffith criteria. Conversely, densification by spark plasma sintering, which had heating rates of up to 300°C/min resulted in microcracks, which decreased the elastic modulus from >500 GPa for pristine specimens to <485 GPa for microcracked materials. The use of heating rates >20°C/min also reduced the thermal conductivity due to the presence of retained ZrO$_2$, but improved the strength by reducing the maximum grain size.

Introduction

Zirconium diboride (ZrB_2) belongs to a class of materials known as ultrahigh temperature ceramics (UHTCs). These materials have melting temperatures >3000°C, high elastic moduli (~520 GPa), and high hardness values (20-25GPa).[1-4] This combination of properties makes UHTCs candidates for a variety of applications including refractory linings, cutting tools, and molten metal crucibles.[5] ZrB_2 and other diborides also have high thermal (>50 W/m•K)[6-8] and electrical (~10^7 S/m)[7,8] conductivities, which makes them excellent candidates for applications in extreme environments such as high temperature electrodes and thermal protection systems for hypersonic aerospace vehicles.[9]

ZrB_2 has strong covalent bonding and low self-diffusion coefficients, which generally requires temperatures >1900°C and/or external pressure to achieve full density.[10-12] Hot pressing has typically been used to densify ZrB_2.[10,13,14] Oxide impurities, which are usually present as oxide layers on particle surfaces, cause grain coarsening at temperatures below the onset of densification that further reduces the driving force for densification.[15] Additives have been used to react with and remove oxide impurities from particle surfaces to improve densification.[16] Carbon and boron carbide are common additives,[17,18] while WC and $MoSi_2$ have also been shown to enhance densification.[19-21] These additives not only enhance densification, but can also lead to improved strength due to decreased grain size. In the case of $MoSi_2$, additives can also improve oxidation resistance by promoting formation of a SiO_2-rich passive oxide layer.[11,21]

Spark plasma sintering (SPS) has also been used to densify ZrB_2. SPS, which is also called pulsed electric current sintering or field assisted sintering, boasts high heating rates (up to 600°C/min) and rapid densification times (typically 5 min or less at maximum temperature), which has been attributed to the direct heating of the powder and die.[12,13,22] During SPS, a DC current is passed through a die in short pulses (~20 msec). The current heats the specimen and die directly by so-called Joule heating while a uniaxial force is simultaneously applied.[13,23] This combination results in rapid densification, which reduces the effects of grain coarsening and produces room temperature mechanical properties that are superior to those of hot pressed materials.[24,25]

For thermal protection systems for future hypersonic vehicles, the thermal properties are as important as mechanical properties for performance of leading edges. Reported thermal conductivity values for ZrB_2 are typically ~60 W/m•K, but can be as high as 120 W/m•K.[7] High thermal conductivity is desirable since the heat generated at sharp leading edges much be conducted away from where it is generated to cooler areas where it can be dissipated by radiation.[9] Thermal conductivity is affected by a number of microstructural and compositional factors including relative density, grain size, and additives/impurities. Additives like carbon, SiC, and $MoSi_2$ that are used to improve densification and/or mechanical properties also affect thermal conductivities of the resulting ceramics.[7,26] These additives typically decrease the thermal conductivity by scattering both electrons and phonons.

Thermal conductivity can be difficult to measure directly. As a result, thermal diffusivity and heat capacity are typically measured and then used to calculate thermal conductivity. Both Gasch et al. and Zimmermann et al. found that heat capacity was not affected significantly by additions of up to 30 vol% SiC, 5 vol% $TaSi_2$, or 2 vol% Ir.[27,28] Thus, changes in thermal conductivity were attributed to changes in thermal diffusivity.

The thermal diffusivity of ZrB_2 has been measured by a number of researchers.[7,8,20,28,29] Typically, thermal diffusivity is measured by the laser flash technique, and values > 0.25 cm^2/sec have been reported at room temperature for ZrB_2 based materials.[7,26,28] However, the values are sensitive to changes in processing conditions (e.g., impurities, additives, densification time and temperature, etc.) that affect the composition, grain size, and relative density of the resulting ceramics.

The purpose of this investigation was to determine the effect of heating rate during hot pressing and spark plasma sintering on the thermal and mechanical properties of ZrB_2.

Procedure

Commercially available ZrB_2 (Grade B, H. C. Starck, Goslar, Germany) was used for this study. The powder was attrition milled in hexane for two hours using Co-bonded WC milling media in a fluoropolymer lined bucket. The resulting slurry was rotary evaporated to remove the hexane. Milling reduced the average particle size of the ZrB_2 from ~2 μm (supplier data) to ~0.22 μm, which was measured by laser light scattering (Microtrac S3500, Montgomeryville, PA). The mass of the WC milling media was measured before and after milling, which indicated that ~2 wt% WC was incorporated into the ZrB_2 powder. The oxygen content of the resulting powder was measured to be 2.06 wt% by the Leco Method (analysis performed by NSL Analytical, Cleveland, OH). The resulting powder was then passed through a 50 mesh sieve.

Hot pressed (HP) specimens were prepared by using a graphite die in a resistively heated graphite element hot press (Thermal Technology Inc., Model HP20-3060-20, Santa Rosa, CA). The graphite die was lined with graphite paper and coated with boron nitride (Cerac, SP-108, Milwaukee, WI) to minimize reactions between the die and the ZrB_2. Specimens were heated at rates from 5°C/min to 80°C/min throughout their respective hot pressing cycles. Below 1500°C, specimens were heated at the selected rate in a mild vacuum (20 Pa). Isothermal holds of 1 hour were used at 1300°C and 1500°C during heating to allow reactions involving the surface oxides and/or WC impurities to go to completion.[14,18] After the hold at 1500°C, the atmosphere was changed to flowing Ar gas at a pressure of ~10^5 Pa (nominally 1 atm) and a uniaxial pressure of 32 MPa was applied. Specimens were then ramped at the selected rate to 1900°C. When the densification temperature was reached, the furnace was held at that temperature until ram travel had stopped for 10 minutes. The furnace was then allowed to cool at an average of 40°C/min for all specimens. The external pressure was released below 1650°C.

Spark plasma sintered (SPS) specimens were prepared using a graphite paper lined graphite die and coated with boron nitride, similar to the procedure used for hot pressing. Prior to loading into the SPS die, powders were heated to 1500°C under mild vacuum (nominally 20 Pa) for one hour without an applied pressure in the graphite hot press to remove any possible volatile species. The specimens were then spark plasma sintered (HP D25[3], FCT Systeme GmbH, Rauenstein, Germany) to 1900°C for 15 minutes using heating rates ranging from 50°C/min to 300°C/min under mild vacuum, ~40 Pa (285 mTorr). During heating, a pressure of 5 MPa was applied to the die to ensure that current passed through the die. The pressure was increased to 32 MPa when the die

---

[3] Spark Plasma Sintering was completed at WPAFB in Dayton, OH.

reached 1500°C. The resulting dense specimens were then labeled according to the densification technique and heating rate (e.g., HP5 means hot pressed with a heating rate of 5°C/min).

The bulk density of each specimen was measured by the Archimedes' technique (ASTM standard C373)[30] using vacuum infiltration with distilled water as the immersing medium. Billets were then machined into squares approximately 12.5 mm by 12.5 mm that were 3 mm thick. The outer portions of the billets (~1 mm on each surface that contacted the die) were removed so that any portion of the specimen that may have reacted with the graphite dies was not used.

Flexure strength was measured by four-point bending according to ASTM standard C1161 using a semi-articulated fixture and a screw-driven load frame (Model 5881, Instron Corp., Norwood, MA) using type A bars (1.5 mm x 2 mm x 25 mm).[31] All specimens were prepared by diamond polishing to a 0.25 μm finish. For each processing condition, 10 bars were measured to calculate the reported averages and standard deviations. The corresponding elastic moduli were calculated from bar deflection data that were collected using a deflectometer during four-point flexure.

Thermal diffusivity was measured by the laser flash technique (Flashline 5000, Anter Corp, Pittsburg, PA) following the procedure defined in ASTM standard E1461.[32] Specimens were heated at 15°C/min up to 2000°C in flowing Ar that was maintained at a gauge pressure of ~41 kPa (6 psi). Each point was an average of three tests taken in two minutes after the specimen was held at a constant temperature for seven minutes. All specimens were heat treated at 2000°C for 1 hour in flowing Ar prior to measurement. Diffusivity values were calculated using the Clark and Taylor method, shown in equation

(1), where $t_{1/2}$ is the time to reach half the maximum temperature, L is the sample thickness, and c is a constant dependent on the shape of the temperature rise curve. Heat capacity was also measured by comparing the relative temperature rise of each specimen (M) to a graphite standard (R) using equation (2), where ρ is bulk density, C_p is heat capacity, L is thickness, and ΔT is the temperature rise.[33] Thermal conductivity (λ) was then calculated at each temperature from the measured thermal diffusivity (α), heat capacity (C_p), and bulk density (ρ), shown in equation (3).

$$\alpha = \frac{ct_{1/2}}{L^2} \tag{1}$$

$$\left(\rho C_p\right)_M = \frac{L_R \Delta T_R}{L_M \Delta T_M}\left(\rho C_p\right)_R \tag{2}$$

$$\lambda = \alpha \rho C_p \tag{3}$$

For microstructure analysis, billets were cross-sectioned and then polished to 0.25 μm using successively smaller diamond grit sizes. Scanning electron microscopy (Hitatchi S570, Tokyo, Japan) was used to characterize the microstructures. For grain size analysis, specimens were thermally etched at 1500°C for 15 minutes in flowing argon. Grain sizes were then measured from digital images using ImageJ software (National Institutes of Health, Bethesda, MD) by analyzing ~500 grains.

Results and Discussion

The onset of densification for HP ZrB_2 was found to be ≤1500°C for heating rates ≤20°C/min based on the initiation of ram travel after an external force was applied

(Figure 1(A)). Full density was reached at 1900°C for heating rates up to 80°C/min. In the case of the slowest heating rate, 5°C/min (HP5), full density was reached below 1800°C with a final density of 6.06 g/cm^3 (~98% relative density). The densification rate, calculated as a function of time (not shown), for HP5 during the intermediate stage of sintering was 0.6×10^{-2} sec^{-1}. Using faster heating rates, onset of densification was delayed to higher temperatures. For example, densification began ~1700°C for HP80, which reached a density of 6.00 g/cm^3 after 35 min at 1900°C. As heating rate increased, more time at 1900°C was required for densification. For instance, HP5 was held for 10 minutes at 1900°C, while HP80 required 35 minutes at 1900°C for ram travel to cease. The densification rates for HP50 and HP80 were both ~1.0×10^{-2} sec^{-1} during intermediate stage sintering. This showed that the increase in heating rate for HP specimens both delayed densification to higher temperatures, but increased the intermediate stage densification rate. However, the final density was independent of the heating rate during HP as all of the HP specimens reached about the same relative density.

ZrB_2 was densified by SPS at 1900°C using heating rates from 50°C/min to 300°C/min (Figure 1(B)). Similar to HP, SPS50 had an onset of densification around 1500°C after an external force was applied. The initial density was controlled by powder compaction and specimen preparation. Once densification began, however, no significant differences in ram travel were observed as a function of heating rate for SPS50, SPS100, or SPS300, in contrast to what had been observed for HP ZrB_2. Figure 1B shows that the majority of densification in SPS specimens occurred at 1900°C rather than during heating as it had for HP. Overall, the densification rates in SPS were higher than in HP. For instance, SPS50 had a densification rate of 1.3×10^{-2} sec^{-1} compared to

1.0×10^{-2} sec^{-1} for HP50. The faster heating rates in SPS, namely SPS100 and SPS300, had higher densification rates (1.7×10^{-2} sec^{-1}) compared to SPS 50 (1.3×10^{-2} sec^{-1}). Regardless of heating rate, the final density was the same for all SPS specimens, ~6.05 g/cm^3 or 98%, as shown in Table I.

Table I: Density and Grain Size for HP and SPS ZrB_2

Heating rate (°C/min)	Bulk density (g/cm^3)	Relative Density (%)	Porosity (%)	Grain size (μm)
HP5	6.06	97.9	0.8	2.8 ± 2.8
HP10	5.92	95.7	2.7	2.6 ± 1.6
HP20	5.79	93.5	4.3	3.0 ± 2.1
HP33	5.92	95.6	2.9	3.2 ± 2.1
HP40	5.89	95.2	3.3	3.3 ± 2.2
HP50	5.95	96.1	2.5	3.1 ± 2.0
HP80	6.02	97.3	1.4	3.8 ± 1.7
SPS50	6.04	97.6	1.1	2.1 ± 1.1
SPS80	5.89	95.2	3.2	2.0 ± 1.1
SPS100	6.04	97.6	1.0	2.1 ± 1.2
SPS200	6.06	98.2	0.8	2.1 ± 1.1
SPS300	6.06	97.9	0.8	2.0 ± 1.0

Scanning electron microscopy (SEM) was used to determine the average ZrB_2 grain sizes in after HP and SPS ceramics (Figure 2). One difference in the resulting microstructures, shown in Figure 2 and summarized in Table I, was that SPS ZrB_2 had a smaller final grain size for the materials densified using the same heating rate. For example, the average grain size was 2.1 μm for SPS50 compared to 3.1 μm for HP50. For HP, the average grain size increased as heating rate increased, increasing from 2.8 μm for HP5 to 3.8 μm for HP80. However, the standard deviation, which was taken as a measure of the uniformity of the grain size, decreased as heating rate increased for HP

ZrB_2. This was consistent with the delay in intermediate stage sintering for faster heating rates as previously reported by Guo et al.[24]

Unlike HP, changing the heating rate for SPS ZrB_2 did not change the average grain size or distribution, as all SPS heating rates produced an average grain size ~2.1 ± 1.1 μm. The microstructures for SPS ZrB_2 shown in Figure 2 had similar appearances due to the use of the same holding time (15 minutes) at 1900°C for each heating rate. The same hold time at the peak temperature, which was where the majority of densification occurred for SPS specimens, would then be expected to result in similar grain sizes. In HP, however, a significant amount of densification occurred below 1900°C, thereby leading to different hold times at 1900°C, which produced differences in grain size and grain size distribution.

Additional SEM analysis revealed the presence of ZrO_2 throughout the microstructure of HP80 (Figure 3). Comparatively, no ZrO_2 was observed in HP ZrB_2 with heating rates ≤20°C/min or in the SPS ZrB_2 specimens. This observation suggested that initial oxygen impurities in the ZrB_2 powder were removed for slower heating rates during HP and for all of the SPS specimens. However, for HP, the highest heating rates decreased the amount of time that specimens spent at intermediate temperatures and, therefore, also the time for reactions that removed oxides.[16,18] The observation of oxide inclusions was supported by x-ray diffraction analysis of HP and SPS specimens after densification. HP specimens with heating rates >20°C/min were found to have up to ~3.1 wt% tetragonal ZrO_2 (3.3 vol%). Based on the amount of ZrO_2 that was observed, the final oxygen content was calculated to be 0.8 wt% for HP80. Considering that the starting oxygen content of the attrition milled ZrB_2 was ~2.1 wt% O, the densification process (heating rates >20°C/min) removed ~1.3 wt% oxygen. In contrast, the oxygen contents were much lower (~0.05 wt%) for all of the SPS specimens and HP specimens with heating rates ≤20°C/min. Despite the use of faster heating rates (i.e., 50°C/min and higher), which reduced the time for removal of oxygen, the oxygen contents of the SPS specimens were lower due to the pre-treatment of powders to 1500°C prior to the SPS runs.

Mechanical Properties

The average strength of HP ZrB_2 increased with increasing heating rate, as shown in Figure 4. The maximum flexure strength increased from 480 MPa for HP5 to 612 MPa for HP50. The average strengths for intermediate heating rates fell between these two values. Although the average flexure strength was the highest for HP50 at 612 MPa, the flexure strength was 593 MPa for HP80, essentially the same considering the standard deviation (Table II). Figure 4 also shows that the standard deviations of the flexure strength decreased as heating rate increased for HP specimens. The standard deviations for the flexure strengths of HP5 and HP10 was ~70 MPa, but decreased to ~50 MPa for HP20 and HP50 and decreased further to ~20 MPa for HP80. The increase in flexure strength with heating rate appears to contradict the trend expected based on the average grain size, since average grain size increased with heating rate for HP ceramics (Table I). However, the standard deviation in grain size was smaller for faster heating rates, with a minimum value of 1.7 μm for HP80. Compared to the trend of average grain size, the maximum grain size decreased with faster heating rates, which presumably act as the strength-limiting flaws, and increased the flexure strength up to >600 MPa.

The flexure strength of HP ZrB_2 decreased as the maximum grain size increased (Figure 5). As an example, the largest grain size observed by SEM for HP5 was 10.6 μm and the average strength was 480 MPa. By comparison, HP80 had an average strength of 593 MPa and a maximum grain size of 8.8 μm. In the absence of other larger flaws, the largest grain size should act as the strength-limiting flaw, which implies that strength should scale with inverse square root of maximum grain size based on the Griffith relationship.[34] The maximum grain size was found to decrease with faster heating rates during HP (Table II). The relationship of flexure strength and grain size was consistent with the Griffith relationship, which was indicated on Figure 5 by the dotted line. Equation (4) was used to calculate the expected surface flaw size based on the Griffith criterion, where K_{1C} was the fracture toughness (assumed to be 3.5 MPa $m^{1/2}$ based on previous reports of similar materials[35]), σ was the flexure strength, and Y was a constant (1.98 for a surface flaw). Table II shows that there was strong agreement between largest flaw size observed and the calculated critical flaw size for HP ZrB_2 regardless of the heating rate. The difference between the calculated and measured maximum grain sizes for each heating rate is likely due to the fact that the measured maximum grain size was only the largest found during grain size analysis rather than the actual maximum flaw size contributing to failure. Likewise, Figure 5 shows the maximum grain size was consistent with the critical flaw for HP ZrB_2.

$$c = \left(\frac{K_{1C}}{Y\sigma}\right)^2 \tag{4}$$

Table II: Mechanical Properties of HP and SPS ZrB_2 with Varying Heating Rates

Heating rate (°C/min)	Flexure strength (MPa)	Elastic modulus (GPa)	Max grain size (μm)	Calc flaw size (μm)
HP5	480 ± 65	500 ± 6	10.6	13.6
HP10	505 ± 77	521 ± 23	11.2	12.2
HP20	461 ± 53	514 ± 17	12.7	14.6
HP33	561 ± 64	529 ± 20	9.7	9.9
HP40	555 ±55	532 ± 14	9.9	10.1
HP50	612 ± 53	543 ± 17	8.1	8.3
HP80	593 ± 20	520 ± 35	8.8	8.9
SPS50	400 ± 45	467 ± 30	6.2	19.5
SPS80	393 ± 53	430 ± 30	7.0	20.3
SPS100	405 ± 40	460 ± 60	6.6	19.1
SPS200	473 ± 82	482 ± 50	6.0	14.0

The flexure strengths of SPS ZrB_2 ceramics were lower than those of HP ZrB_2, regardless of heating rate. For SPS50, the flexure strength was ~400 MPa for SPS ZrB_2 compared to ~600 MPa for HP50. Unlike HP ZrB_2, the average strength of SPS ZrB_2 did not change significantly as a function of heating rate. Regardless of heating rate, the average flexure strength for the SPS ZrB_2 was 430 ± 40 MPa (Table II). The smaller variation in flexure strength was expected for SPS ZrB_2 based on microstructure analysis, which revealed that neither the average grain size nor the standard deviation varied with heating rate. For each SPS ceramic, the average grain size was 2.0 ± 0.1 μm, while the maximum grain size was 6.3 ± 0.3 μm. Using Equation (4) and the average flexure strength of SPS ZrB_2 of ~430 MPa, the calculated flaw size would be 16.9 μm, which is significantly larger than the measured maximum grain size for SPS ZrB_2 (~6.6 μm). For the same heating rate in HP, the flaw size was calculated to be 8.3 μm (612 MPa flexure strength), which agreed well with the largest measured grain size. The difference between the HP and SPS results suggested that something other than maximum grain size was controlling the strength of SPS ZrB_2.

The decreased flexure strength of SPS ZrB_2 may be due to residual stresses that resulted from the high cooling rates (>100°C/min) employed in SPS. If residual stresses were present and were of sufficient magnitude, then they could produce microcracks in the resulting ceramics. Examination of polished cross sections of SPS ZrB_2 ceramics (Figure 6) revealed that microcracking was present in SPS ZrB_2. Microcracks not only affected the flexure strength, but also resulted in a decrease in the elastic modulus of the SPS ceramics (Table II). For example, the elastic modulus of SPS ZrB_2 was <485 MPa for all heating rates compared to values >500 MPa for all of the HP ZrB_2 ceramics. The lower flexure strengths and decreased elastic moduli of SPS ZrB_2 ceramics are therefore a direct result of the presence of microcracking.

Thermal Properties

The heat capacity values measured for HP and SPS ZrB_2 ceramics were similar to handbook values (Figure 7). For all heating rates and both processing methods, the heat capacity increased from ~54 J/mol•K at 400°C to ~65 J/mol•K at 600°C. Above 600°C, the heat capacity increased linearly up to a maximum value of 84 J/mol•K at 2000°C. The heat capacity reported in the NIST JANAF tables, which was measured by copper-block drop calorimetry up to 1200°C and then an arc-imaging technique to >2000°C,[36] is indicated by a solid line in Figure 7. At any temperature, the difference between reported heat capacity and that measured by the laser flash method measured in this study was less than 10%. Not only were the heat capacity values measured in this study consistent with the accepted values, but the measurements also showed that the values were not affected by the processing conditions, microstructures, or the presence of microcracks. Therefore, the NIST-JANAF values were used for all subsequent calculations.

Thermal diffusivity of both HP and SPS ZrB_2 decreased with increasing temperature (Figure 8). A maximum value of 0.170 cm^2/sec was measured for HP10 at 200°C, which decreased to 0.144 cm^2/sec at 2000°C. For HP heating rates >20°C/min, thermal diffusivity values decreased compared to specimens produced using lower heating rates. For example, HP80 had a maximum thermal diffusivity of 0.145 cm^2/sec at 200°C compared to values of more than 0.165 cm^2/sec for specimens produced with HP heating rates ≤20°C/min. At 2000°C, the thermal diffusivity of HP80 decreased to 0.131 cm^2/sec, which that was ~10% (0.01 cm^2/sec) less than that of the lower heating rates.

The values of thermal diffusivity for SPS ZrB_2 did not change significantly as a function of heating rate (Figure 8(B)), with values of 0.16-0.17 cm^2/sec at 200°C and decreasing to 0.14-0.15 cm^2/sec at 2000°C. As noted earlier, the thermal diffusivity of HP ZrB_2 decreased with heating rates >20°C/min, however the thermal diffusivity of SPS ZrB_2 did not change as a function of heating rate.

Thermal conductivity values were calculated using measured thermal diffusivities and heat capacities from the NIST-JANAF data. For HP ZrB_2, thermal conductivity increased with increasing temperature (Figure 9(A)). As an example, for ceramics produced with HP heating rates ≤20°C/min thermal conductivity increased from 29 W/m•K at 200°C to 62 W/m•K at 2000°C. With heat capacity not markedly affected by compositional or microstructural changes, the thermal conductivities for HP ZrB_2, as a function of heating rate, followed the same trends as thermal diffusivity values with heating rates ≤20°C/min producing lower values. When the heating rate was >20°C/min, the thermal conductivity decreased as heating rate increased. As an example, the thermal conductivity was 27 W/m•K for HP50 at 200°C, but decreased to 25 W/m•K for HP80 at 200°C. At 2000°C, the thermal conductivity of HP50 was 59 W/m•K and decreased to 56 W/m•K for HP80, which showed that the incremental decrease in thermal conductivity was observed over the entire temperature range, 200°C to 2000°C.

Unlike HP ZrB_2, the thermal conductivities of SPS ZrB_2 were about the same for all heating rates (Figure 9B). The thermal conductivity of SPS ZrB_2 increased from a minimum value of 26 W/m•K at 200°C to 60 W/m•K at 2000°C for SPS300. These values did not change significantly with heating rate as the values for SPS50 increased from 28 W/m•K at 200°C to 64 W/m•K at 2000°C. The thermal conductivity of SPS ZrB_2 with heating rates between 50°C/min and 300°C/min fell between the extremes of the investigation, but did not show a discernable trend as compared to HP ZrB_2. The values of SPS ZrB_2 were similar to those of HP ZrB_2 with heating rates ≤20°C/min.

Previous work by Smith et al.[37] related the thermal conductivity of Al_2O_3 to average grain size. This analysis was later modified by Zimmermann et al.[28] to model the effect of grain size on the phonon contribution to thermal conductivity of ZrB_2 (Equation 5). The analysis assumed that the electrical conductivity as a function of temperature determined by Zimmermann et al was the same for HP and SPS ZrB_2.[28] The electron contribution to thermal conductivity was then calculated using the Wiedemann-Franz law (Equation 6), and the resulting relationship of electron contribution and temperature is shown below as Equation 7. The phonon contribution for specimens in this study was estimated by subtracting the electron contribution from the total thermal conductivity. The effect of grain size was estimated to change the phonon contribution by decreasing the mean free path of phonons with smaller grain sizes. In these equations, T is absolute temperature, σ_e is the electrical conductivity, and d is average grain size. Figure 10A shows the total thermal conductivity of ZrB_2 as a function of grain size and temperature. Lines have been drawn to show the predicted thermal conductivity based on average grain size, which is the sum of the electron (λ_e) and phonon (λ_p) contributions (Equations (5) and (7), respectively).[28] An example of the electron and phonon contributions as a function of temperature for HP5 is shown in Figure 10(B). For SPS ZrB_2 materials and for HP ZrB_2 prepared using heating rates ≤20°C/min, the calculated thermal conductivities were similar to values predicted from the average grain size. The values for SPS80 and HP5 are shown as representative of these conditions. In contrast, the thermal conductivity of HP ZrB_2 with heating rates >20°C/min fell below the values predicted using the grain size model. For these materials, the thermal conductivity decreased as the average grain size increased. This result was not expected, as larger grain sizes should reduce phonon scattering and therefore increasing thermal conductivity.

$$\frac{1}{\lambda_p} = 2.18\times10^{-5}T + \frac{2\times10^{-7}}{d} \tag{5}$$

$$\lambda_e = 2.44\times10^{-8}\sigma_e T \tag{6}$$

$$\lambda_e = \frac{2.45T}{0.0401T+10.798} \tag{7}$$

Unlike all of the SPS materials, or HP ceramics produced using heating rates of <20°C/min, the higher heating rates in HP led to the formation of ZrO_2 inclusions in the

ZrB_2 ceramics. For example, 3.3 vol% ZrO_2 was found in HP80 based on image analysis. Using a dispersed phase model in Equation (8), and assuming thermal conductivities of 1 W/m•K for tetragonal ZrO_2[38] and 62 W/m•K for ZrB_2 at 2000°C, the calculated thermal conductivity of HP80 was 58 W/m•K at 2000°C. This value compared favorably to the measured value of 56 W/m•K at 2000°C. This shows that the rapid heating rate used during HP forced oxides to remain in the microstructure, which formed ZrO_2. The presence of the lower thermal conductivity ZrO_2 inclusions decreased the thermal conductivity of the resulting ceramics.

$$\lambda = \lambda_c \left(\frac{1+2v_d\left(1-{\lambda_c}/{\lambda_d}\right)/\left({2\lambda_c}/{\lambda_d}+1\right)}{1-v_d\left(1-{\lambda_c}/{\lambda_d}\right)/\left({\lambda_c}/{\lambda_d}+1\right)} \right) \qquad (8)$$

Conclusion

ZrB_2 was densified by HP and SPS using heating rates ranging from 5°C/min to 300°C/min. The average grain size for HP ZrB_2 increased as heating rate increased from 2.8 μm for HP5°C/min to 3.8 μm for HP80 because more time was required at 1900°C for densification that led to coarsening of ZrB_2 grains. In contrast, the maximum grain size observed in HP ZrB_2 decreased with increased heating rate from 10.6 μm for HP5 to 8.8 μm for HP80. For SPS ZrB_2, both the average and maximum grain sizes were constant at ~2.1 μm and ~6.5 μm, respectively, regardless of the heating rate. The flexure strength of HP material was proportional to the inverse square root of maximum grain size, which is consistent with predictions from the Griffith criteria. Based on the Griffith relationship, SPS ZrB_2 had a critical flaw size of ~19 μm, which was much larger than the maximum grain size of 6.3 μm. The discrepancy between the calculated flaw size and the measured maximum grain size indicated that some larger flaw controlled the strength of SPS ZrB_2. Analysis by SEM along with measurement of elastic moduli confirmed the presence of microcracks that decreased the flexure strength of SPS ZrB_2 ceramics. The microcracks could have resulted from the cooling rates (~100°C/min) utilized in SPS. Without microcracking, the maximum grain size of SPS specimens was ~6 μm, which would correspond to a flexure strength of ~700 MPa in the absence of other, larger strength-limiting flaws.

The heat capacity values for HP and SPS ZrB_2 ceramics were independent of heating rate and densification method. In addition, the values were comparable to those from the NIST JANAF tables. The thermal diffusivity decreased from 0.165 cm^2/sec at 200°C to 0.14 cm^2/sec at 2000°C for SPS ZrB_2. In HP ZrB_2, the thermal diffusivity decreased with higher heating rates, to a minimum value of 0.146 cm^2/sec at 200°C. The thermal conductivity of HP ZrB_2 decreased with heating rates >20°C/min, below which no differences were present. This behavior followed a trend that was consistent with predictions made using the average grain size. For HP ZrB_2 produced with heating rates ≤20°C/min, the value of thermal conductivity could be predicted to be >60 W/m•K using the average grain size, as had been reported by previous researchers. However, the values predicted from grain size did not agree with measured values when heating rates were >20°C/min. For heating rates >20°C/min in HP, SEM analysis revealed that up to 3.3 vol% ZrO_2 (HP80) was present in the dense ceramics. The presence of this low thermal conductivity phase decreased the thermal conductivity compared to HP ZrB_2 produced using heating rates ≤20°C/min or SPS ZrB_2, which were free of ZrO_2

inclusions. Overall, using higher heating rates increased strength, but decreased the thermal conductivity. Based on the information generated in this investigation, a heating rate between 20°C/min and 50°C/min during hot pressing may optimize both the mechanical strength and thermal conductivity of ZrB_2. The results show that it is possible to achieve a flexural strength of 550 MPa with a thermal conductivity of 60 W/m•K for ZrB_2 at 2000°C.

Acknowledgements

The authors would like to acknowledge Dr. Michael Cinibulk and Dr. Carmen Carney at Wright Patterson Air Force Base in Dayton, OH for their assistance with the use of the FCT-SPS unit as well as technical discussions related to SPS processing and heating rate effects. The AMCL should also be acknowledged for use of SEM and XRD.

References

1. R.A. Cutler, "Engineering Properties of Borides," pp. 787-803 in Vol. 4, *Ceramics and Glasses: Engineered Materials Handbook.* Edited by S. J. S. Jr. ASM International, Materials Park, OH, 1991.

2. X. Zhang, X. Luo, J. Han, J. Li, and W. Han, "Electronic structure, elasticity and hardness of diborides of zirconium and hafnium: First principles calculations," *Computational Materials Science,* **44** [2] 411-21 (2008).

3. L.S. Sigl R. Telle, and K. Takagi, "Boride-Based Hard Materials," pp. 802-945 in *Handbook of Ceramic Hard Materials.* Edited by R. Riedel. Wiley-VCH, Weinheim, Germany, 2000.

4. D.E. Wiley, W.R. Manning, and O. Hunter Jr, "Elastic properties of polycrystalline TiB_2, ZrB_2 and HfB_2 from room temperature to 1300K," *Journal of the Less Common Metals,* **18** [2] 149-57 (1969).

5. O. Kida, "Monolithic Refractory Material and Waste Melting Furnace Using the Same," Japanese Patent JP2000335969, May 12, 2000.

6. M.M. Opeka, I.G. Talmy, E.J. Wuchina, J.A. Zaykoski, and S.J. Causey, "Mechanical, Thermal, and Oxidation Properties of Refractory Hafnium and zirconium Compounds," *Journal of the European Ceramic Society,* **19** 2405-14 (1999).

7. R.P. Tye and E.V. Clougherty, "The Thermal and Electrical Conductivities of some Electrically Conducting Compounds," *Proceedings of the Fifth Symposium on Thermophysical Properties,* 396-401 (1970).

8. H.J. Juretschke and R. Steinitz, "Hall Effect and Electrical Conductivity of Transition-Metal Diborides," *Journal of Physics and Chemistry of Solids,* **4** [1-2] 118-27 (1957).

9. M.M. Opeka, I.G. Talmy, and J.A. Zaykoski, "Oxidation-based materials selection for 2000C + hypersonic aerosurfaces: Theoretical considerations and historical experience: Special Section: Ultra-High Temperature Ceramics (Guest Editors: Joan Fuller and Michael D. Sacks)," *Journal of Materials Science,* **39** 5887-904 (2004).

10. A. Rezaie, W.G. Fahrenholtz, and G.E. Hilmas, "Effect of hot pressing time and temperature on the microstructure and mechanical properties of ZrB_2–SiC," *Journal of Materials Science,* **42** [8] 2735-44 (2007).

11. W. G. Fahrenholtz, G. E. Hilmas, I. G. Talmy, and J. A. Zaykoski, "Refractory Diborides of Zirconium and Hafnium," *Journal of the American Ceramic Society,* **90** [5] 1347-64 (2007).

12. D. Kalish and E. V. Clougherty, "Densification Mechanisms in High-pressure Hot-Pressing of HfB_2," *Journal of the American Ceramic Society,* **52** [1] 26-30 (1969).

13. A. Rezaie, W.G. Fahrenholtz, and G.E. Hilmas, "Effect of hot pressing time and temperature on the microstructure and mechanical properties of ZrB_2-SiC," *Journal of Materials Science,* **42** [8] 2735-44 (2007).

14. M. Thompson, W.G. Fahrenholtz, and G. Hilmas, "Effect of Starting Particle Size and Oxygen Content on Densification of ZrB_2," *Journal of the American Ceramic Society,* **94** [2] 429-35 (2011).

15. S. Baik and P.F. Becher, "Effect of Oxygen Contamination on Densification of TiB2," *Journal of the American Ceramic Society,* **70** [8] 527-30 (1987).

16. S. Zhu, W.G. Fahrenholtz, G.E. Hilmas, and S.C. Zhang, "Pressureless sintering of carbon-coated zirconium diboride powders," *Materials Science and Engineering: A,* **459** [1-2] 167-71 (2007).

17. S. C. Zhang, G. E. Hilmas, and W. G. Fahrenholtz, "Pressureless Densification of Zirconium Diboride with Boron Carbide Additions," *Journal of the American Ceramic Society,* **89** [5] 1544-50 (2006).

18. W. G. Fahrenholtz, G. E. Hilmas, S. C. Zhang, and S. Zhu, "Pressureless Sintering of Zirconium Diboride: Particle Size and Additive Effects," *Journal of the American Ceramic Society,* **91** [5] 1398-404 (2008).

19. S.-Q. Guo, Y. Kagawa, T. Nishimura, D. Chung, and J.-M. Yang, "Mechanical and physical behavior of spark plasma sintered ZrC-ZrB2-SiC composites," *Journal of the European Ceramic Society,* **28** [6] 1279-85 (2008).

20. N. Kaur, R. Mohan, N.K. Gaur, and R.K. Singh, "Cohesive and thermal properties of transition metal diborides," *Physica B: Condensed Matter,* **404** [8-11] 1607-10 (2009).

21. S.C. Zhang, G.E. Hilmas, and W.G. Fahrenholtz, "Oxidation of Zirconium Diboride with Tungsten Carbide Additions," *Journal of the American Ceramic Society,* **94** [4] 1198-205 (2011).

22. L.M. Clark and R.E. Taylor, "Radiation loss in the flash method for thermal diffusivity," *Journal of Applied Physics,* **46** [2] 714-9 (1975).

23. L. Solymar and D. Walsh, *Electrical Properties of Materials,* 7 ed. Oxford University Press Inc., New York, 2004.

24. J. Zou, S.-K. Sun, G.-J. Zhang, Y.-M. Kan, P.-L. Wang, and T. Ohji, "Chemical Reactions, Anisotropic Grain Growth and Sintering Mechanisms of Self-Reinforced ZrB_2–SiC Doped with WC," *Journal of the American Ceramic Society,* **94** [5] 1575-83 (2011).

25. W.-B. Tian, Y.-M. Kan, G.-J. Zhang, and P.-L. Wang, "Effect of carbon nanotubes on the properties of ZrB_2-SiC ceramics," *Materials Science and Engineering: A,* **487** [1-2] 568-73 (2008).

26. S. Guo, Y. Kagawa, T. Nishimura, and H. Tanaka, "Thermal and Electric Properties in Hot-Pressed ZrB_2-$MoSi_2$-SiC Composites," *Journal of the American Ceramic Society,* **90** [7] 2255-8 (2007).

27. M. Gasch, S. Johnson, and J. Marschall, "Thermal Conductivity Characterization of Hafnium Diboride-Based Ultra-High-Temperature Ceramics," *Journal of the American Ceramic Society,* **91** [5] 1423-32 (2008).

28. J.W. Zimmermann, G.E. Hilmas, W.G. Fahrenholtz, R.B. Dinwiddie, W.D. Porter, and H. Wang, "Thermophysical Properties of ZrB_2 and ZrB_2-30SiC Ceramics," *Journal of the American Ceramic Society,* **91** [5] 1405-11 (2008).

29. G.V. Samsonov, B.A. Kovenskaya, and T.I. Serebryakova, "Some physical characteristics of the diborides of transition metals of groups IV and V," *Russian Physics Journal,* **14** [1] 11-4 (1971).

30. L. Zhang, D.A. Pejaković, J. Marschall, and M. Gasch, "Thermal and Electrical Transport Properties of Spark Plasma-Sintered HfB_2 and ZrB_2 Ceramics," *Journal of the American Ceramic Society,* **94** [8] 2562-70 (2011).

31. R.G. Munro, "Material Properties of Titanium Diboride," *Journal of Research of the National Institute of Standards and Technology,* **105** 709-20 (2000).

32. ASTME1461, "Standard Test Method for Thermal Diffusivity of Solids by the Flash Method," *ASTM International,* (2001).

33. K. Shinzato and T. Baba, "A Laser Flash Apparatus for Thermal Diffusivity and Specific Heat Capacity Measurements," *Journal of Thermal Analysis and Calorimetry,* **64** [1] 413-22 (2001).

34. J.B. Wachtman, *Mechanical Properties of Ceramics*. John Wiley and Sons, Inc., New York, 1996.

35. A.L. Chamberlain, W.G. Fahrenholtz, G.E. Hilmas, and D.T. Ellerby, "High-Strength Zirconium Diboride-Based Ceramics," *Journal of the American Ceramic Society,* **87** [6] 1170-2 (2004).

36. M.W. Chase, *NIST-JANAF Thermochemical Tables*. American Chemical Society and the American Institute of Physics, Woodbury, NY, 1998.

37. D.S. Smith, S. Fayette, S. Grandjean, C. Martin, R. Telle, and T. Tonnessen, "Thermal Resistance of Grain Boundaries in Alumina Ceramics and Refractories," *Journal of the American Ceramic Society,* **86** [1] 105-11 (2003).

38. D.P.H. Hasselman, L.F. Johnson, L.D. Bentsen, R. Syed, and H.L. Lee, "Thermal Diffusivity and Conductivity of Dense Polycrystalline ZrO_2 Ceramics: A Survey," *Am. Ceram. Soc. Bull.,* **66** [5] 799-806 (1987).

FIGURES

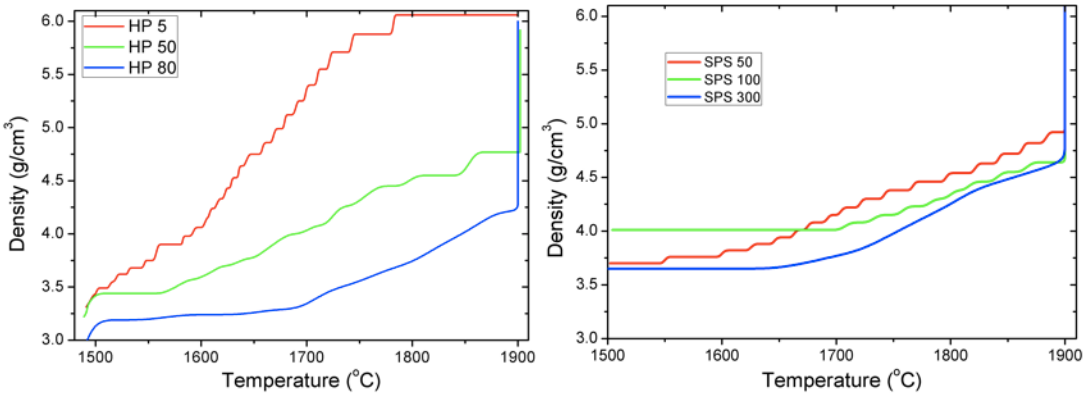

(A) (B)

Figure 1: Bulk density as a function of temperature during hot pressing (A) and spark plasma sintering (B) of ZrB_2.

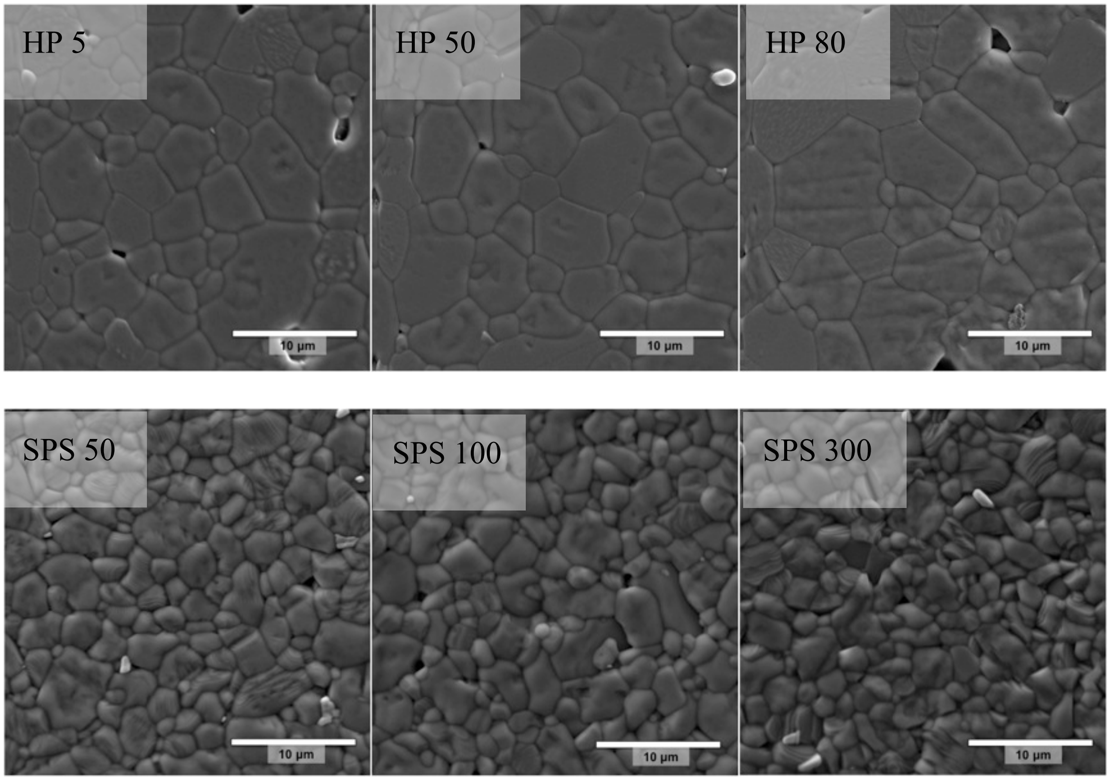

Figure 2: Polished and thermally etched cross sections of HP and SPS ZrB_2.

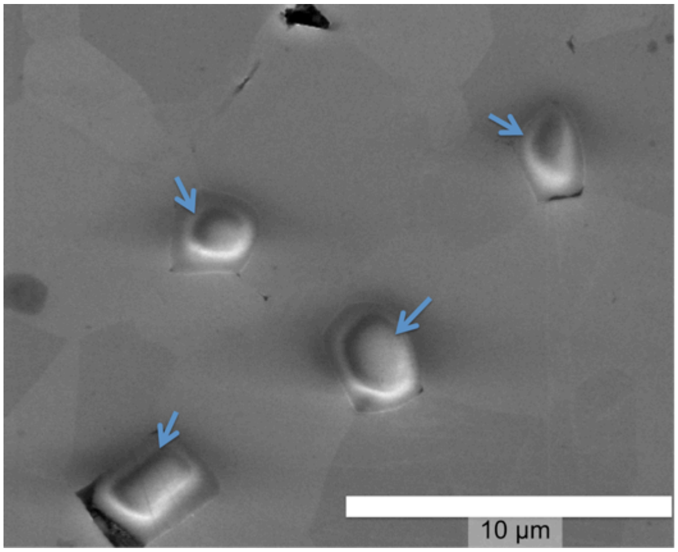

Figure 3: Polished SEM image of HP80. The arrows indicate ZrO_2 grains (3.3 vol% ZrO_2) confirmed by XRD (not shown).

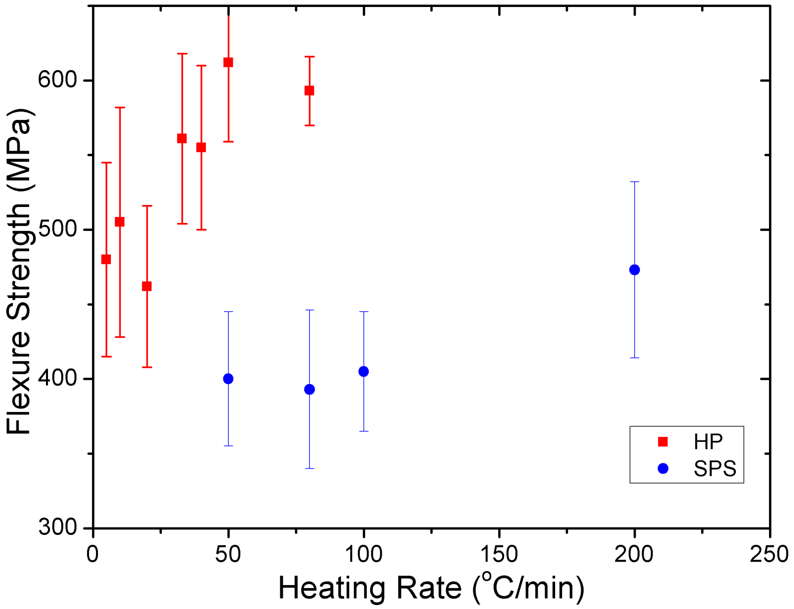

Figure 4: Four-point flexure strength as a function of heating rate for HP and SPS ZrB_2.

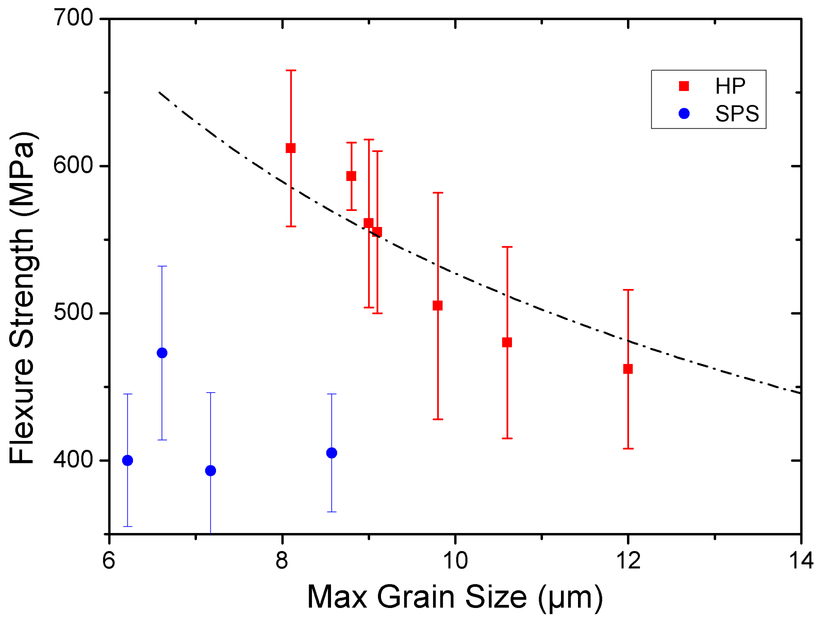

Figure 5: Four-point flexure strength as a function of maximum grain size for HP and SPS ZrB_2 ceramics. A dashed line is shown for the expected flexure strength based on the Griffith criteria for surface flaws and assuming a fracture toughness of 3.5 MPa•m$^{-1/2}$.

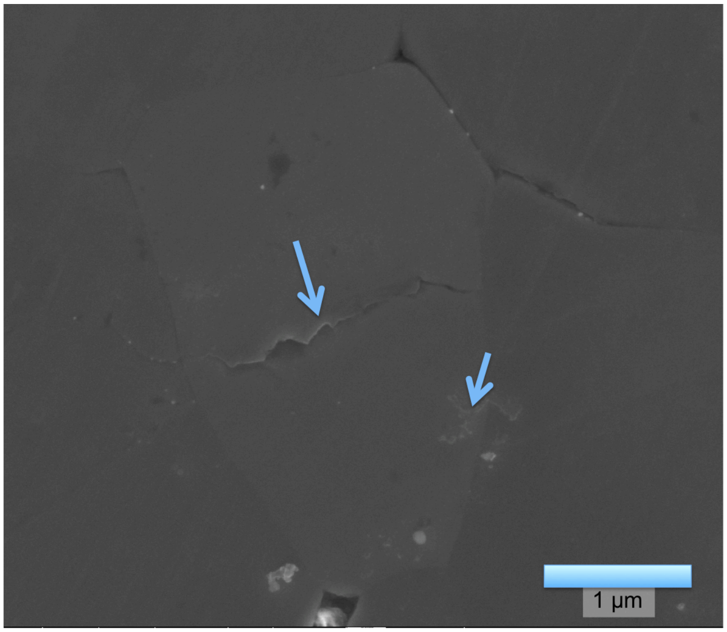

Figure 6: SEM image of a polished cross-section of SPS ZrB_2 (SPS80) with arrows indicating microcracks.

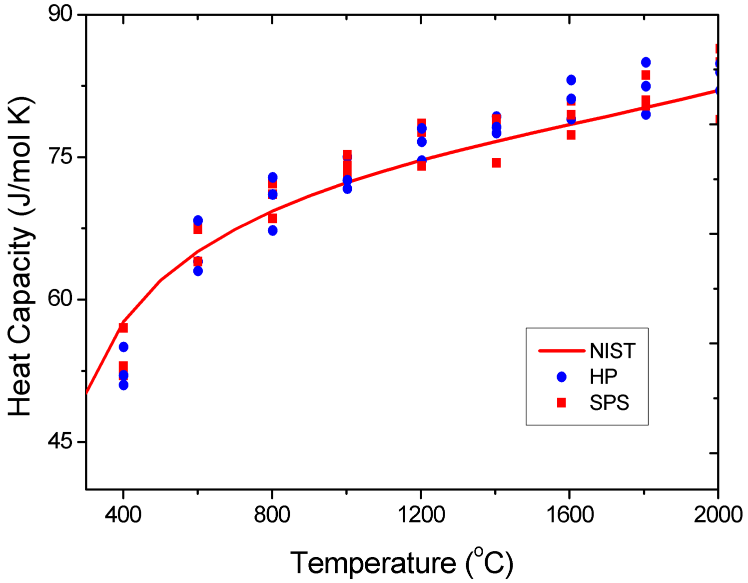

Figure 7: Heat capacity as a function of temperature for HP and SPS ZrB_2 ceramics processed with different heating rates. A line was added to show values calculated from data in the NIST JANAF tables.

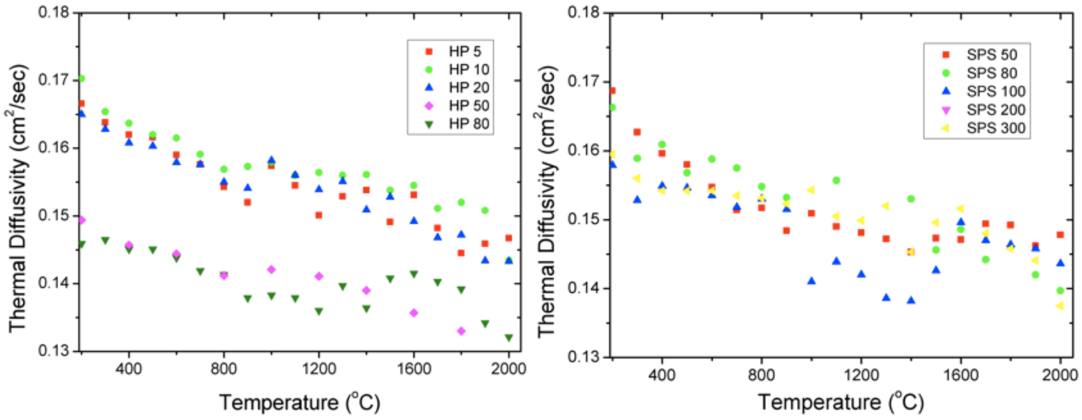

(A) (B)

Figure 8: Thermal diffusivity as a function of temperature for HP (A) and SPS ZrB_2 (B) processed with different heating rates.

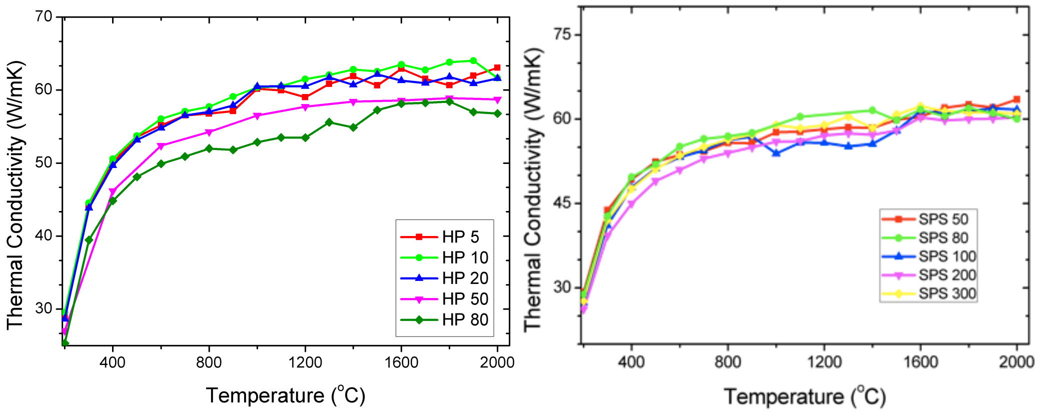

(A) (B)

Figure 9: Thermal conductivity as a function of temperature for (A) HP and (B) SPS ZrB_2. Lines are shown too guide eye for each specimen.

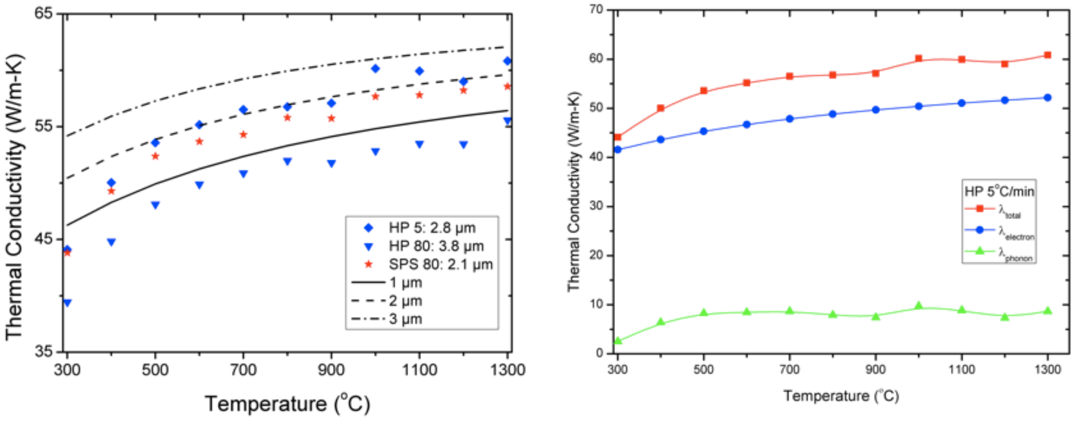

(A) (B)

Figure 10: Thermal conductivity as a function of the average ZrB_2 grain size (A) and the combination of electron and phonon contributions to the thermal conductivity of HP5 (B).

4. THERMAL PROPERTIES OF ZRB_2-TIB_2 SOLID SOLUTIONS

Matthew Thompson*; William G. Fahrenholtz; Greg E. Hilmas;
Dept. of Materials Science and Engineering
Missouri University of Science and Technology, Rolla, MO 65401

Abstract

Zirconium diboride ceramics were prepared with additions of up to 50 vol% TiB_2. The resulting $(Zr,Ti)B_2$ ceramics formed solid solutions, which was confirmed by x-ray diffraction analysis. Scanning electron microscopy showed that the addition of TiB_2 resulted in the grain size decreasing from 22 μm for nominally pure ZrB_2 to 7 μm for ZrB_2 containing 50 vol% TiB_2. The thermal conductivity at 25°C ranged from 93 W/m•K for nominally pure ZrB_2 to 58W/m•K for ZrB_2 containing 50 vol% TiB_2. Thermal conductivity was as high as 67 W/m•K for nominally pure ZrB_2 at 2000°C, but dropped to 59 W/m•K with the addition of 50 vol% TiB_2. Electrical resistivity measurements used to calculate the electron contribution to thermal conductivity, which was 76 W/m•K for nominally pure ZrB_2, but decreased to 57 W/m•K when 50 vol% TiB_2 was added. The phonon contribution to thermal conductivity did not change significantly for TiB_2 additions of 10 vol% or less. For larger additions of TiB_2, however, the phonon contribution decreased to nearly zero for all temperatures. Models were used to show that electrons and phonons between TiB_2 and ZrB_2 interacted, which decreased the thermal conductivity.

Introduction

Zirconium diboride (ZrB_2) belongs to a class of materials known as ultrahigh temperature ceramics (UHTCs) due to its melting temperature, which is in excess of 3000°C.[1] In addition to high melting temperatures, UHTCs also boast high elastic moduli (>500 GPa)[1-3] and good chemical inertness,[4] which make them excellent candidates for refractory linings, cutting tools, and molten metal crucibles.[1,4,5] In addition to these properties, metal diborides, including ZrB_2, have high thermal (>95 W/m•K at 25°C)[6-8] and electrical (~10^7 S/m)[8,9] conductivities. The high thermal and electrical conductivities of metal diborides make them candidates for high temperature electrodes and thermal protection systems for hypersonic aerospace vehicles.[10]

ZrB_2, as with other metal diborides, has strong covalent bonding and low self-diffusion coefficients, which requires temperatures >1900°C and/or external pressure to achieve full density.[11-13] Hot pressing has typically been used to densify ZrB_2.[11-15] While ZrB_2 has been shown to densify without the addition of sintering additives, researchers commonly use carbon, B_4C, WC, SiC, or $MoSi_2$ to improve densification.[14,16-21] These additives have been used to react with and remove oxygen impurities from the surfaces of ZrB_2 particles prior to densification, which reduces the onset temperature for densification and decreases the effects of grain coarsening.[20,22,23] After densification, these additives can be incorporated into the microstructure in a variety of ways including as solid solutions,[21] isolated particles,[17,18] or grain boundary phases.[24] The mechanical properties of ZrB_2 with these additional phases have been reported by a number of researchers.[14,15,18] For example, the addition of SiC increased the strength from 565 MPa for nominally pure ZrB_2 to >1 GPa for ZrB_2 containing 30 vol% SiC.[14] Similarly, the addition of $MoSi_2$ has also been reported to increase strength.[18]

High thermal conductivity is an important design parameter for leading edges of proposed future hypersonic aerospace vehicles.[25] The ability of candidate leading edge materials, such as ZrB_2, to conduct heat depends on thermal conductivity. Higher values of thermal conductivity allow more heat to be conducted away from the sharp point of the leading edge where it is generated.[10,15,26] The thermal conductivity of metal diborides has been reported by a number of researchers.[6,7,27-29] In general, the thermal conductivities of different metal diborides have similar values and behavior as a function of temperature.[8] For example, the room temperature thermal conductivity of TiB_2 was reported to be 96 W/m•K compared to 95 W/m•K for ZrB_2 at room temperature.[8,30] However, the reported values also vary widely for individual materials, with values for HfB_2-based ceramics ranging from as low as about 40 W/m•K to above 120 W/m•K.[6] The differences in thermal conductivity were not explained in the papers, but were likely due to variations in processing technique, impurities, and grain sizes.[7,29] For nominally pure ZrB_2 ceramics, values of thermal conductivity at 25°C have been reported to be as low as 38 W/m•K to as high as 95 W/m•K.[31,32] Based on the results of these studies, it appears that the thermal conductivities are higher for materials with larger grain sizes and higher purities.

To better understand the thermal conductivity of electrically conductive materials such as diborides, researchers have separated thermal conductivity into electron and phonon contributions.[28,29,31] As an example, Tye and Clougherty reported the electron component of thermal conductivity to be as high as 75 W/m•K and a phonon component of 25 W/m•K at 25°C for ZrB_2.[29] Similarly, other researchers have shown that the electron component was responsible for at least 90% of the thermal conductivity of diborides, especially at temperatures greater than 1000°C.[8,31] Differences in processing techniques, impurities, and microstructure affect both the electron and phonon components of thermal conductivity below 1000°C.[7,31,33] For example, Zhang et al. reported that $HfB_{2.1}$ had a higher thermal conductivity (125 W/m•K) than $HfB_{1.9}$ (103 W/m•K) at 25°C, which showed that boron stoichiometry affected both the electron and phonon contribution to thermal conductivity in HfB_2.[8] However, only a limited number of studies have characterized the electron contribution to thermal conductivity for metal diborides.[28,29] One study focused on the effect of solid solutions on electrical properties, Juretschke et al. found that additions of group 4 diborides (i.e., Ti, Zr, and Hf) to group 5 diborides (i.e., V, Nb, and Ta) decreased the electrical conductivity compared to either of the end members.[9]

The purpose of this investigation was to study the effect of solid solution additions on the thermal conductivity of ZrB_2 ceramics.

Procedure

Commercially available ZrB_2 (Grade B, H. C. Starck, Goslar, Germany) and TiB_2 (Grade HCT-F, Momentive, Columbus, OH) powders were used for this study. The powders were ball milled in hexane for one hour using ZrB_2 milling media in a high-density polyethylene bottle to mix powders followed by rotary evaporation to remove the solvent. The mass of the ZrB_2 milling media was measured before and after milling, which indicated that ~0.2 wt% ZrB_2 was incorporated into the ZrB_2-TiB_2 powders due to wear of the media. After rotary evaporation, the powders were passed through a 50-mesh sieve.

Densification was accomplished by hot pressing using a 1-inch diameter circular graphite die in a resistively heated graphite element hot press (Thermal Technology Inc., Model HP20-3060-20, Santa Rosa, CA). The graphite die was lined with graphite paper and coated with boron nitride (Cerac, SP-108, Milwaukee, WI) to minimize reaction between the die and the ZrB_2-TiB_2 powders. Specimens were heated at 40°C/min. Below 1500°C, specimens were heated in a mild vacuum (~20 Pa). Isothermal holds of 1 hour were used at 1300°C and 1500°C during heating to allow for potential evaporation and/or reactions involving surface oxides (B_2O_3 and ZrO_2). After the hold at 1500°C, the atmosphere was changed to flowing Ar gas at standard pressure (~10^5 Pa) and a uniaxial pressure of 32 MPa was applied to the specimen. When the specimens reached 2100°C, the furnace was held at that temperature until ram travel had stopped for 20 minutes. The furnace was then allowed to cool at 40°C/min. The external pressure was released below 1500°C.

Hot pressed specimens were surface ground and cut (Chevalier, FSG-3A818, Santa Fe Springs, CA) into squares approximately 12.5 mm by 12.5 mm by 3.0 mm thick. The outer portions of the billets were ground or cut away to remove the portion of the pellet that may have been affected by reaction with the hot press die. The bulk density of each specimen was measured by Archimedes' technique (ASTM standard C373) using vacuum infiltration with distilled water as the immersing medium.[34]

Specimens were polished using successively finer diamond abrasives with a final abrasive size of 0.25 μm. Scanning electron microscopy (SEM; Hitachi S570, Japan) was used to characterize microstructure. Grain sizes were measured from SEM micrographs using image analysis software (ImageJ, National Institutes of Health, Bethesda, MD) by analyzing ~500 grains. X-ray powder diffraction (Philips X-Pert Pro diffractometer, Westborough, MA) analysis was used to identify phases present. Rietveld refinement (RIQAS, Materials Data Inc., Livermore, CA) of XRD patterns was used to determine lattice parameters of ZrB_2-TiB_2 specimens. Diffraction was accomplished using $Cu_{k\alpha}$ radiation (1.5409 Å) and scanning from 5° to 90° 2θ using a step size of 2.63 degrees and a counting time of 138 seconds.

Thermal diffusivity was measured by the laser flash technique (Flashline 5000, Anter Corp, Pittsburgh, PA) following the procedure defined in ASTM standard E1461.[35] Specimens were coated with graphite (Dry Graphite Lube, Diversified Brands, Cleveland, OH) and then analyzed up to 2000°C in flowing Ar that was maintained at a gauge pressure of ~41 kPa. Specimens were heated at 15°C/min. Each data point was an average of 3 tests taken every 2 minutes after the specimen had been held at a constant temperature for 7 minutes. Results were calculated using the Clark and Taylor method for determining thermal diffusivity (Equation 1).[36] In this calculation, thermal diffusivity (α) was dependent on specimen thickness (L) and the time for the specimen to rise to a quarter, half, and three quarters of the maximum temperature ($t_{0.25}$, $t_{0.5}$, $t_{0.75}$, respectively) after the laser pulse. Heat capacity was measured at the same time as thermal diffusivity by comparing the relative temperature rise of each specimen against a graphite standard using Equation 2, where ρ is bulk density, C_p is heat capacity, L is thickness of specimen, and ΔT is temperature rise of the specimen (M) and graphite standard (R).[37] Thermal conductivity (λ) was then calculated at each temperature from the measured thermal diffusivity (α), heat capacity (C_p), and temperature dependent bulk density (ρ), according to Equation (3).

$$\alpha = \frac{L^2}{t_{0.5}}[-0.346 + 0.362(t_{0.75}/t_{0.25}) - 0.065(t_{0.75}/t_{0.25})^2] \quad (1)$$

$$\left(\rho C_p\right)_M = \frac{L_R \Delta T_R}{L_M \Delta T_M}\left(\rho C_p\right)_R \quad (2)$$

$$\lambda = \alpha \rho C_p \quad (3)$$

Electrical resistivity was measured as a function of temperature up to 750°C in flowing Ar. Measurements were made by the 4-point bar method on bars that were 30 mm long, 2 mm wide, and 1.5 mm thick.[38] Data were collected after equilibrating for 10 minutes at each test temperature. Silver wire electrodes were used for the measurements and they were joined to the specimens with silver paint. Equation (4) was then used to calculate electrical resistivity based on the gauge length (L), the specimen width (w) and thickness (t), maximum current (I), and voltage (V).

$$\rho = \frac{wtV}{LI} \quad (4)$$

Results

Table I shows the designations for the compositions along with density and microstructural information about the ZrB_2-TiB_2 ceramics. For instance, nominally pure ZrB_2 (Zr0Ti) had a bulk density of 5.93 g/cm^3. The amount of porosity was 2.79 vol% based on the Archimedes' measurements, which were supported by SEM analysis as discussed below. The addition of a small amount of TiB_2, 5 vol% (Zr5Ti), decreased the bulk density to 5.75 g/cm^3. The porosity, however, increased to 3.57 vol%. For larger additions of TiB_2, such as 50 vol% in Zr50Ti, bulk density decreased to 5.27 g/cm^3, but the residual porosity also decreased to 0.39 vol%. The bulk density was expected to decrease with addition of TiB_2 (bulk density 4.495 g/cm^3). For all of the materials, the relative density of the specimens was greater than or equal to 96% based on nominal composition.

Table I: Designation, Bulk Density, and Microstructural Information for ZrB_2-TiB_2 Compositions

Designation	TiB_2 Content		Bulk Density	Theoretical Density	Porosity	Grain Size
	Vol%	Mol%	g/cm^3	g/cm^3	%	μm
Zr0Ti	0	0	5.93	6.10	2.8	22 ± 12
Zr1Ti	1	1.2	5.93	6.09	2.6	13 ± 7
Zr5Ti	5	5.9	5.75	6.02	3.6	13 ± 7
Zr10Ti	10	11.7	5.72	5.94	4.0	10 ± 5
Zr25Ti	25	28.5	5.65	5.70	0.6	9 ± 5
Zr50Ti	50	54.5	5.27	5.30	0.4	7 ± 4

The grain size of each specimen was measured from SEM images of polished, etched cross sections while the volume fraction of porosity was determined from polished cross sections (Figure 1). The largest average grain size was 22 μm for Zr0Ti. The average grain size decreased as the amount of TiB_2 increased with values of 13 μm for Zr5Ti and 9 μm for Zr25Ti. The smallest average grain size (7 μm) was measured for the largest addition of TiB_2, 50 vol% in Zr50Ti. Similarly, the standard deviation of the grain size decreased from ±12 μm for Zr0Ti to ±4 μm for Zr50Ti. Since a second phase was not visible in the SEM images, TiB_2 appeared to form a solid solution with ZrB_2

across the composition range that was studied. In addition, the presence of TiB_2 reduced the effects of grain coarsening and led to the decreased average grain size found in the ZrB_2-TiB_2 ceramics.

X-ray diffraction (XRD) analysis was used to confirm that TiB_2 dissolved into the ZrB_2 matrix for all of the compositions. XRD for Zr50Ti (Figure 2A) shows a solid solution between ZrB_2 and TiB_2 for the addition of 50 vol% TiB_2. This was expected based on the Zr-Ti-B phase diagram. The positions of the peaks shifted to higher 2θ values depending on the amount of TiB_2 added compared to nominally pure ZrB_2 (XRD card number: 34-0423). The shift to higher angles corresponded to a decreased lattice parameter with increasing TiB_2 additions because TiB_2 has a smaller unit cell than ZrB_2. The lattice parameters calculated from XRD patterns as a function of TiB_2 addition are shown in Figure 2B. Both the a and c lattice parameters decreased linearly with increasing amounts of TiB_2. Overall, XRD confirmed that additions of up to 50 vol% TiB_2 dissolved into ZrB_2 and formed a continuous solid solution.

The thermal diffusivity of the ZrB_2-TiB_2 ceramics was measured using the laser flash technique (Figure 3). For each composition, the thermal diffusivity decreased from room temperature to 2000°C. As an example, the thermal diffusivity of Zr0Ti decreased from 0.30 cm^2/sec at 25°C to 0.15 cm^2/sec at 2000°C. At 25°C, the addition of TiB_2 decreased the thermal diffusivity from 0.30 cm^2/sec for Zr0Ti to 0.21 cm^2/sec for Zr50Ti. At 2000°C, the magnitude of the decrease in thermal diffusivity due to the addition of TiB_2 was not as significant. For example, the thermal diffusivity was 0.15 cm^2/sec for Zr0Ti compared to 0.11 cm^2/sec for Zr50Ti, which is a decrease of 0.04 cm^2/sec at 2000°C compared to 0.09 cm^2/sec at 25°C. However, the percentage decrease was about the same for both temperatures, ranging from 25 to 30 percent for all of the compositions. The decrease in thermal diffusivity for TiB_2 additions of ≤10 vol% was linear over the entire temperature range. For additions of TiB_2 of >10 vol% the decrease in thermal diffusivity was lower than expected compared to smaller additions and not constant over the entire temperature range. In general, the addition of TiB_2 decreased the thermal diffusivity of the resulting ZrB_2 ceramics at all temperatures.

Heat capacity was also measured for ZrB_2-TiB_2 ceramics (Figure 4). For each composition, the heat capacity increased over the entire temperature range. The heat capacity increased more rapidly below 700°C, while above that temperature the increase in heat capacity appeared to be linear as a function of temperature. The heat capacity at 25°C increased from 430 J/kg•K for Zr0Ti to 519 J/kg•K for Zr50Ti due to the higher heat capacity of TiB_2 (shown in Figure 4). Similarly at 2000°C, the heat capacity was 753 J/kg•K for Zr0Ti and 1028 J/kg•K for Zr50Ti. The values of heat capacity for each composition were consistent with values predicted using a volumetric rule of mixtures calculation with the accepted values for each phase in the NIST-JANAF tables.[39]

Thermal conductivity was calculated from measured values of thermal diffusivity and heat capacity as well as temperature-dependent density calculated using published thermal expansion data.[40] For TiB_2 contents of 10 vol% and less, the thermal conductivity decreased as temperature increased (Figure 5). For nominally pure ZrB_2, the initial decrease in thermal conductivity was steep, from 93 W/m•K at 25°C to 76 W/m•K at 800°C. In contrast, the decrease was less severe at higher temperatures, from 76 W/m•K at 800°C to 67 W/m•K at 2000°C. The addition of TiB_2 reduced the thermal conductivity at all temperatures. For additions of TiB_2 of 10 vol% or less, the thermal conductivity at 25°C decreased from 93 W/m•K for Zr0Ti to 85 W/m•K for Zr5Ti, and to 77 W/m•K for Zr10Ti.

The addition of TiB_2 also changed the initial slope of the thermal conductivity as a function of temperature curves. Additions of more than 10 vol% TiB_2 to ZrB_2 decreased the thermal conductivity at 25°C significantly. Compared to a thermal conductivity of 93 W/m•K for Zr0Ti at 25°C, the thermal conductivity of Zr25Ti was 55 W/m•K and was 58 W/m•K for Zr50Ti. For the latter compositions, the thermal conductivity increased between 25°C and 800°C. For Zr50Ti the thermal conductivity increased from 58 W/m•K at 25°C to 65 W/m•K at 800°C. Above 800°C, the thermal conductivity decreased linearly for all compositions. For comparison, the thermal conductivity of Zr0Ti decreased from 72 W/m•K at 800°C to 67 W/m•K at 2000°C, which was similar to the decrease from 65 W/m•K at 800°C to 59 W/m•K at 2000°C for Zr50Ti.

To further characterize the effects of solid solution formation, thermal conductivity was separated into phonon and electron contributions to the overall thermal conductivity. To determine the electron contribution to thermal conductivity, the electrical resistivity was measured as a function of temperature (Figure 6A). The electrical resistivity increased linearly with respect to temperature, which is typical of free electron motion for metallically bonded materials. The presence of metallic bonding can also be inferred from the relative values of electrical resistivity. For example, the measured resistivity of Zr0Ti was 9.69 μΩ•cm 25°C. The resistivity as a function of temperature plots all had the same slope, ~0.033 μΩ•cm/°C, regardless of the amount of TiB_2 added. The slope values imply that the electron mean free path is the same for all of the compositions. This also implies that the solid solution did not result in lattice distortions or other microstructural changes that would affect electron-phonon interactions.

The addition of TiB_2 to ZrB_2 increased the room temperature electrical resistivity (Figure 6B). Specifically, the 25°C electrical resistivity increased from 9.69 μΩ•cm for Zr0Ti to 12.92 μΩ•cm for Zr50Ti. The electrical resistivity of the ZrB_2-TiB_2 ceramics followed Nordheim's rule for metallic conductors, which is a typical model for the electrical resistivity of solid solutions. Equation 4 is a fit of the measured electrical resistivity values to Nordheim's rule and is shown as the solid line on Figure 6B. For Equation 4, x is mol% of TiB_2, ρ_{ZrB2} and ρ_{TiB2} are the electrical resistivities of nominally pure ZrB_2 (9.69 μΩ•cm) and TiB_2 (9.00 μΩ•cm). The value of electrical resistivity for TiB_2 reported by Venkateswaran et al., was used to calculate the function in Figure 6B.[41] As discussed above, all of the specimens showed similar changes in resistivity as a function of temperature. Because titanium atoms substitute onto zirconium sites, only the non-temperature-dependent portion of electrical resistivity was affected, which is consistent with Nordheim's rule for metallic solid solutions.[42,43]

$$\rho_{SS} = x\rho_{TiB_2} + (1-x)\rho_{ZrB_2} + 14.12x(1-x) + 26.92xe^{-9.86x} \qquad (4)$$

The electron contribution (λ_e) to the thermal conductivity was calculated from measured electrical resistivity values using the Weidemann-Franz law (Equation 5), where L is the Lorentz number (2.45×10^{-8} W•Ω•K^{-2} reported for ZrB_2), T is the absolute temperature, and ρ is electrical resistivity.[44] For Zr0Ti, the electron contribution to thermal conductivity initially decreased before leveling out at ~600°C (Figure 7A). The addition of TiB_2 to ZrB_2 decreased the electron contribution to thermal conductivity. For example, the electron contribution was 76 W/m•K for Zr0Ti and decreased to 65 W/m•K for Zr5Ti at 25°C. Larger additions of TiB_2 decreased the electron contribution to as low as 57 W/m•K at 25°C for Zr50Ti. The additions of TiB_2 also changed electron contribution relationship with temperature. For Zr5Ti, the electron contribution to thermal conductivity increased from 65 W/m•K at 25°C to 70 W/m•K at 600°C. For comparison, the electron contribution to thermal conductivity of Zr0Ti decreased from 76 W/m•K at 25°C to 71W/m•K at 600°C. The change in slope was due to a solid solution formation, which altered electron transport through the ZrB_2 lattice.

$$\lambda_e = \frac{LT}{\rho} \tag{5}$$

The phonon contribution (λ_{ph}) to thermal conductivity was calculated by subtracting the electron contribution from the total thermal conductivity (Equation 6). Shown in Figure 7B, the phonon contribution to thermal conductivity decreased with increasing temperature. For instance, the phonon contribution to thermal conductivity for Zr0Ti decreased from 17 W/m•K at 25°C to 6 W/m•K at 700°C. Small additions of TiB_2, ≤10 vol%, did not affect the phonon contribution to thermal conductivity significantly. This may be due to the fact that titanium is a substitutional atom in ZrB_2 that has a similar atomic size and valence state. Larger additions of Ti, however, decreased the phonon contribution to nearly zero for Zr25Ti and Zr50Ti. The difference in phonon contributions was attributed to the large number of titanium atoms (≥25 vol%) that affected phonon transport through the ZrB_2 structure.

$$\lambda_{ph} = \lambda_{Total} - \lambda_e \tag{6}$$

Discussion

The phonon contribution to thermal conductivity was evaluated using models that describe the effects of solid solution and temperature. Based on research by Smith et al. on Al_2O_3, the relationship between the phonon contribution to thermal conductivity and TiB_2 content can be described by Equation (7), where a is a constant based on the phonon frequency and amplitude, T is the absolute temperature, and R*/l is a constant that depends on the phonon mean free path. This model has been used previously for ZrB_2 and ZrB_2-SiC ceramics as reported by Zimmermann et al., where the mean free path of phonons was estimated to be the grain size. The average grain size of ZrB_2 in that study was 6 μm. In the present analysis, the grain size was too large (>6 μm) to be used as the mean free path. Instead, the relative change in the phonon contribution to thermal conductivity was used to estimate the effect of solid solution formation on phonon mean free path.

$$\frac{1}{\lambda_{Ph}} = aT + \frac{R^*}{l} \tag{7}$$

The phonon contribution constant did not change significantly for TiB_2 additions of ≤10 vol%, with an average value for a of 2.20×10^{-4} m/W for Zr0Ti, Zr5Ti and

Zr10Ti. This value was obtained by a best fit analysis. Also, the magnitude of R*/l was insignificant (<1 x 10^{-4} m•K/W) for these compositions compared to the aT term, which meant that the mean free path was not affected by relatively small addition of TiB_2 to ZrB_2. For TiB_2 additions of >10 vol%, the value for a increased to 4.88 m/W and R*/l was 0.394 m•K/W. The increased a values showed that the larger number of Ti atoms changed the frequency of the phonons through the ZrB_2-TiB_2 lattice. The value of R*/l also became significant compared to the aT term, which meant that the mean free path was smaller for Zr25Ti and Zr50Ti than in specimens with ≤10 vol% TiB_2. This behavior showed that the addition of more than 10 vol% TiB_2 decreased the phonon contribution by adding a large number of Ti atoms to the ZrB_2 lattice and decreasing the grain size, which decreased the mean free path of phonon transport.

A combination of calculated electron and phonon contributions was used to estimate the total thermal conductivity of ZrB_2-TiB_2 ceramics as a function of solid solution content. Figure 8 showed that the sum of the electron and phonon models (solid lines) predict the measured values (individual points). The largest differences between the model predictions and experimental data were observed at 25°C. This may be due to breakdown of the phonon contribution model below about half the Debye temperature, which is 325°C based on a reported Debye temperature of 650°C for ZrB_2.[31] Typically, accurate prediction of the phonon contribution to thermal conductivity requires use of separate “low” and “high” temperature models.[24] The variation of the Lorentz number may also contribute to the difference between measured and calculated values. Overall, the predicted values for total thermal conductivity were within 4% of experimental values below 325°C. At higher temperatures, the total thermal conductivity was dominated by the electron contribution, which resulted in better agreement between predicted and measured values since measured electrical resistivity was used to calculate the electron contribution. The maximum difference between the predicted and measured values above 325°C was 2% for Zr10Ti at 600°C. The majority of calculated values were within 1% of experimental values for temperatures above 325°C. The model used to describe the thermal conductivity of ZrB_2-TiB_2 ceramics showed that the combination of electron and phonon models is required to accurately describe how solid solution affects the thermal conductivity. This is evident because the electron and phonon contributions are affected differently with the addition of TiB_2.

Conclusion

ZrB_2 with additions of TiB_2 up to 50 vol% were densified by hot pressing at 2100°C to over 96% of theoretical density. The resulting ceramics formed complete solid solutions that were confirmed by phase and microstructure analysis. The addition of TiB_2 also decreased the grain size of the ceramics from 22 μm for Zr0Ti to 7 μm for Zr50Ti. The resulting thermal conductivity decreased with the addition of TiB_2 from 92 W/m•K for Zr0Ti to <60 W/m•K for Zr25Ti and Zr50Ti. The following conclusions can be drawn from this study:

1. At temperatures less than 1000°C, the slope of thermal conductivity as a function of temperature changed significantly as a result of TiB_2 addition, where additions of TiB_2 greater than 10 vol% led to and increase in the initial slope. This change was a result of a significant decrease in the low temperature thermal conductivity

from 92 W/m•K for Zr0Ti to with a minimum value of 58 W/m•K for Zr50Ti at 25°C.

2. The electron contribution to thermal conductivity decreased considerably from nominally pure ZrB_2, which had a value of 76 W/m•K at 25°C to Zr50Ti, which has a value of 57 W/m•K at 25°C. The decrease was consistent with Nordheim's rule for solid solutions, which indicated interaction of Ti and Zr atoms that increased electrical resistivity compared to pure ZrB_2.

3. The phonon contribution to thermal conductivity decreased from 17 W/m•K to nearly zero with the addition of TiB_2 to ZrB_2. This decrease was a result of decreased grain size and interference of phonon waves caused by the substitution of Ti onto Zr sites in the ZrB_2 lattice.

4. Two models were used to predict the electron and phonon contributions to thermal conductivity and their sum had good correlation with experimental results. The agreement showed that solid solution formation limited the transfer of electrons and phonons, which decreased thermal conductivity as Ti was added into the ZrB_2 lattice.

Acknowledgements

The authors would like to acknowledge the AMCL at Missouri S&T for the use of the SEM and XRD.

References

1. R.A. Cutler, "Engineering Properties of Borides," pp. 787-803 in Vol. 4, *Ceramics and Glasses: Engineered Materials Handbook.* Edited by S. J. S. Jr. ASM International, Materials Park, OH, 1991.

2. X. Zhang, X. Luo, J. Han, J. Li, and W. Han, "Electronic structure, elasticity and hardness of diborides of zirconium and hafnium: First principles calculations," *Computational Materials Science,* **44** [2] 411-21 (2008).

3. D.E. Wiley, W.R. Manning, and O. Hunter Jr, "Elastic properties of polycrystalline TiB_2, ZrB_2 and HfB_2 from room temperature to 1300K," *Journal of the Less Common Metals,* **18** [2] 149-57 (1969).

4. L.S. Sigl R. Telle, and K. Takagi, "Boride-Based Hard Materials," pp. 802-945 in *Handbook of Ceramic Hard Materials.* Edited by R. Riedel. Wiley-VCH, Weinheim, Germany, 2000.

5. O. Kida, "Monolithic Refractory Material and Waste Melting Furnace Using the Same," Japanese Patent JP2000335969, May 12, 2000.

6. M. Gasch, S. Johnson, and J. Marschall, "Thermal Conductivity Characterization of Hafnium Diboride-Based Ultra-High-Temperature Ceramics," *Journal of the American Ceramic Society,* **91** [5] 1423-32 (2008).

7. S. Guo, Y. Kagawa, T. Nishimura, and H. Tanaka, "Thermal and Electric Properties in Hot-Pressed ZrB_2-$MoSi_2$-SiC Composites," *Journal of the American Ceramic Society,* **90** [7] 2255-8 (2007).

8. L. Zhang, D.A. Pejaković, J. Marschall, and M. Gasch, "Thermal and Electrical Transport Properties of Spark Plasma-Sintered HfB2 and ZrB2 Ceramics," *Journal of the American Ceramic Society,* **94** [8] 2562-70 (2011).

9. H.J. Juretschke and R. Steinitz, "Hall Effect and Electrical Conductivity of Transition-Metal Diborides," *Journal of Physics and Chemistry of Solids,* **4** [1-2] 118-27 (1957).

10. M.M. Opeka, I.G. Talmy, and J.A. Zaykoski, "Oxidation-based materials selection for 2000C + hypersonic aerosurfaces: Theoretical considerations and historical experience: Special Section: Ultra-High Temperature Ceramics (Guest Editors: Joan Fuller and Michael D. Sacks)," *Journal of Materials Science,* **39** 5887-904 (2004).

11. D. Kalish and E. V. Clougherty, "Densification Mechanisms in High-pressure Hot-Pressing of HfB_2," *Journal of the American Ceramic Society,* **52** [1] 26-30 (1969).

12. W. G. Fahrenholtz, G. E. Hilmas, I. G. Talmy, and J. A. Zaykoski, "Refractory Diborides of Zirconium and Hafnium," *Journal of the American Ceramic Society,* **90** [5] 1347-64 (2007).

13. A. Rezaie, W.G. Fahrenholtz, and G.E. Hilmas, "Effect of hot pressing time and temperature on the microstructure and mechanical properties of ZrB_2-SiC," *Journal of Materials Science,* **42** [8] 2735-44 (2007).

14. A.L. Chamberlain, W.G. Fahrenholtz, G.E. Hilmas, and D.T. Ellerby, "High-Strength Zirconium Diboride-Based Ceramics," *Journal of the American Ceramic Society,* **87** [6] 1170-2 (2004).

15. M. Gasch, D. Ellerby, E. Irby, S. Beckman, M. Gusman, and S. Johnson, "Processing, properties and arc jet oxidation of hafnium diboride/silicon carbide ultra high temperature ceramics: Special Section: Ultra-High Temperature Ceramics (Guest Editors: Joan Fuller and Michael D. Sacks)," *Journal of Materials Science,* **39** 5925-37 (2004).

16. S.-Q. Guo, Y. Kagawa, T. Nishimura, D. Chung, and J.-M. Yang, "Mechanical and physical behavior of spark plasma sintered ZrC-ZrB_2-SiC composites," *Journal of the European Ceramic Society,* **28** [6] 1279-85 (2008).

17. S. C. Zhang, G. E. Hilmas, and W. G. Fahrenholtz, "Pressureless Densification of Zirconium Diboride with Boron Carbide Additions," *Journal of the American Ceramic Society,* **89** [5] 1544-50 (2006).

18. L. Silvestroni and D. Sciti, "Effects of $MoSi_2$ additions on the properties of Hf- and Zr-B2 composites produced by pressureless sintering," *Scripta Materialia,* **57** [2] 165-8 (2007).

19. William G. Fahrenholtz, Gregory E. Hilmas, Shi C. Zhang, and Sumin Zhu, "Pressureless Sintering of Zirconium Diboride: Particle Size and Additive Effects," *Journal of the American Ceramic Society,* **91** [5] 1398-404 (2008).

20. S. Zhu, W.G. Fahrenholtz, G.E. Hilmas, and S.C. Zhang, "Pressureless sintering of carbon-coated zirconium diboride powders," *Materials Science and Engineering: A,* **459** [1-2] 167-71 (2007).

21. J. Zou, S.-K. Sun, G.-J. Zhang, Y.-M. Kan, P.-L. Wang, and T. Ohji, "Chemical Reactions, Anisotropic Grain Growth and Sintering Mechanisms of Self-Reinforced ZrB_2–SiC Doped with WC," *Journal of the American Ceramic Society,* **94** [5] 1575-83 (2011).

22. S. Baik and P.F. Becher, "Effect of Oxygen Contamination on Densification of TiB_2," *Journal of the American Ceramic Society,* **70** [8] 527-30 (1987).

23. M. Thompson, W.G. Fahrenholtz, and G. Hilmas, "Effect of Starting Particle Size and Oxygen Content on Densification of ZrB_2," *Journal of the American Ceramic Society,* **94** [2] 429-35 (2011).

24. D.S. Smith, S. Fayette, S. Grandjean, C. Martin, R. Telle, and T. Tonnessen, "Thermal Resistance of Grain Boundaries in Alumina Ceramics and Refractories," *Journal of the American Ceramic Society,* **86** [1] 105-11 (2003).

25. D.M. Van Wie, D.G. Drewry, D.E. King, and C.M. Hudson, "The hypersonic environment: Required operating conditions and design challenges," *Journal of Materials Science,* **39** [19] 5915-24 (2004).

26. W.D. Kingery, "Factors Affecting Thermal Stress Resistance of Ceramic Materials," *Journal of the American Ceramic Society,* **38** [1] 3-15 (1955).

27. M.M. Opeka, I.G. Talmy, E.J. Wuchina, J.A. Zaykoski, and S.J. Causey, "Mechanical, Thermal, and Oxidation Properties of Refractory Hafnium and zirconium Compounds," *Journal of the European Ceramic Society,* **19** 2405-14 (1999).

28. G.V. Samsonov, B.A. Kovenskaya, and T.I. Serebryakova, "Some physical characteristics of the diborides of transition metals of groups IV and V," *Russian Physics Journal,* **14** [1] 11-4 (1971).

29. R.P. Tye and E.V. Clougherty, "The Thermal and Electrical Conductivities of some Electrically Conducting Compounds," *Proceedings of the Fifth Symposium on Thermophysical Properties,* 396-401 (1970).

30. R.G. Munro, "Material Properties of Titanium Diboride," *Journal of Research of the National Institute of Standards and Technology,* **105** 709-20 (2000).

31. J.W. Zimmermann, G.E. Hilmas, W.G. Fahrenholtz, R.B. Dinwiddie, W.D. Porter, and H. Wang, "Thermophysical Properties of ZrB_2 and ZrB_2-30SiC Ceramics," *Journal of the American Ceramic Society,* **91** [5] 1405-11 (2008).

32. W.-B. Tian, Y.-M. Kan, G.-J. Zhang, and P.-L. Wang, "Effect of carbon nanotubes on the properties of ZrB_2-SiC ceramics," *Materials Science and Engineering: A,* **487** [1-2] 568-73 (2008).

33. N. Kaur, R. Mohan, N.K. Gaur, and R.K. Singh, "Cohesive and thermal properties of transition metal diborides," *Physica B: Condensed Matter,* **404** [8-11] 1607-10 (2009).

34. ASTMC373, "Standard Test Method for Water Absorption, Bulk Density, Apparent Porosity, and Apparent Specific Gravity of Fired Whiteware Products," *ASTM International,* (2006).

35. ASTME1461, "Standard Test Method for Thermal Diffusivity of Solids by the Flash Method," *ASTM International,* (2001).

36. L.M. Clark and R.E. Taylor, "Radiation loss in the flash method for thermal diffusivity," *Journal of Applied Physics,* **46** [2] 714-9 (1975).

37. K. Shinzato and T. Baba, "A Laser Flash Apparatus for Thermal Diffusivity and Specific Heat Capacity Measurements," *Journal of Thermal Analysis and Calorimetry,* **64** [1] 413-22 (2001).

38. ASTMF76, "Standard Test Methods for Measuring Resistivity and Hall Coefficient and Determining Hall Mobility in Single-Crystal Semiconductors," *ASTM International,* (2008).

39. M.W. Chase, *NIST-JANAF Thermochemical Tables*. American Chemical Society and the American Institute of Physics, Woodbury, NY, 1998.

40. Y. Touloukian, C. Ho, and D. Dewitt, *Thermal Expansion: Nonmetallic Solids,* Vol. 13. Edited by Touloukian. IFI/Plenum, New York, 1970.

41. T. Venkateswaran, B. Basu, G.B. Raju, and D.-Y. Kim, "Densification and properties of transition metal borides-based cermets via spark plasma sintering," *Journal of the European Ceramic Society,* **26** [13] 2431-40 (2006).

42. S.O. Kasap, *Principles of Electrical Engineering Materials and Devices*. McGraw-Hill, Boston, 1997.

43. L. Solymar and D. Walsh, *Electrical Properties of Materials,* 7 ed. Oxford University Press Inc., New York, 2004.

44. R. Franz and G. Wiedemann, "Ueber die Wärme-Leitungsfähigkeit der Metalle," *Annalen der Physik,* **165** [8] 497-531 (1853).

FIGURES:

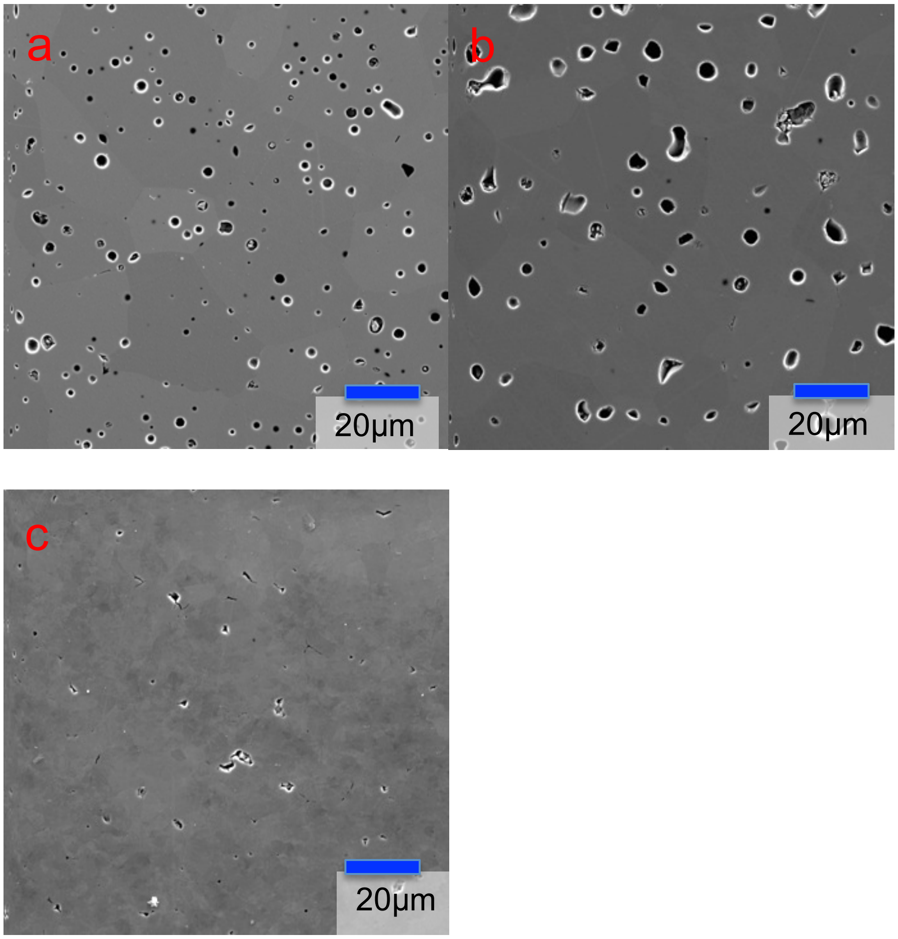

Figure 1: Representative SEM images of polished cross sections of (a) Zr0Ti, (b) Zr10Ti, and (c) Zr50Ti.

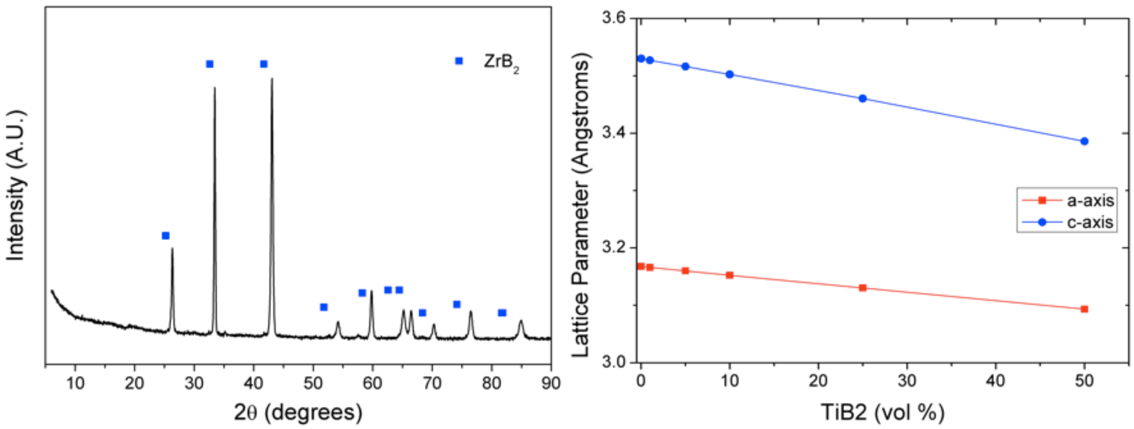

A B

Figure 2: X-Ray diffraction analysis confirming that ZrB_2 and TiB_2 formed a single phase solution (A) and that the addition of TiB_2 decreased the lattice parameters compared to nominally pure ZrB_2 (B).

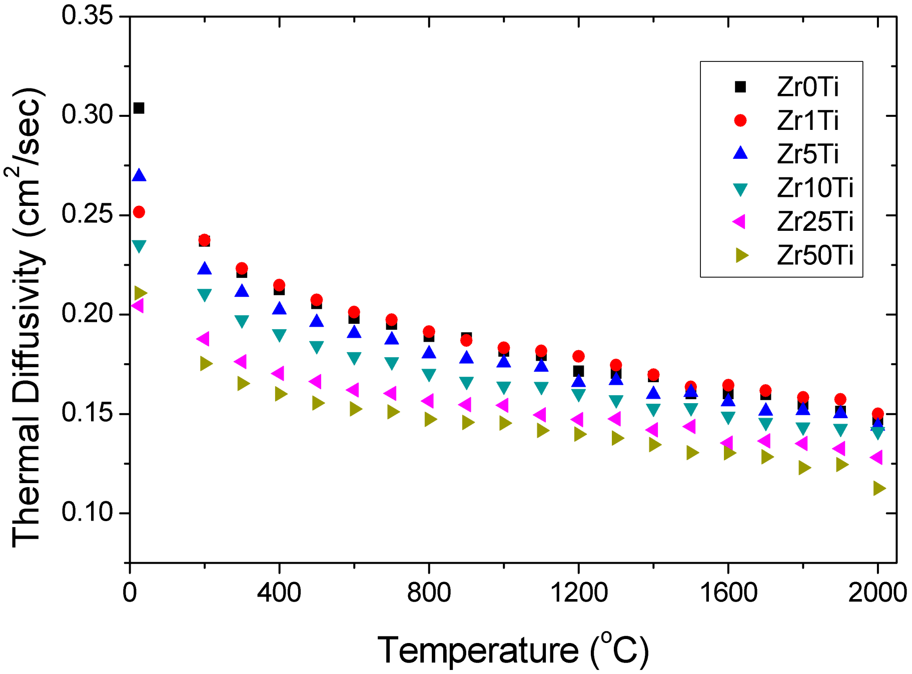

Figure 3: Thermal diffusivity of ZrB_2-TiB_2 ceramics from room temperature up to 2000°C.

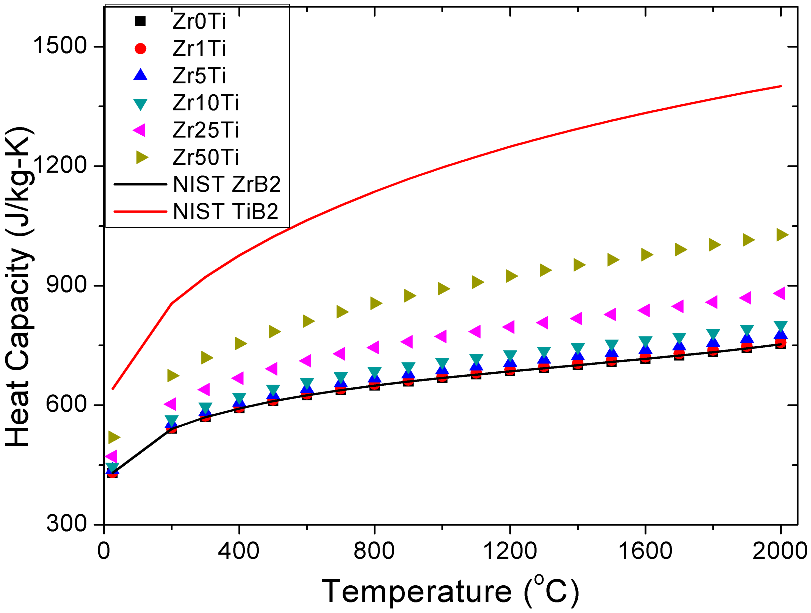

Figure 4: Heat capacity as a function of temperature for ZrB_2-TiB_2 ceramics along with handbook values for pure ZrB_2 and TiB_2.[39]

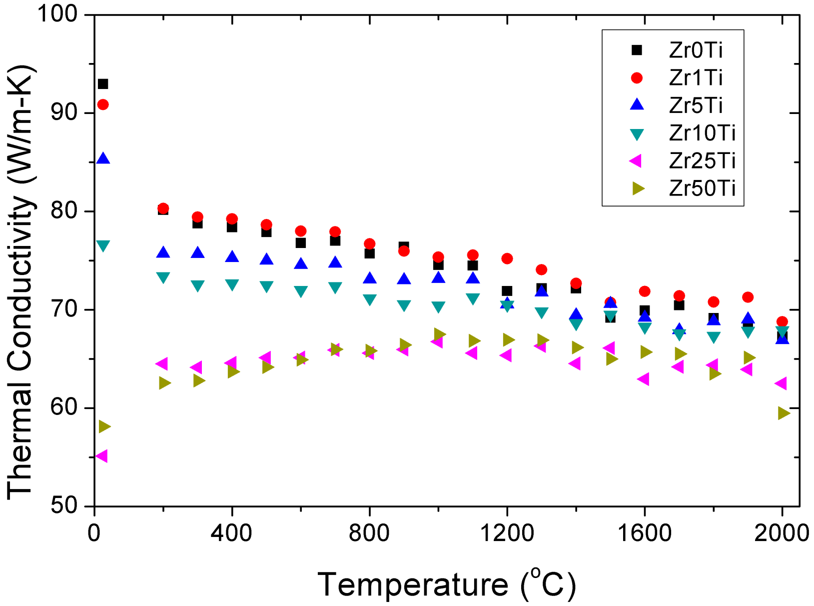

Figure 5: Thermal conductivity as a function of temperature for ZrB_2-TiB_2 ceramics calculated from the thermal diffusivity, heat capacity, and bulk density.

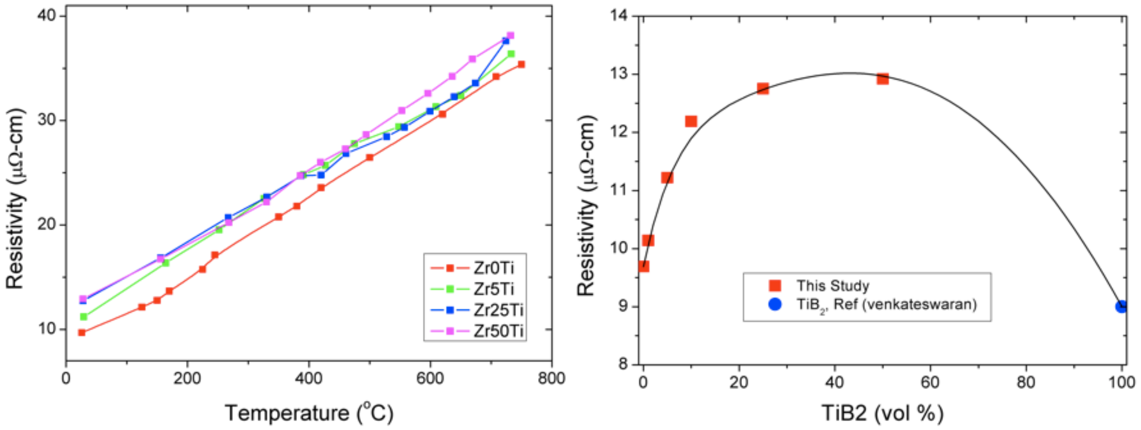

A B

Figure 6: Electrical resistivity of ZrB_2-TiB_2 ceramics (A) as a function of temperature up to 750°C and (B) at room temperature as a function of composition.

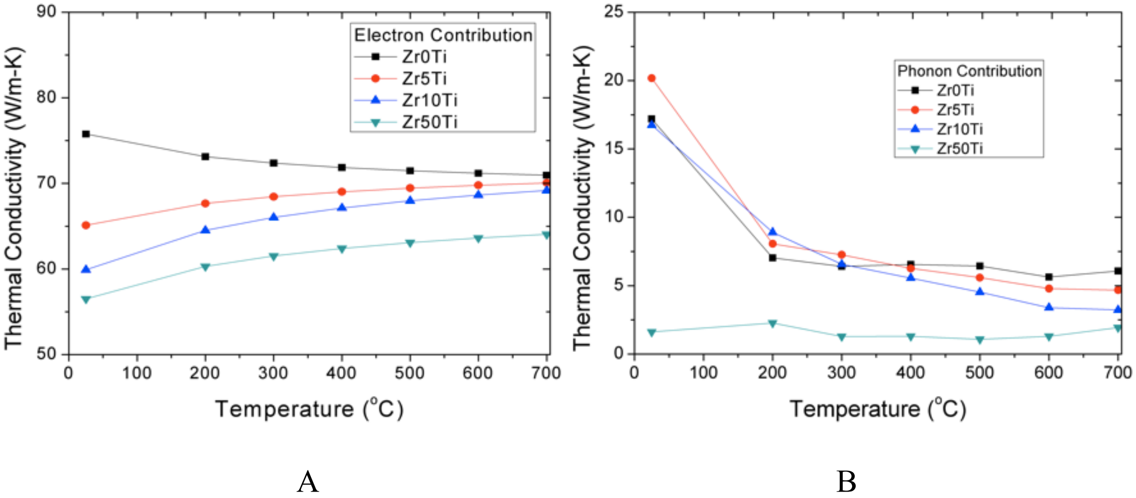

Figure 7: The electron (A) and phonon (B) contributions to thermal conductivity calculated based on electrical resistivity data as a function of temperature up to 750°C.

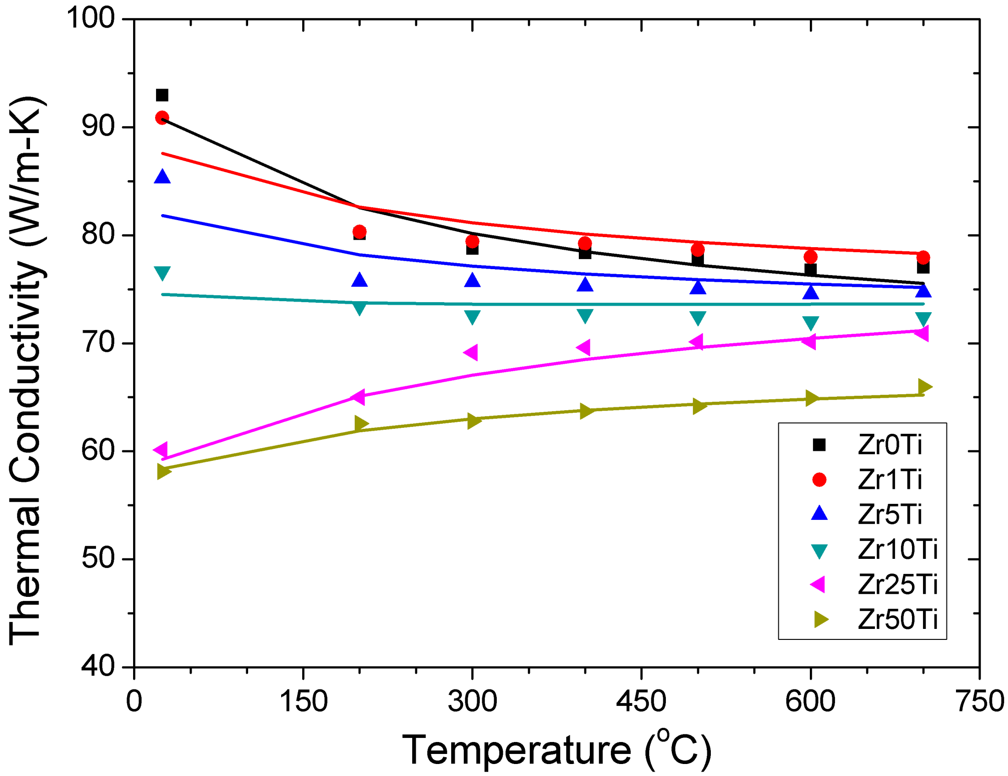

Figure 8: Thermal conductivity of ZrB_2-TiB_2 ceramics. The symbols are measured values and the lines associated with composition were calculated using electron and phonon conduction models.

SECTION

3. CONCLUSIONS

Processing-microstructure-property relationships were investigated for ZrB_2-based ceramics. Initially, the effects of powder processing and densification method on the densification behavior were investigated. The ceramics produced showed that density was affected by the addition of carbon, which reacted with and removed initial oxygen impurities from the ZrB_2. Other additives including B_4C and WC also promoted removal of oxides present on particle surfaces and decreased the temperature required to achieve full density. WC, introduced as an impurity during attrition milling, worked as a sintering aid, and allowed full density of ZrB_2 to be reached as low as 1900°C.

A number of characterization techniques were employed to determine how small concentrations (<5 vol%) of additives were incorporated into ZrB_2 ceramics. Microstructures were analyzed to identify the changes in average grain sizes, distributions of grain sizes, formation of second phases, and morphology of second phases. This analysis revealed that carbon was present as elongated grain boundary phases, which reacted with oxide impurities and/or ZrB_2 at temperatures of ~2000°C to form ZrC. Another addition, B_4C, was present as an isolated second phase that inhibited ZrB_2 grain growth, reducing grain sizes from >20 μm for nominally pure ZrB_2 to less than 10 μm for ceramics with residual B_4C. In contrast to C and B_4C, additions such as WC or TiB_2 formed solid solutions with ZrB_2, which were confirmed by x-ray diffraction analysis to change the lattice parameters of ZrB_2. Raman spectroscopy was also employed to identify that the carbon formed a graphitic structure and to confirm the stoichiometry of B_4C.

Flexure strength, elastic modulus, and Vickers hardness were measured for dense ZrB_2 produced from as received and attrition milled powders with the addition of second phases. Based on mechanical property characterization, the densification method, or more precisely the time at elevated temperature required to promote densification, played a significant role in mechanical properties. For example, pressureless sintering required about 120 minutes at temperatures >2000°C, which increased grain size and resulted in the distribution of second phases along grain boundaries (in particular, carbon), which led to intergranular failure. When hot pressing or spark plasma sintering, grain sizes were reduced from above 8 μm (for pressureless sintering) to less than 3 μm for ZrB_2 that was produced from attrition milled powder. Ceramics with finer grain sizes exhibited mixed mode or transgranular failure, indicative of stronger grain boundaries. Cooling rates over 100°C/min during spark plasma sintering caused microcracking that decreased the elastic modulus to less than 460 GPa compared to more than 500 GPa for dense ZrB_2 produced using cooling rates of 40-50°C/min. In cases where microcracking was not observed, the strength of the ceramics showed an inverse square root relationship with grain size, which is predicted by the Griffith relationship for ceramics free of other larger flaws. Strengths above 600 MPa for nominally pure ZrB_2 were achieved when grain sizes were less than 2 μm.

The use of ZrB_2 at elevated temperatures has been of particular interest for thermal protection systems for future hypersonic aerospace vehicles. For these applications, high thermal conductivities are desired so that heat can be conducted away from sharp leading edges where it is generated to cooler areas where it can be dissipated. A number of recent studies have used attrition milling to reduce the starting particle size. However, attrition milling introduces WC impurities that form a solid solution with ZrB_2 and significantly reduce the thermal conductivity, particularly below the Debye temperature of ~650°C. The room temperature thermal conductivity decreased from 95 W/m•K for nominally pure ZrB_2 to ~25 W/m•K for ZrB_2 containing 2.2 wt% WC. For comparison, the addition of 50 vol% TiB_2 (42.4 wt%) also formed a solid solution with ZrB_2, but only decreased the thermal conductivity to 58 W/m•K at 25°C. The addition of carbon to attrition milled ZrB_2 resulted in the formation of ZrC, which absorbed nearly 25 wt% of the WC in the ZrB_2 and resulted in an increase in the thermal conductivity to >30 W/m•K at room temperature. Compared to the addition of W, other additives that formed isolated particles or solid solutions were not as detrimental to thermal conductivity above 1000°C.

Key Technical Questions Addressed By This Research

Several technical questions were presented in the Introduction of this dissertation. The questions were addressed in the analysis presented in the manuscripts that make up the body of this dissertation. The answers to the technical questions are as follows.

1. *How does the densification method affect the microstructure and mechanical properties of ZrB_2 with varying oxygen contents?*

   ZrB_2 ceramics were densified by pressureless sintering, hot pressing, and spark plasma sintering at temperatures as low as 1900°C. The oxygen contents of the dense ceramics were different due to different oxygen impurity contents of the starting powders and by different levels of carbon additions. Densification by pressureless sintering required oxygen contents of <0.1 wt% to achieve relative densities of 97.6%. However, the extended time at elevated temperature resulted in grain coarsening. The application of external pressure during hot pressing enabled densification of ZrB_2 with higher oxygen contents and reduced the effects of grain coarsening by limiting the time that the ceramics spent at temperatures above 1500°C. Hot pressed ceramics had grain sizes <5 μm compared to >15 μm for ceramics produced by pressureless sintering. Spark plasma sintering, which used a pulsed DC current that promoted removal oxygen impurities, produced ceramics with grain sizes <3 μm, regardless of the initial oxygen contents. Ultimately, the mechanical strength was affected by the grain size, which could be controlled by limiting the effects of grain coarsening. Spark plasma sintering produced ceramics with the highest strengths, >500 MPa, because of rapid densification rates and reduction of oxygen impurities, which led to dense ceramics with the smallest average grain sizes.

2. *Does the heating rate used during hot pressing or spark plasma sintering impact the mechanical and/or thermal properties of ZrB_2?*

   ZrB_2 was densified by HP and SPS using heating rates ranging from 5°C/min to 300°C/min. The flexure strength of HP ZrB_2 was proportional to the inverse square root of maximum grain size, which is consistent with predictions based on the Griffith criteria. Based on the Griffith relationship, SPS ZrB_2 had a critical flaw size of ~19 μm, which was much larger than the maximum grain size of 6.3 μm. The discrepancy between the calculated flaw size and the measured maximum grain size was due to microcracking, which reduced the strength of SPS ZrB_2. Microcracking was observed in SEM images and it also reduced the elastic modulus to less than 460 GPa, compared to more than 500 GPa for fully dense ZrB_2. The thermal conductivity of HP ZrB_2 was lower for ceramics produced using heating rates greater than 20°C/min, whereas no differences were observed for heating rates below 20°C/min. For HP heating rates greater than 20°C/min, SEM analysis revealed that up to 3.3 vol% ZrO_2 (HP80) was present in the dense ceramics. The presence of this low thermal conductivity phase decreased the thermal conductivity compared to HP ZrB_2 produced using heating rates less than of equal to 20°C/min or SPS ZrB_2, which were free of ZrO_2 inclusions.

3. *How do carbon additions affect the thermal conductivity of ZrB_2 ceramics?*

Excess carbon present after densification of ZrB_2 reacted to form ZrC during a post densification heat treatment. During the first heating cycle, the thermal diffusivity changed irreversibly when the ceramics were above 1500°C. Analysis concluded that the thermal diffusivity changed irreversibly due to changes in the microstructure that started between 1550°C and 1650°C. Extended time above 1550°C resulted in the formation of the ZrC phase and the migration of W impurities from the ZrB_2 matrix into the newly formed ZrC. Thermal conductivity at 2000°C was as high as 64.2 W/m•K for ZrB_2 containing 3 wt% carbon. The second phases of graphite and ZrC decreased the phonon contribution to thermal conductivity to nearly zero. However, the resulting decrease in the W content in the ZrB_2 matrix increased the electron contribution to thermal conductivity and gave ZrB_2 with 3 wt% carbon the highest overall thermal conductivity.

4. *Does the formation of solid solutions alter the electron and phonon contributions to thermal conductivity of ZrB_2 ceramics?*

   X-ray diffraction analysis showed that TiB_2 added to ZrB_2 resulted in the formation of $(Zr,Ti)B_2$ solid solutions. The thermal conductivity at 25°C ranged from 93 W/m•K for nominally pure ZrB_2 to 58W/m•K for ZrB_2 containing 50 vol% TiB_2. The electron contribution to thermal conductivity, which was 76 W/m•K for nominally pure ZrB_2, decreased to 57 W/m•K when 50 vol% TiB_2 was added. The phonon contribution to thermal conductivity was not noticeably affected by TiB_2 additions of 10 vol% or less. For larger additions of TiB_2, however, the phonon contribution decreased to nearly zero from 25°C to 700°C. In general, both the electron and phonon contributions decreased due to the formation of solid solutions, but ZrB_2 with >10 vol% TiB_2 affected the phonon contribution significantly more.

This research was a systematic study on how densification method, impurities, and additives affect the thermal conductivity and mechanical strength of ZrB_2 based ceramics. The importance of controlling thermal conductivity was to improve ZrB_2 based ceramics for thermal protection systems that require both high mechanical strength and thermal conductivity. The work presented in this dissertation can be divided into three areas in which significant advances in fundamental understanding were achieved. First, the densification technique and other processing parameters affected the density and microstructure of ZrB_2 based ceramics, which directly impacted strength and thermal conductivity. Second, additive and impurity contents created a trade off between mechanical and thermal properties, meaning that ceramics could be designed to maximize either strength or thermal conductivity individually, but not both simultaneously. Lastly, material reactions during densification and at use temperatures were observed and affected the thermal conductivity behavior of ZrB_2 ceramics.

4. RECOMMENDATIONS FOR FUTURE WORK

The goal of the research presented in this dissertation was to investigate the effects of densification method, impurity content, and additives on the thermal and mechanical properties of ZrB_2 ceramics. During the course of this research, a number of areas were identified that could be the subject of future investigations.

1. The effect of solid solution on the electron and phonon contributions to thermal conductivity should be investigated. In particular, some diborides form limited solid solutions with group 4 diborides. The change in solubility limit of diborides indicates that there is a difference in the number of metal-metal and metal-boron bonds that form, thus changing the number of free electrons. These changes can significantly change electron and phonon contributions to thermal conductivity and should be explored.
2. The elevated temperature thermal properties of ZrB_2 should be more systematically studied with additions of non-conducting and semi-conducting second phases including: SiC, carbon, $MoSi_2$, etc. While several different additions have been used to remove oxides as well as create passive oxidation resistance, little information of measured thermal conductivity has been reported near the intended use temperature. Specifically, only a limited number of studies have been conducted to explain how electron and phonon transport are affected at high temperatures with more than about 10 vol% of second phases. Also, the thermal transport mechanisms of UHTCs are not well understood.

3. A useful area to explore would be additions that allow the use of WC during processing, but remove solid solutions from the matrix phase. WC forms a solid solution in ZrB_2. A second phase, ZrC, was shown in the carbon addition study to absorb up to 25% WC and trap it in a minor phase. Other researchers have found similar results with Si containing phases that form WSi_2 (Watts, JECS 2010). A more systematic investigation may show that WC introduced during powder processing can be removed from solid solution with ZrB_2 and contained in a small amount of a second phase, <5 vol%. This could provide a better knowledge about the trade off between thermal and mechanical properties.

4. A significant study to improve the knowledge base for electrical behavior is needed. Hall resistivity measurements would improve the understanding the effect of impurities on the concentration of charge carriers and mobility of carriers. Also, the electrical resistivity measurements reported to date have been between room temperature and 1300°C. Higher temperature data could be collected by using W or high temperature thermocouple wires, which could provide electrical measurements up to the intended use temperature, ~2000°C. Electrical resistivity measurements could also be made at temperatures below room temperature using Bloch-Gruneisen behavior of metals. This would help indicate what factors are affecting resistivity of materials including electron-phonon interactions, s-d oribital electron interactions, general electron-electron interactions, and defect scattering. This information could explain how certain defects interact with ZrB_2 to change thermal properties.

APPENDIX

ELEVATED TEMPERATURE THERMAL PROPERTIES OF ZRB$_2$-B$_4$C CERAMICS

Matthew Thompson*; William G. Fahrenholtz; Greg E. Hilmas;
Dept. of Materials Science and Engineering
Missouri University of Science and Technology, Rolla, MO 65401

ABSTRACT

The elevated temperature thermal properties of zirconium diboride ceramics containing boron carbide additions of up to 15 vol% were investigated using a combined experimental and modeling approach. The addition of B$_4$C led to a decrease in the ZrB$_2$ grain size from 22 μm for nominally pure ZrB$_2$ to 5.4 μm for ZrB$_2$ containing 15 vol% B$_4$C. The measured room temperature thermal conductivity decreased from 93 W/m•K for nominally pure ZrB$_2$ to 80 W/m•K for ZrB$_2$ containing 15 vol% B$_4$C. The thermal conductivity also decreased as temperature increased. For nominally pure ZrB$_2$, the thermal conductivity was 67 W/m•K at 2000°C compared to 55 W/m•K for ZrB$_2$ containing 15 vol% B$_4$C. A model was developed to describe the effects of grain size and the second phase additions on thermal conductivity from room temperature to 2000°C. Differences between model predictions and measured values were less than 2 W/m•K at 25°C for nominally pure ZrB$_2$ and less than 6 W/m•K when 15 vol% B$_4$C was added.

INTRODUCTION

Zirconium diboride (ZrB_2) is in a class of materials known as ultrahigh temperature ceramics (UHTCs). ZrB_2 is in this class because it has a high melting above 3250°C along with high thermal and electrical conductivities.[1-5] This unusual combination of properties makes ZrB_2 an excellent candidate for applications in extreme environments such as high temperature electrodes, thermal protection systems, and molten metal crucibles.[6] The hig thermal and electrical condutcivities arise from the significant electron contribution, which can be >70% at room temperature.[5] For example, the total thermal conductivity can be above 90 W/m•K with >60 W/m•K as the electron contribution.[5,7]

ZrB_2 and other transition metal borides and carbides have strong covalent bonding and low self-diffusion coefficients. As a result, a combination of temperatures of 1900°C or higher with applied external pressure is normally required to achieve full density.[8-11] Oxygen impurities in the form of ZrO_2 and B_2O_3 on particle surfaces have been shown to cause grain coarsening preferentially to densification at elevated temperatures.[12] Additives such as carbon, B_4C, and WC that react with and remove oxide impurities are used to promote densification.[12,13] Excess additives can form isolated particles, solid solutions, and/or grain boundary phases in the densified ceramics, which impact mechanical, electrical, and mechanical properties.[13,14] Specifically for thermal properties, reported room temperature thermal conductivity values for polycrystalline ZrB_2 based ceramics vary widely, from as low as 29 W/m•K to as high as 95 W/m•K.[14,15] Hence, changes to processing conditions and composition can impact thermal properties significantly. Several types of models have been used to describe the thermal conductivity of diboride based ceramics including network conductance models,[16] grain size models,[14] and effective medium theories, but these are typically limited to evaluating one specific composition[17]

The purpose of this study was to measure and model the thermal conductivity of ZrB_2 ceramics as a function of B_4C content. More generally, the study evaluated the impact of isolated, electrically insulating particles on the thermal conductivity of a conductive matrix.

PROCEDURE

Commercially available ZrB_2 (Grade B, H. C. Starck, Goslar, Germany) and B_4C (Grade HS, H. C. Starck, Goslar, Germany) powders were ball milled in hexane for one hour using ZrB_2 milling media. The resulting slurry was rotary evaporated to remove the hexane. The mass of the ZrB_2 milling media was measured before and after milling, which indicated that ~0.1 wt% additional ZrB_2 was incorporated into the resulting powders. After rotary evaporation, the powders were passed through a 50-mesh sieve.

Densification was accomplished by hot pressing using a 1-inch diameter circular graphite die in a resistively heated graphite element hot press (Thermal Technology Inc., Model HP20-3060-20, Santa Rosa, CA). The graphite die was lined with graphite paper and coated with boron nitride (Cerac, SP-108, Milwaukee, WI) to minimize reaction between the die and the powders. Specimens were heated at 40°C/min throughout the run. Below 1500°C, specimens were heated in a mild vacuum (~20 Pa). Isothermal holds of 1 hour were used at 1300°C and 1500°C during heating to allow for evaporation of B_2O_3 and/or reaction of ZrO_2 and B_2O_3 with B_4C. After the hold at 1500°C, the atmosphere was changed to flowing Ar gas at a pressure of ~10^5 Pa and a uniaxial pressure of 32 MPa was applied. The furnace was held at 2100°C until ram travel had stopped for 10 minutes. The furnace was then allowed to cool at 40°C/min. The external pressure was released below 1500°C.

Hot pressed specimens were surface ground and cut (Chevalier, FSG-3A818, Santa Fe Springs, CA) into squares approximately 12.5 mm by 12.5 mm by 3 mm thick. The outer portions of the billets were ground or cut away to remove the portion of the pellet that may have been affected by reaction with the hot press die. The bulk density of each specimen was measured by the Archimedes' technique (ASTM standard C373) using vacuum infiltration with distilled water as the immersing medium.[18] Specimens were polished using successively finer diamond abrasives with a final size of 0.25 μm. Scanning electron microscopy (SEM; Hitachi S570, Japan) was used to characterize microstructure. Grain sizes were measured from SEM micrographs using image analysis software (ImageJ, National Institutes of Health, Bethesda, MD) by analyzing ~500 grains.

Thermal diffusivity was measured by the laser flash technique (Flashline 5000, Anter Corp, Pittsburgh, PA) following the procedure defined in ASTM standard E1461.[19] Specimens were coated with graphite (Dry Graphite Lube, Diversified Brands, Cleveland, OH) and then analyzed up to 2000°C in flowing Ar that was maintained at a gauge pressure of ~41 kPa. Specimens were heated at 15°C/min. Each data point was an average of 3 tests taken at 2 minute intervals after the specimen had been held at a constant temperature for 7 minutes. Results were calculated using the Clark and Taylor method for determining thermal diffusivity (Equation 1).[20] In this calculation, thermal diffusivity (α) was dependent on specimen thickness (L) and time for the specimen to rise to a quarter, half, and three quarters of the maximum temperature ($t_{0.25}$, $t_{0.5}$, $t_{0.75}$, respectively) after the laser pulse.

$$\alpha = \frac{L^2}{t_{0.5}}[-0.346 + 0.362(t_{0.75}/t_{0.25}) - 0.065(t_{0.75}/t_{0.25})^2] \quad (1)$$

Heat capacity was calculated for each specimen based on molar ratios using data from the NIST- JANAF tables. Equations 2 and 3 were derived for ZrB_2 and B_4C, respectively, where t is the absolute temperature divided by 1000.[21] The bulk density was calculated as a function of temperature using thermal expansion data for ZrB_2 and B_4C provided by Touloukian.[22] Thermal conductivity (λ) was then calculated at each temperature from the measured thermal diffusivity (α), calculated heat capacity (C_p), and temperature-dependent bulk density (ρ), according to Equation (4).

$$C_p = 66.96 + 5.67T + 1.43t^2 - 0.15t^3 - 1.84t^{-2} \quad (2)$$

$$C_p = 96.00 + 23.17t - 0.41t^2 + 0.08t^3 - 4.40t^{-2} \quad (3)$$

$$\lambda = \alpha\rho C_p \quad (4)$$

MODEL DEVELOPMENT

A model was developed to describe the thermal conductivity behavior of the ZrB_2-B_4C ceramics as a function of B_4C addition and temperature. The approach was to calculate the electron and phonon contributions individually and then sum them to obtain the total thermal conductivity. The electron contributions were calculated using an effective medium approach assuming the electron contribution of B_4C was significantly lower than ZrB_2 (Equation 5), where $\lambda_{e,Zr}$ is the electron contribution from ZrB_2 and ν is the volume fraction of B_4C.[17,23] The phonon contribution was calculated using the Maxwell-Eucken method[24] (Equation 6) using the measured conductivity of B_4C (λ_B) and the phonon contribution data for ZrB_2 (λ_{Zr}) that was calculated in a previous study. In addition, the effect of grain size on the phonon contribution of ZrB_2 was estimated using Equation 7, where T is the absolute temperature and d is average grain size.[25]

$$\lambda_e = \lambda_{e,Zr}\frac{(2-2v)}{2+v} \tag{5}$$

$$\lambda_{ph} = \lambda_{Zr}\left(\frac{1+2v^{(1-\lambda_{Zr}/\lambda_B)}\Big/_{(2\lambda_{Zr}/\lambda_B+1)}}{1-^{v(1-\lambda_{Zr}/\lambda_B)}\Big/_{(1+\lambda_{Zr}/\lambda_B)}}\right) \tag{6}$$

$$\frac{1}{\lambda_{Zr}} = 1.7\times10^{-4}T + \frac{8.7\times10^{-8}}{d} \tag{7}$$

RESULTS AND DISCUSSION

Table I summarizes the specimen designations and bulk density information. For nominally pure ZrB_2, the bulk density was 5.93 g/cm^3, which was 97.2% of the theoretical density. Additions of as little as 1 vol% B_4C increased the relative density of the resulting ceramics. For example, the bulk density of Zr1B was 6.02 g/cm^3, which was >99% relative density. For all of the ZrB_2-B_4C specimens, relative density values were >99% of the theoretical densities based on the nominal compositions. Because of its lower theoretical density, the addition of B_4C, decreased the theortical density from 6.10 g/cm^3 for nominally pure ZrB_2 to as low as 5.62 g/cm^3 for Zr15B.

Table I: Designation, Bulk Density, and Microstructural Information

Designation	B_4C Content Vol%	Bulk Density g/cm^3	Theoretical Density g/cm^3	Relative Density %	Grain Size μm
Zr0B	0	5.93	6.10	97.2	22.4 ± 12
Zr1B	1	6.02	6.07	99.2	14.5 ± 8.8
Zr2B	2	5.98	6.03	99.2	15.9 ± 8.2
Zr5B	5	5.93	5.94	99.8	12.0 ± 7.1
Zr10B	10	5.78	5.80	99.7	9.1 ± 5.1
Zr15B	15	5.60	5.62	99.6	5.4 ± 3.1
B_4C	100	2.49	2.52	98.8	3.8 ± 1.0

Using SEM (not shown), ZrB_2 grain size, the distribution of B_4C, and the amount and location of porosity were investigated. The average grain size for nominally pure ZrB_2, Zr0B, was 22.4 μm. The addition 1 vol% of B_4C reduced the average grain size to 14.5 μm. The reduction in grain size was attributed to a combination of removing surface oxides, which would reduce grain coarsening at elevated temperatures, and the pinning effect of the B_4C particles. Larger additions of B_4C were more effective at reducing the average ZrB_2 grain size. For example, Zr5B had an average grain size of 12.0 μm. As B_4C content increased, the average grain size continued to decrease to a minimum of 5.4 μm for Zr15B. The decrease in average grain size with increasing B_4C content was attributed to the increase in pinning of ZrB_2 grain growth with the increasing volume fraction of second phase particles. Regardless of the amount of B_4C, SEM analysis revealed that the average size of B_4C inclusions in the ZrB_2 matrix was 3.8 ± 1 μm. SEM analysis also showed that B_4C was present as well dispersed, isolated particles in the ZrB_2 matrix. The addition of B_4C improved the relative density of the ZrB_2 ceramics and reduced the average grain size of the final ceramics through a combination of reaction with/removal of surface oxides and grain pinning.

Thermal conductivity was determined from the measured thermal diffusivity values, calculated heat capacity, and density information. Figure 1 shows the thermal conductivity as a function of temperature for all of the compositions. For nominally pure ZrB_2, the thermal conductivity decreased from 93 W/m•K at 25°C to 81 W/m•K at 2000°C. Above 200°C, the thermal conductivity decreased linearly from 80 W/m•K at 200°C to 67 W/m•K at 2000°C with a slope of -6.9×10^{-3} W/m•K^2. Small additions of B_4C, 1 or 2 vol%, significantly change the room temperature thermal conductivity significantly as the value was 93 W/m•K for both Zr1B and Zr2B. The thermal conductivities of these compositions, along with Zr0B, decreased to 67 W/m•K at 2000°C. Since B_4C has a lower thermal conductivity than ZrB_2, its addition should lower the thermal conductivity of the composite ceramics. The lack of change in thermal conductivity of Zr1B and Zr2B compared to Zr0B was a result of increased relative density and decreased oxide impurity contents of Zr1B and Zr2B compared to Zr0B.

The addition of more than 2 vol% B_4C decreased the thermal conductivity of the resulting ceramics. For instance, Zr5B had a thermal conductivity of 83 W/m•K at 25°C that decreased to 64 W/m•K at 2000°C. Adding more B_4C, as in the cases of Zr10B and Zr15B, further decreased the thermal conductivity at 25°C to 81 W/m•K and 79 W/m•K, respectively. The excess B_4C was present as a second phase in the ZrB_2 matrix. Because all of the B_4C-containing ceramics had relative densities >99%, the lower thermal conductivity of B_4C compared to ZrB_2 decreased the thermal conductivity of the ceramics as B_4C content increased.

Model predictions were compared to experimental thermal conductivity values using Equations 1-4. In figure 2A, the 25°C thermal conductivity values predicted by the model were compared to experimental values. For Zr0B, the model predicted a thermal conductivity of 94 W/m•K compared to the experimental value of 93 W/m•K. Likewise, the model predicted that the 25°C thermal conductivity would decreased to 77 W/m•K for Zr15B due to the presence of B_4C and the decrease in grain size, which was close to the experimental value of 80 W/m•K. The factors that impacted the room temperature conductivity the most were the B_4C addition on the electron contribution and ZrB_2 grain size on the phonon contribution.

$$\lambda = \lambda_e + \lambda_{Ph} \tag{1}$$

$$\lambda_e = \lambda_{e,Zr}\frac{(2-2v)}{(2+v)} \tag{2}$$

$$\lambda_{Ph} = \lambda_{Zr}\left(\frac{1+2v_d\left(1-{}^{\lambda_{Zr}}/_{\lambda_d}\right)/\left({}^{2\lambda_{Zr}}/_{\lambda_d}+1\right)}{1-v_d\left(1-{}^{\lambda_{Zr}}/_{\lambda_d}\right)/\left({}^{\lambda_{Zr}}/_{\lambda_d}+1\right)}\right) \tag{3}$$

$$\frac{1}{\lambda_{Zr}} = 1.7\times10^{-4}T + \frac{8.7\times10^{-8}}{d} \tag{4}$$

The thermal conductivity was predicted as a function of temperature. The model predicted that the thermal conductivity of Zr0B was 72 W/m•K at 2000°C, compared to the experimental value, 67 W/m•K (Figure 2B). The model predicted thermal conductivity values for ZrB_2-B_4C ceramics well with the exception of ZrB2 with >5 vol% B_4C. For these compositions, the model deviated from experimental values between 200°C and 800°C, with a maximum difference of 7 W/m•K. A potential reason for this discrepancy may be due more interaction of B_4C than anticipated based on the current model. This model as a whole revealed that while the electron contribution to thermal conductivity was solely due to ZrB_2, the phonon contribution was higher than expected based solely on the volume fraction of B_4C in the composite.

CONCLUSION

The thermal conductivity values of ZrB_2-B_4C ceramics were modeled and compared to experimental data to determine how isolated second phases affected high temperature behavior. The addition of B_4C to ZrB_2 decreased the grain size from 22 μm for pure ZrB_2 to 5.4 μm for Zr15B. The addition of B_4C also decreased the thermal conductivity of the ZrB_2 ceramics to 79.6 W/m•K for Zr15B at 25°C compared to 93.0 W/m•K for Zr0B. In each case, the thermal conductivity decreased quickly from 25°C to 200°C. Above 200°C, the thermal conductivity decreased linearly to 2000°C. At 2000°C, the thermal conductivity of Zr0B was 67.3 W/m•K and decreased to 60.5 W/m•K for Zr15B. A model for the thermal conductivity was developed using B_4C content, ZrB_2 grain size, and temperature and was in agreement with measured values. The developed model revealed that B_4C improved the phonon contribution to thermal conductivity and decreased the electron contribution, which decreased the total thermal conductivity compared to pure ZrB_2. The model can calculate the expected thermal conductivity for ZrB_2 with a non-electrically conducting second phase with volume percent of second phase and conductivity of ZrB_2 and second phase as a function of temperature.

ACKNOWLEDGEMENTS

The Authors would like to acknowledge the AMCL at Missouri S&T for the use of the SEM.

REFERENCES:

1. R.A. Cutler, "Engineering Properties of Borides," pp. 787-803 in Vol. 4, *Ceramics and Glasses: Engineered Materials Handbook.* Edited by S. J. S. Jr. ASM International, Materials Park, OH, 1991.

2. L.S.S. R. Telle, and K. Takagi, "Boride-Based Hard Materials," pp. 802-945 in *Handbook of Ceramic Hard Materials.* Edited by R. Riedel. Wiley-VCH, Weinheim, Germany, 2000.

3. X. Zhang, X. Luo, J. Han, J. Li, and W. Han, "Electronic structure, elasticity and hardness of diborides of zirconium and hafnium: First principles calculations," *Computational Materials Science,* **44** [2] 411-21 (2008).

4. S. Guo, Y. Kagawa, T. Nishimura, and H. Tanaka, "Thermal and Electric Properties in Hot-Pressed ZrB_2-$MoSi_2$-SiC Composites," *Journal of the American Ceramic Society,* **90** [7] 2255-8 (2007).

5. L. Zhang, D.A. Pejaković, J. Marschall, and M. Gasch, "Thermal and Electrical Transport Properties of Spark Plasma-Sintered HfB_2 and ZrB_2 Ceramics," *Journal of the American Ceramic Society,* **94** [8] 2562-70 (2011).

6. M.M. Opeka, I.G. Talmy, and J.A. Zaykoski, "Oxidation-based materials selection for 2000C + hypersonic aerosurfaces: Theoretical considerations and historical experience: Special Section: Ultra-High Temperature Ceramics (Guest Editors: Joan Fuller and Michael D. Sacks)," *Journal of Materials Science,* **39** 5887-904 (2004).

7. R.P. Tye and E.V. Clougherty, "The Thermal and Electrical Conductivities of some Electrically Conducting Compounds," *Proceedings of the Fifth Symposium on Thermophysical Properties,* 396-401 (1970).

8. William G. Fahrenholtz, Gregory E. Hilmas, Inna G. Talmy, and James A. Zaykoski, "Refractory Diborides of Zirconium and Hafnium," *Journal of the American Ceramic Society,* **90** [5] 1347-64 (2007).

9. A. Rezaie, W.G. Fahrenholtz, and G.E. Hilmas, "Effect of hot pressing time and temperature on the microstructure and mechanical properties of ZrB_2-SiC," *Journal of Materials Science,* **42** [8] 2735-44 (2007).

10. A.L. Chamberlain, W.G. Fahrenholtz, G.E. Hilmas, and D.T. Ellerby, "High-Strength Zirconium Diboride-Based Ceramics," *Journal of the American Ceramic Society,* **87** [6] 1170-2 (2004).

11. D. Kalish and E. Clougherty, "Densification Mechanisms in High-pressure Hot-Pressing of HfB_2," *Journal of the American Ceramic Society,* **52** [1] 26-30 (1969).

12. S. Zhu, W.G. Fahrenholtz, G.E. Hilmas, and S.C. Zhang, "Pressureless sintering of carbon-coated zirconium diboride powders," *Materials Science and Engineering: A,* **459** [1-2] 167-71 (2007).

13. William G. Fahrenholtz, Gregory E. Hilmas, Shi C. Zhang, and Sumin Zhu, "Pressureless Sintering of Zirconium Diboride: Particle Size and Additive Effects," *Journal of the American Ceramic Society,* **91** [5] 1398-404 (2008).

14. J.W. Zimmermann, G.E. Hilmas, W.G. Fahrenholtz, R.B. Dinwiddie, W.D. Porter, and H. Wang, "Thermophysical Properties of ZrB_2 and ZrB_2-30SiC Ceramics," *Journal of the American Ceramic Society,* **91** [5] 1405-11 (2008).

15. W.-B. Tian, Y.-M. Kan, G.-J. Zhang, and P.-L. Wang, "Effect of carbon nanotubes on the properties of ZrB_2-SiC ceramics," *Materials Science and Engineering: A,* **487** [1-2] 568-73 (2008).

16. M. Gasch, S. Johnson, and J. Marschall, "Thermal Conductivity Characterization of Hafnium Diboride-Based Ultra-High-Temperature Ceramics," *Journal of the American Ceramic Society,* **91** [5] 1423-32 (2008).

17. A. Eucken, *Thermal conductivity of refractory ceramic materials: its calculation from the thermal conductivity of the components*. 1932.

18. ASTM C373, "Standard Test Method for Water Absorption, Bulk Density, Apparent Porosity, and Apparent Specific Gravity of Fired Whiteware Products," *ASTM International,* (2006).

19. ASTM E1461, "Standard Test Method for Thermal Diffusivity of Solids by the Flash Method," *ASTM International,* (2001).

20. L.M. Clark and R.E. Taylor, "Radiation loss in the flash method for thermal diffusivity," *Journal of Applied Physics,* **46** [2] 714-9 (1975).

21. M.W. Chase, *NIST-JANAF Thermochemical Tables*. American Chemical Society and the American Institute of Physics, Woodbury, NY, 2000.

22. Y. Touloukian, C. Ho, and D. Dewitt, *Thermal Expansion: Nonmetallic Solids,* Vol. 13. Edited by Touloukian. IFI/Plenum, New York, 1970.

23. C.-N. Sun, M.C. Gupta, and W.D. Porter, "Thermophysical Properties of Laser-Sintered Zr–ZrB_2 Cermets," *Journal of the American Ceramic Society,* **94** [8] 2592-9 (2011).

24. F.L. Levy, "A modified Maxwell-Eucken equation for calculating the thermal conductivity of two-component solutions or mixtures," *International Journal of Refrigeration,* **4** [4] 223-5 (1981).

25. D.S. Smith, S. Fayette, S. Grandjean, C. Martin, R. Telle, and T. Tonnessen, "Thermal Resistance of Grain Boundaries in Alumina Ceramics and Refractories," *Journal of the American Ceramic Society,* **86** [1] 105-11 (2003).

FIGURES:

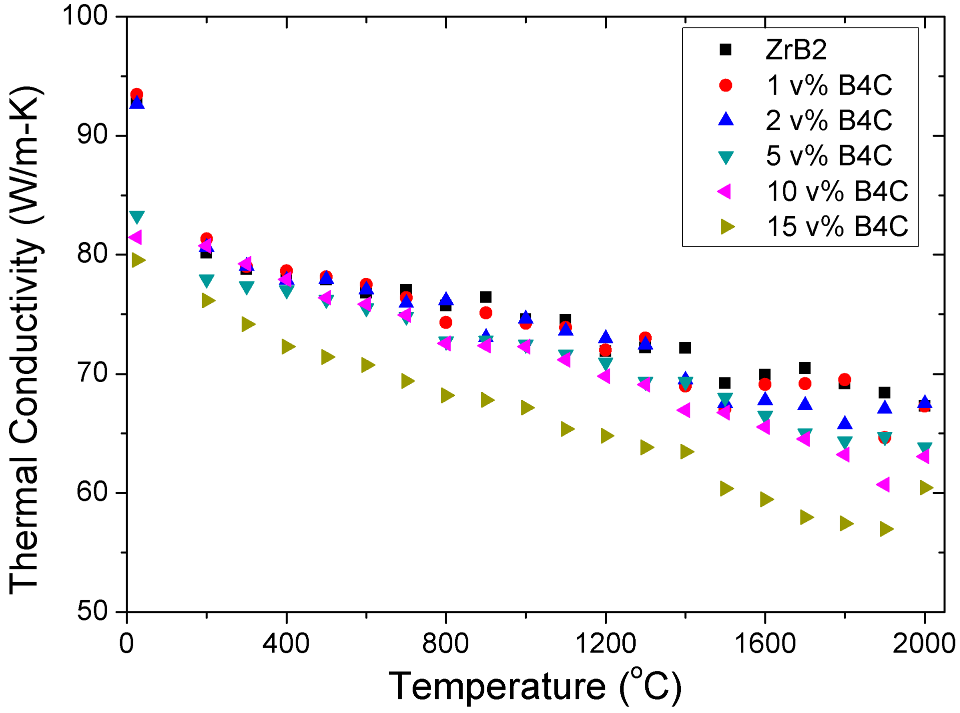

Figure 1: Thermal conductivity of ZrB_2-B_4C ceramics as a function of temperature calculated from the measured thermal diffusivity and calculated heat capacity and bulk density.

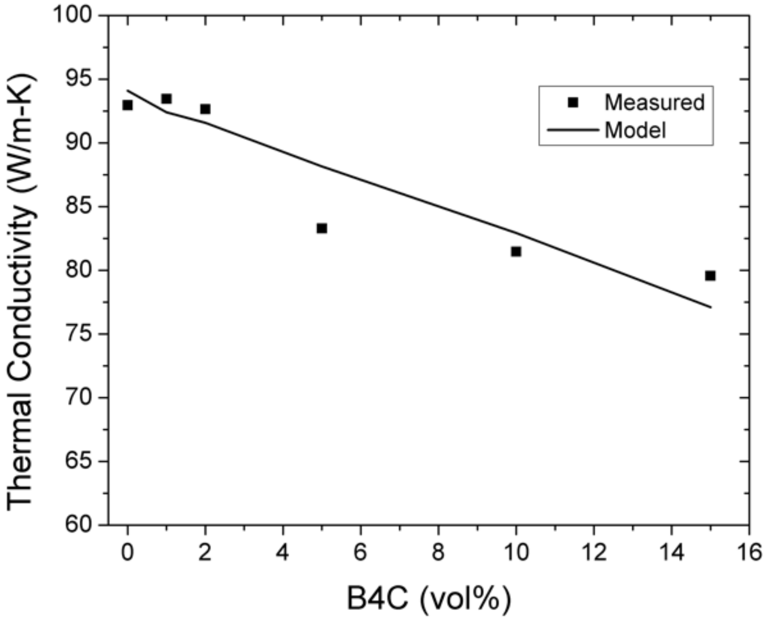

A

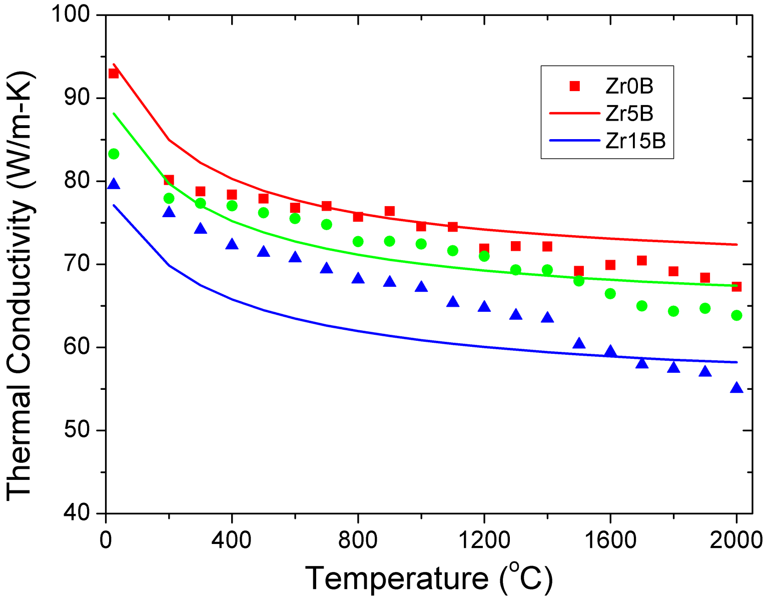

B

Figure 2: Comparison of model predictions (lines) to measured values (points) of thermal conductivity at (A) room temperature and (B) as a function of temperature for ZrB_2-B_4C ceramics.

VITA

Matthew Joseph Thompson was born on in Rochester, NY. Until 2003, he resided in the town of Greece, NY near the shores Lake Ontario. After attending St. Lawrence elementary school and Odyssey Academy he graduated from Aquinas Institute. In the fall of 2003, Matthew began his undergraduate career at Alfred University. During that time, he worked in a number of areas including being a teaching assistant, computer lab assistant, and undergraduate researcher. Nearing graduation, he earned the material science and engineering Outstanding senior award. While in his undergraduate career, he held several leadership positions including Treasurer for Tau Beta Pi, as well as the Vice President and President of Keramos. He graduated Cum Laude in 2007 and started his PhD in August of the same year.

Upon entering graduate school at the University of Missouri Rolla, later renamed Missouri University of Science and Technology, he received the Chancellors Fellowship that provided financial support for tuition and fees. His PhD research focused on the processing, characterization, and thermal properties of materials for hypersonic thermal protection systems. He had nine presentations at seven conferences nationally and published two manuscripts with three more pending. After the completion of his PhD requirements, Matthew will continue working as a ceramic engineer for NorPro, a division of Saint Gobain in Akron, OH.